Max-Planck-Institut
für Meteorologie

MAX-PLANCK-GESELLSCHAFT

International Max Planck Research School
on Earth System Modelling

Linking marine dust records to Saharan landscape evolution during the Holocene

- a theoretical study -

Sabine Egerer

Hamburg 2018

Berichte zur Erdsystemforschung
Reports on Earth System Science

203
2018

Hinweis

Die Berichte zur Erdsystemforschung werden vom Max-Planck-Institut für Meteorologie in Hamburg in unregelmäßiger Abfolge herausgegeben.

Sie enthalten wissenschaftliche und technische Beiträge, inklusive Dissertationen.

Die Beiträge geben nicht notwendigerweise die Auffassung des Instituts wieder.

Die "Berichte zur Erdsystemforschung" führen die vorherigen Reihen "Reports" und "Examensarbeiten" weiter.

Notice

The Reports on Earth System Science are published by the Max Planck Institute for Meteorology in Hamburg. They appear in irregular intervals.

They contain scientific and technical contributions, including Ph. D. theses.

The Reports do not necessarily reflect the opinion of the Institute.

The "Reports on Earth System Science" continue the former "Reports" and "Examensarbeiten" of the Max Planck Institute.

Anschrift / Address

Max-Planck-Institut für Meteorologie
Bundesstrasse 53
20146 Hamburg
Deutschland

Tel./Phone: +49 (0)40 4 11 73 - 0
Fax: +49 (0)40 4 11 73 - 298

name.surname@mpimet.mpg.de
www.mpimet.mpg.de

Layout

Bettina Diallo and Norbert P. Noreiks
Communication

Copyright

Linking marine dust records to Saharan landscape evolution during the Holocene

- a theoretical study -

Dissertation with the aim of achieving a doctoral degree
at the Faculty of Mathematics, Informatics and Natural Sciences
Department of Earth Sciences of Universität Hamburg
submitted by

Sabine Egerer

Hamburg 2018

Sabine Egerer

Max-Planck-Institut für Meteorologie
Bundesstrasse 53
20146 Hamburg

Tag der Disputation: 04.12.2017

Folgende Gutachter empfehlen die Annahme der Dissertation:

Prof. Dr. Martin Claussen
Dr. Christian Reick

Berichte zur Erdsystemforschung / Max-Planck-Institut für Meteorologie 203
Reports on Earth System Science / Max Planck Institute for Meteorology 2018

ISSN 1614-1199

Abstract

Marine sediment records show an abrupt and large increase in North Atlantic dust deposition towards the end of the African Humid Period (AHP) about 5 ka BP. How this abrupt shift in dust deposition is linked to Holocene North African landscape and climate change is still under debate. Within the scope of this thesis, we simulate the North African dust cycle from the mid-Holocene until present-day using the coupled aerosol-climate model ECHAM6-HAM2. We thereby identify drivers of the change in dust deposition and set the dynamics of dust deposition in context to North African landscape evolution.

In a first step, we simulate the pre-industrial and mid-Holocene dust cycle, where vegetation and lake cover as well as orbit and ocean conditions are prescribed. Consistent with marine sediment records, our simulations show that North Atlantic dust deposition fluxes were two to three times lower during the mid-Holocene compared with pre-industrial fluxes. In a sensitivity study, we identify enhanced vegetation cover and extended lake surface area to be the main cause of the reduced dust cycle during the AHP as they cover dust source areas and alter the atmospheric circulation.

In a second step, we aim to understand the dynamics of the dust cycle. Therefore, we test the hypothesis that gradual changes in North African landscape result in an abrupt shift in North Atlantic dust deposition. This could have been caused either due to the nonlinearity in dust activation or due to a heterogeneous distribution of major dust sources. To explore these two arguments, we prescribe a gradual decline of North African vegetation and lake cover in two series of simulations. In contrast to our hypothesis, we do not find evidence for an abrupt increase in simulated dust deposition as seen in the marine records. Our results rather point to a rapid large-scale retreat of vegetation and lakes in the area of significant dust sources in the northwest Sahara.

Finally, we perform time slice simulations including dynamic vegetation. We find a rapid increase in North Atlantic dust deposition in our simulations as indicated by the marine records. The sudden increase in simulated dust deposition is linked to a rapid decline of vegetation and precipitation from 22°N to 18°N in the western Sahara pointing to strong local vegetation-precipitation feedbacks. Changes in dust source areas and vegetation in the eastern Sahara and south of 18°N as well as changes in atmospheric circulation contribute only minor to the abrupt change in dust deposition. Our study emphasizes spatial and temporal differences in the transition of North African landscape. Conclusions from local records to large scales have thus to be treated with caution.

Zusammenfassung

Marine Sedimentaufzeichnungen zeigen einen abrupten und starken Anstieg der marinen Staubablagerung im Nordatlantik gegen Ende der Afrikanischen Feuchtperiode vor etwa 5000 Jahren. Wie dieser plötzliche Anstieg der Staubablagerung mit der Veränderung der Nordafrikanischen Landschaft und des Klimas während des Holozäns zusammenhängt, wird nach wie vor diskutiert. Im Rahmen dieser Arbeit simulieren wir den Nordafrikanischen Staubkreislauf vom mittleren Holozän bis heute mit Hilfe des gekoppelten Aerosol-Klimamodelles ECHAM6-HAM2. Dabei differenzieren wir die unterschiedlichen Antriebe einer Veränderung des Staubflusses und stellen die Dynamik der Staubablagerung in Zusammenhang mit der Nordafrikanischen Landschaftsentwicklung.

In einem ersten Schritt simulieren wir den vorindustriellen Staubkreislauf sowie den des mittleren Holozäns. Vegetations- und Seenbedeckung sowie der orbitale Antrieb und Meeresoberflächentemperaturen sind dabei vorgeschrieben. In Übereinstimmung mit Beobachtungen aus den Sedimentbohrkernen zeigen unsere Simulationen, dass die Staubablagerungsflüsse während des mittleren Holozäns zwei bis drei Mal geringer waren als während der vorindustriellen Zeit. Mit Hilfe einer Sensitivitätsstudie ermitteln wir, dass ausgeweitete Vegetations- und Seenbedeckung die Hauptursachen des verminderten Staubflusses während der Afrikanischen Feuchtperiode waren indem sie Staubquellgebiete bedeckten und die atmosphärische Zirkulation beeinflussten.

Im nächsten Schritt wollen wir die Dynamik des Staubkreislaufes verstehen. Dafür testen wir die Hypothese, dass eine graduelle Veränderung der Nordafrikanischen Landschaft zu einem abrupten Wechsel der Nordafrikanischen Staubablagerung führte. Dies könnte entweder durch den nichtlinearen Zusammenhang zwischen Bodenwinden und Staubaktivierung oder durch eine heterogene Verteilung der Hauptstaubquellen verursacht worden sein. Um diese beiden Argumente näher zu beleuchten, schreiben wir eine graduelle Abnahme der Nordafrikanischen Vegetations- und Seenbedeckung in zwei unterschiedlichen Simulationsreihen vor. Im Gegensatz zu unserer Hypothese finden wir keine Anzeichen für einen abrupten Anstieg der Staubdeposition in unseren Simulationen. Unsere Ergebnisse deuten eher auf einen rapiden und großräumigen Rückzug der Vegetation und der Seen im Gebiet signifikanter Staubquellen in der nordwestlichen Sahara hin.

Schließlich simulieren wir Zeitscheiben unter der Berücksichtigung dynamischer Vegetation. In diesen Simulationen finden wir einen rapiden Anstieg der Staubablagerung im Nordatlantik genau wie in den marinen Sedimentaufzeichnungen. Der plötzliche Anstieg der simulierten Staubablagerungen ist mit einem rapiden Rückzug der Vegetation und des Niederschlags von 22°N auf 18°N in der westlichen Sahara verknüpft,

was auf starke lokale Vegetations-Niederschlagsrückkopplungen hindeutet. Veränderungen der Staubquellen und der Vegetation in der östlichen Sahara und südlich von 18°N sowie Veränderungen der atmosphärischen Zirkulation tragen nur wenig zu der abrupten Veränderung der Staubablagerung bei. Unsere Studie zeigt räumliche und zeitliche Unterschiede im Übergang der Nordafrikanischen Landschaft auf. Rückschlüsse von lokalen Aufzeichnungen auf ein großräumiges Gebiet müssen demzufolge mit Vorsicht betrachtet werden.

Contents

List of Figures

List of Tables

Abbreviations

0k	Pre-industrial
6k	Mid-Holocene
AEJ	African Easterly Jet
AeroCom	Aerosol Model Intercomparison Project
AEW	African Easterly Waves
AHP	African Humid Period
AO	Atmosphere and ocean conditions
BP	Before present
DJF	Winter months: december, january, february
ECHAM	Atmospheric component of MPI-ESM1
FPAR	Fraction of absorbed photosynthetically active radiation
GCM	General Circulation Model
ICON	ICOsahedral Non-hydrostatic General Circulation Model
IPCC	Intergovernmental Panel on Climate Change
ITCZ	Intertropical Convergence Zone
ITF	Intertropical Front
JJA	Summer months: june, july, august
JSBACH	Jena Scheme for Biosphere-Atmosphere Interaction in Hamburg, land component of MPI-ESM1
LAI	Leaf area index
LV	Land surface conditions including lakes and vegetation
mh	mid-Holocene
MPI-ESM1	Max Planck Insitute Earth System Model
NE	Northeast Sahara (10°E–35°E; 18°N–30°N)
NLLJ	Nocturnal low level jet

NPP	Net primary productivity
NW	Northwest Sahara (15°W–10°E; 18°N–30°N)
PFT	Plant functional types
pi	pre-industrial
PMIP	Paleo Model Intercomparison Project
SAL	Saharan Air Layer
SHL	Saharan Heat Low
SIC	Sea ice concentration
SST	Sea surface temperature
TEJ	Tropical Easterly Jet
TNA	Tropical North Atlantic
WAM	West African monsoon

Physical Constants and Variables

α	Ratio of vertical to horizontal dust flux
α_{dark}	Albedo of darkened soil
α_{obs}	Standard soil albedo in JSBACH based on present-day observations
α_{soil}	Soil albedo
A_{eff}	Effective surface ratio available for dust emission
$C = 2.61$	Constant determined from wind tunnel experiments (White, 1979)
D	Vertical dust flux
D_p	Particle diameter
f_{bare}	Bare soil fraction of a grid cell
f_{gap}	Gaps within the vegetated fraction of a grid cell
f_{lake}	Fraction of a grid cell covered with lakes
f_{pot}	Fraction of a grid cell acting as a potential dust source area
f_{snow}	Fraction of a grid cell covered with snow
f_{veg}	Vegetated fraction of a grid cell
$g = 9.81\text{m/s}$	Gravitational acceleration
G	Horizontal dust flux
i	Particle size fraction
I_θ	Indicator for soil wetness; $I_\theta = 0$ if the uppermost soil layer is wet, $I_\theta = 1$ otherwise
$\overline{NPP}$	5-years average NPP
NPP_{dark}	Threshold NPP to keep the soil dark
ρ_a	Air density
u^*	Wind velocity
u_t^*	Threshold friction wind velocity

Chapter 1

General Introduction

The study of paleoclimates and past climate changes sheds light on ancient environmental conditions, human cultures and civilizations, helps to estimate the sensitivity of Earth system components to internal and external forcing, and supports predicting the magnitude and speed of future climate change. An era of particular interest is the mid-Holocene, roughly between 9 and 6 ka BP, as stable climate conditions and a large archive of records provide an optimal playground for climate scientists.

During this time period, the so called 'African Humid Period' (AHP) peaked across North Africa, which was triggered by a steady shift in the Earth's orbit (Berger, 1978). The Northern hemisphere received on average about 4.5% more summer insolation compared to present-day which caused a higher temperature and pressure gradient between the North African subcontinent and the Eastern Atlantic Ocean. This led to a strengthening of the West African summer monsoon and a consequent northward shift of the tropical rain belt by about 4° to 6° (Kutzbach, 1981). The wet climate supported the establishment of permanent vegetation cover (Kutzbach and Street-Perrott, 1985; Hoelzmann et al., 1998; Jolly et al., 1998b; Joussaume et al., 1999; Hély et al., 2014), widespread lakes and wetlands (Hoelzmann et al., 1998; Gasse, 2000; Lézine et al., 2011), a dense fluvial river network (Drake et al., 2011), and there is evidence for the presence of humans (Kuper and Kröpelin, 2006). Pollen records indicate a considerable expansion of vegetation in North Africa at that time (Prentice et al., 2000) with steppe, savanna and temperate xerophytic woods and shrubs extending up to 23°N (Jolly et al., 1998a). Lakes and wetlands were sustained up to 30°N and covered about 7.6% of North Africa (Street-Perrott et al., 1989; Hoelzmann et al., 1998; Jolly et al., 1998a; Kröpelin et al., 2008). The largest water body was lake Megachad with an area of 350 000 km^2 presumably (Schuster et al., 2005).

Marine sediment records along the northwest African margin reveal that during the AHP, North Atlantic dust deposition was reduced by a factor of 2 (deMenocal et al., 2000) to 5 (McGee et al., 2013a). As the main sources providing dust to the North Atlantic have been ever located upwind in the Sahara during the Holocene (Carlson and Prospero, 1972), the reduced dust deposition has been attributed to enhanced Saharan vegetation cover (deMenocal et al., 2000) or to extended lake surface area (Cockerton et al., 2014), that inhibited dust emission. Alternatively, the decreased dust deposition during the mid-Holocene has been linked to weaker surface winds and a consequent reduction of coastal upwelling (Adkins et al., 2006; Bradtmiller et al., 2016). However, the relative importance of these drivers of changes in North Atlantic dust deposition has not yet been assessed.

So far, two modeling studies have simulated the mid-Holocene dust cycle using a general circulation model (GCM) (Albani et al., 2015; Sudarchikova et al., 2015). Both of them determined dust emission fluxes as a function of simulated vegetation cover. However, as most climate models, they failed to reproduce the northward extent of the West African monsoon during the mid-Holocene (Perez-Sanz et al., 2014) as indicated by precipitation reconstructions (Bartlein, 2011). As a consequence, the northern Sahara was too dry in the models to support the vegetation extent that was predicted by pollen records (Hoelzmann et al., 1998; Jolly et al., 1998b) and too much dust was emitted from the uncovered soil. Also, the presence of paleolakes was not taken into account in either study, despite the fact that areas covered by lakes lose their potential as a dust source. Consequently, the modeling studies overestimated mid-Holocene dust emission in North Africa and simulated higher dust deposition rates in the North Atlantic than indicated by marine sediment records along the northwest African margin (deMenocal et al., 2000; Adkins et al., 2006; McGee et al., 2013a; Albani et al., 2015).

The assessment of realistic atmospheric circulation and land surface is a necessary condition to simulate the mid-Holocene dust cycle accurately and to determine the relevance of Saharan landscape changes on the reduced dust cycle during the mid-Holocene. In turn, the inclusion of accurate dust load was emphasized as key to reasonably simulate mid-Holocene climate (Pausata et al., 2016) because mineral dust has the potential to change the radiation budget (Yoshioka et al., 2007; Spyrou et al., 2013), to impact precipitation patterns (Rosenfeld et al., 2001; Hui et al., 2008; Lau et al., 2009), and to alter the cloud structure (Lohmann, 2002). Prescribing enhanced vegetation cover (Irizarry-Ortiz et al., 2003; Kutzbach et al., 1996) or using an interactive vegetation model (Claussen and Gayler, 1997) was suggested to increase consistency with paleo evidence. For example, Irizarry-Ortiz et al. (2003) were able to simulate a northward shift of the monsoon rain belt of 5° and maintain vegetation cover by prescribing vegetation

initially based on pollen data (Hoelzmann et al., 1998) and allowing for dynamical vegetation. Krinner et al. (2012) found that the inclusion of lakes contributes significantly to the strengthening of the summer monsoon.

Further, the North Atlantic sediment records show that the transition to higher dust deposition fluxes occurred abruptly within centuries, much faster than the gradual change in orbital forcing, some 5.5 ka ago (Adkins et al., 2006) or about 4.9 ka BP (McGee et al., 2013a). The abrupt increase in North Atlantic dust deposition was attributed to a sudden decline of Saharan vegetation. This decline can be explained either with a nonlinear response of vegetation to water availability (Liu et al., 2006; Liu et al., 2007) or with strong vegetation-climate feedbacks (Brovkin et al., 1998; Claussen et al., 1999). Other positive feedbacks that were emphasized to amplify the gradual insolation forcing during the mid-Holocene include those between vegetation and soil (Kutzbach et al., 1996; Liu et al., 2010), surface water and climate (Coe and Bonan, 1997; Krinner et al., 2012), SST and climate (Kutzbach and Liu, 1997; Zhao et al., 2005), SST and dust (Williams et al., 2016), and feedbacks between dust and climate (Pausata et al., 2016). These positive feedbacks could have favored multiple stable states enabling the rapid transition from a highly vegetated humid state to a hyperarid desert state under a gradually changing orbital forcing (Brovkin et al., 1998; Claussen, 1998). The rapidly diminishing vegetation and lakes may have resulted in sudden dust emission from the uncovered soil and an associated abrupt increase in North Atlantic dust deposition (deMenocal et al., 2000). Also, paleohydrological reconstructions show a fast drying out of all water bodies around 4.5 ka BP (Lézine et al., 2011).

In contrast, other modeling studies (Renssen et al., 2003) and paleo climate and ecosystem data derived from a Lake Yoa sediment record (Kröpelin et al., 2008) indicate a more gradual change in vegetation cover and precipitation. Grain size analysis from a core off the northwest African margin reveals a quite steady change in continental humidity (Tjallingii et al., 2008). Two arguments support that even a gradual change in North African landscape could have led to a sudden increase in North Atlantic dust deposition. Firstly, the smaller surface roughness length of reduced vegetation causes a strengthening of surface winds. Due to the highly nonlinear dependence of dust activation on the surface wind speed (Bagnold, 1941; White, 1979), dust deflation and associated North Atlantic dust deposition may have risen rapidly as speculated by Cockerton et al. (2014). Secondly, paleohydrologic reconstructions show a time-transgressive southward retreat of the tropical rain belt (Shanahan et al., 2015). Consistently, vegetation and lakes shifted southward as a consequence of the West African monsoon retreat (Lézine et al., 2011; Shanahan et al., 2015). Especially highly productive northwest African dust sources (Engelstaedter et al., 2006) could have been activated rapidly when the land cover retreated

to lower latitudes causing an abrupt increase in dust deposition in the North Atlantic. Up to now, these speculations are not further evaluated by modeling studies.

Previous studies have simulated the dust cycle for specific time slices including present-day (Tegen et al., 2002; Werner et al., 2002; Stanelle et al., 2014), pre-industrial (Albani et al., 2015; Sudarchikova et al., 2015), mid-Holocene (Albani et al., 2015; Sudarchikova et al., 2015) and the last glacial maximum (Mahowald et al., 1999; Werner et al., 2002). These studies provide only information at a certain point in time and do not capture the entire Holocene era. Solely Albani et al. (2015) predicted the dust cycle from 8 ka BP until present in 2 ka intervals applying a scaling mechanism on dust emission to constrain dust depositions to observations. This modeled reconstruction can only serve as a first guess as it operates on coarse macro-areas and the model lacks of a dynamic coupling between vegetation and dust.

1.1 Thesis outline

In the scope of the thesis, our main objective is to link North Atlantic dust deposition to Saharan land surface conditions during the Holocene to help interpreting the North Atlantic sediment records. To do so, we perform time slice simulations from the mid-Holocene (6k) to pre-industrial (0k) using the coupled climate-aerosol model ECHAM6-HAM2. We thereby address the following questions:

- What is the cause of the large difference between mid-Holocene and pre-industrial dust deposition in the North Atlantic? (Chapter 2)
- Could gradual changes in Holocene Saharan landscape have caused the observed abrupt shift in North Atlantic dust deposition? (Chapter 3)
- How is the abrupt change in North Atlantic dust deposition spatially and temporally linked to Holocene Saharan landscape evolution? (Chapter 4)

Firstly, we give a short summary of the present knowledge about dust sources and transport in North Africa, introduce the aerosol-climate model ECHAM6-HAM2 and provide some information on the characterization and location of the marine sediment records that motivated our study.

Thereafter, we perform stationary state simulations for the mid-Holocene (6k) time slice and a pre-industrial control (0k) in Chapter 2. Because climate models fail to reproduce the extent and strength of the West African monsoon during the mid-Holocene (Perez-Sanz et al., 2014) and thus lack the abundance of vegetation as reconstructed by proxy

data (Jolly et al., 1998a; Hoelzmann et al., 1998; Larrasoaña et al., 2013), we prescribe vegetation conditions in North Africa based on pollen data of Hoelzmann et al. (1998) and specify the distribution of paleolakes from simulations (Tegen et al., 2002). Via a sensitivity study, we determine the relative importance of the drivers of the large changes in North Atlantic dust deposition.

In Chapter 3, we focus on the link between the dynamics of North Atlantic dust deposition and Saharan landscape evolution. In two scenarios, we explore whether gradually declining vegetation and lakes have the potential to cause an abrupt shift in dust deposition as indicated by marine sediment records. Therefore, we conduct two series of equilibrium simulations. In the first scenario, vegetation and lakes are prescribed to decline homogeneously in the North African domain. In the second scenario, the northern limit of vegetation and lake extent is shifted stepwise southward.

We perform time slice simulations in Chapter 4 to investigate the transition from the highly vegetated humid mid-Holocene Sahara to today's hyperarid desert. These simulations include dynamic vegetation and interactive dust to account for the role of feedbacks between vegetation, climate and dust. In this chapter, we analyze how North Atlantic dust deposition change is spatially and temporally linked to changes in Holocene Saharan landscape and climate.

Finally, we give a summary of our results, discuss the shortcomings of our study, point to possible solutions of these limitations and draw implications from our study for future research.

1.2 Dust sources and transport in North Africa

The purpose of this section is to review the common knowledge about dust sources and transport in North Africa and to gain a deeper understanding of the relevant processes and the annual cycle of dust emission at present-day. The studies that explore mid-Holocene dust emission and transport are restricted to the analysis of dust records (Sarnthein, 1978; Sarnthein et al., 1981). Knowledge of dust sources and meteorological processes for dust emission is important to understand the drivers of dust emission and the dust dynamics on various time scales. Further, it is crucial to identify limitations in the implementation of these processes in dust models.

The world's most active dust sources today are located in the Sahara (Goudie and Middleton, 2001; Middleton and Goudie, 2001; Prospero et al., 2002) providing about 40-70% of the global dust budget (Engelstaedter et al., 2006). The most active dust sources are the Bodélé Depression in Northern Chad and several dust source areas that are spread across Mali, Mauritania and southwestern Algeria (Fig. 1.1) (Middleton and Goudie, 2001; Prospero et al., 2002; Engelstaedter et al., 2006). Beyond these well-defined areas, recent studies have suggested that dust regions are much more widespread across the Sahara (Crouvi et al., 2012). Especially topographic depressions, which contain dry lake deposits, and playas are identified by satellite data as hot spots of dust emission (Prospero et al., 2002; Tegen et al., 2002). Additionally, satellite data of higher resolution indicate that sand dunes are important dust sources (Crouvi et al., 2012).

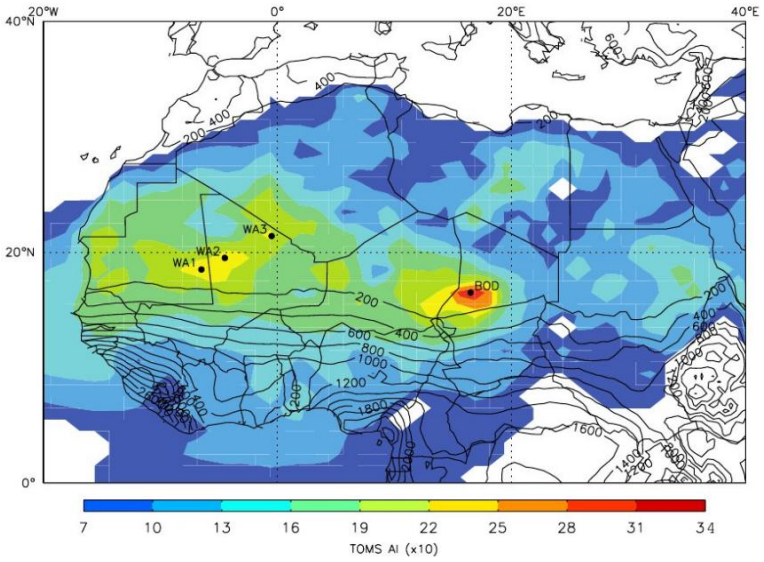

FIGURE 1.1: Long-term mean TOMS AI (x10) over Africa (filled contours) and long-term mean precipitation. West African major dust hot spots are indicated as WA1, WA2, WA3 and the Bodélé Depression in Chad as BOD. Reprint of Fig. 1 from Engelstaedter and Washington (2007).

The major summer dust plume extends thereby from 17°N to 20°N, whereas during boreal winter it is located further south (Cockerton et al., 2014). Aeolian sediments indicate that the position of the dust plume and wind systems probably remained stable throughout the Holocene but the strength of the dust belt was strongly reduced during the mid-Holocene (Sarnthein et al., 1981). However, more recent studies (Irizarry-Ortiz et al., 2003; Patricola and Cook, 2007) found a northward shift of the wind systems, that are relevant for dust transport, by several degrees during mid-Holocene summer.

Dust emission, transport and deposition in North Africa is controlled by atmospheric processes that range from micro-scale to continental scale. Processes that act on small and mesoscales involve:

1. Nocturnal low level jets (NLLJ): downward mixing of momentum during the morning hours after breakdown of the NLLJ (Fiedler et al., 2013)
2. Cyclones (Fiedler et al., 2014) and Harmattan surges (Fiedler et al., 2015)
3. Haboobs: cold pool formation due to deep convection (Sutton, 1925; Lawson, 1971), associated with around 40% of North African dust emission (Heinold et al., 2013)
4. Dust devils: Dry boundary layer convection, contribute from 3.4% (Jemmett-Smith et al., 2015) up to 35% (Koch and Renno, 2005) to the global dust budget

The synoptic weather system is determined by the West African monsoon (WAM) during Northern hemisphere summer between 9°N and 20°N at present-day. The monsoon circulation results from the differing heat capacities of the southwest Equatorial Ocean and North African land masses. Water can absorb much more radiation energy due to its higher heat capacity. Additionally, absorbed heat is transported to deeper layers due to turbulent mixing. On the continent, heat is transported through molecular diffusion. In the summer, when the net radiation is higher in the Northern hemisphere, the continent warms much more than the adjoining southwest Equatorial Ocean resulting in a temperature and pressure gradient. Close to the surface, humid air masses are dragged in direction of lower pressure and stronger warming at the continent. In the region of maximal temperature in the northwest Sahara (roughly between 21°N and 26°N), warm air rises forming the thermal induced Saharan Heat Low (SHL) at the surface. The air masses that are dragged by the continental low pressure zone originate from the Southern Hemisphere. On the Northern hemisphere, they are distracted by the Coriolis force which generates the characteristic southwest monsoon circulation. These moist air masses converge between 15°N and 20°N with the hot dry northeasterly trade winds (Harmattan) that represent the surface flow of the Hadley circulation north of the thermal low. A line of confluence with a prominent shift in temperature and dew point emerges, the Intertropical Front (ITF), which marks the seasonal intrusion or retreat of the monsoon on the subcontinent (Fink, 2006). In the Northern summer, the ITF reaches its most

northern position at about 20°N and retreats during winter to about 7°N. Additionally, the transition of the convergence belt across major dust sources in the west-central Sahara induces the maximal dust emission during summer due to dry, deep convection by enhancing near surface turbulence (Engelstaedter et al., 2006).

Due to the positive temperature gradient and negative soil moisture gradient between the Saharan desert and the southwesterly air masses, the strong vertical shear in the zonal wind induces the formation of the African Easterly Jet (AEJ) (Cook, 1999) with its core located at around 600 hPa, at approximately 4km height, during summer (Fig. 1.2). The AEJ is located about 5° south of the ITF (Nicholson and Grist, 2003) and similarly moves northward in spring and retreats to the south in autumn. On a northern and on a southern track, synoptic scale disturbances with a wavelength of about 2500km, the so called African Easterly Waves (AEW) form as they move westward along the AEJ (Lafore et al., 2011) (Fig. 1.3). They are associated with dust transport between 3 to 5 km altitude during the summer (Jones et al., 2003). Dust particles are carried aloft to the mid-troposphere where they are transported westward within the AEJ and Saharan Air Layer (SAL) across the Atlantic (Karyampudi and Carlson, 1988) reaching the Amazon rain forest within 5 to 7 days (Prospero et al., 1981). On the southern track, where the AEW are fed with moist air at the ground (Nicholson and Grist, 2003), they are associated with the formation of mesoscale convective systems and strong rainfall events (Fig. 1.3) (Janiga and Thorncroft, 2016). In August, the rain band reaches its most northern position at around 20°N. Above the ocean, the band of wind discontinuity coincides with the band of maximal rainfall. However, above the continent the two lines are shifted by several 100km (Nicholson, 2009). The position of the Intertropical Convergence zone (ITCZ) is associated to both, the ITF and the band

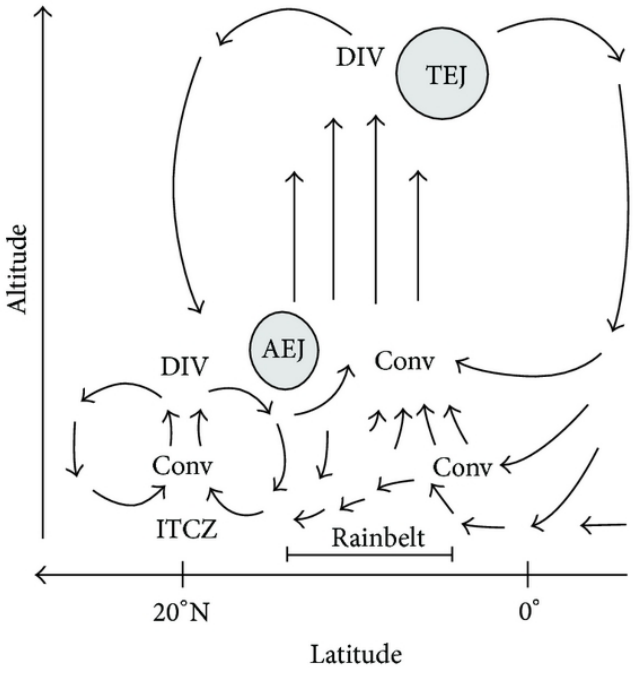

FIGURE 1.2: Schematic illustration of the West African monsoon including some of its key features: the upper-level Tropical Easterly Jet (TEJ), the mid-level African Easterly Jet (AEJ), the Intertropical Convergence Zone (ITCZ) and the position of the tropical rain belt. Reprint of Fig. 18 from Nicholson (2009).

of maximal rainfall in the literature and a explicit definition of the ITCZ is thus missing. Especially during winter, when the ITCZ and the rain belt is shifted to the south, the Bodélé Depression in central Chad is an important dust source to the West African Sahel (Cockerton et al., 2014). Additionally, northeasterly surface trade winds are essential for dust transport to the North Atlantic at altitudes below 2km especially during winter and early spring (Karyampudi and Carlson, 1988; Cook, 1999; Engelstaedter and Washington, 2007). Dust emission might be associated with cyclones at the northern margin of the African continent or Harmattan surges (Fiedler et al., 2014, 2015).

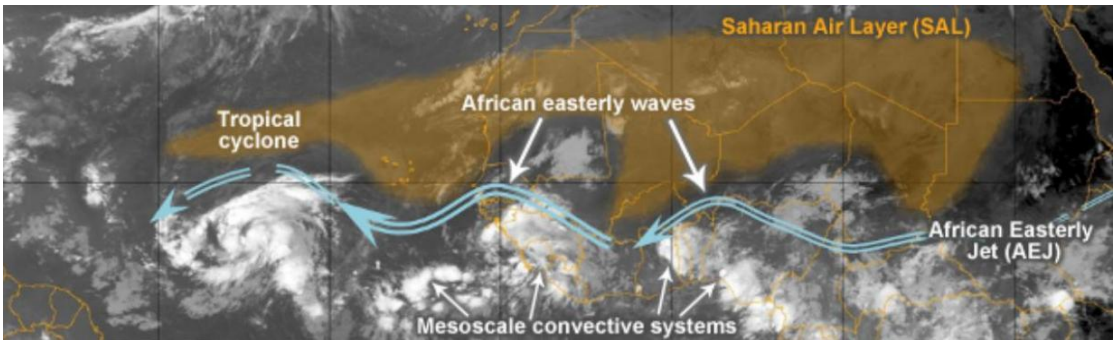

FIGURE 1.3: Major synoptic and mesoscale systems of the West African monsoon (The COMET Program/ ©EUMETSAT 2007/ US Navy/ NRL).

In the upper troposphere at around 150 hPa, the Tropical Easterly Jet (TEJ) forms probably as a consequence of increasing gradient of geopotential on the southern flank of the Saharan anticyclone that is sustained in higher altitudes (Fink, 2006). The zone of maximal rain is located between the the AEJ and TEJ at around 10°N during summer (Fig. 1.2).

1.3 The aerosol-climate model ECHAM6-HAM2

1.3.1 Physical approach of dust emission

Dust is lifted up from the surface as a consequence of strong wind events. The scale of these winds differs from small-scale convective vortices (dust devils) of some meters radius, to gust fronts of up to 1000 km width (haboobs), which arise from thunderstorm events (Harrison et al., 2001; Knippertz and Todd, 2012). To lift up particles, the wind velocity acting on the surface has to exceed a critical threshold friction velocity u_t^*, which depends on particle size, soil moisture and texture, and land cover.

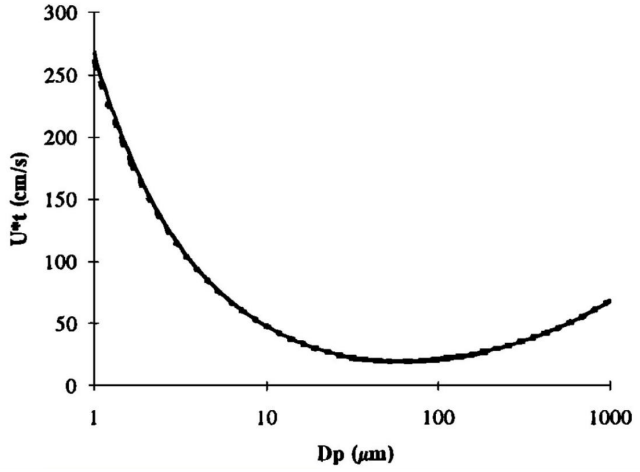

FIGURE 1.4: Relationship between threshold friction velocity U^*t and particle diameter Dp. Reprint of Fig. 1 from Marticorena and Bergametti (1995).

Surface roughness elements such as stones or vegetation enhance turbulent mixing, which decreases the wind velocity and reduces dust deflation. At the critical wind friction velocity, the strength of aerodynamic lift and drag and the strength of forces, that hold surface particles together, are balanced. Larger particles are heavier and thus more difficult to lift up due to gravity. Contrary, also for very small particles, a high threshold wind velocity has to be exceeded, because strong interparticular cohesion forces keep the particles together (Fig. 1.4).

The largest particles $>500\mu m$ are transported via a rolling motion, which is called *creeping* (Fig. 1.5). *Saltation* is the main mechanism to lift up particles from the surface. Thereby, particles within an intermediate size range (70-500μm) are hopping up to 1 meter above the surface. The drag is not sufficient to lift the particles further up and they are carried back to the surface. When hitting the surface, those particles are able to break cohesion forces between the smallest particles $<70\mu m$, which is called saltation bombardment or sand blasting. The small particles are then removed by surface winds and are further elevated through turbulent diffusion. This mechanism is called *suspension* (Shao et al., 1993).

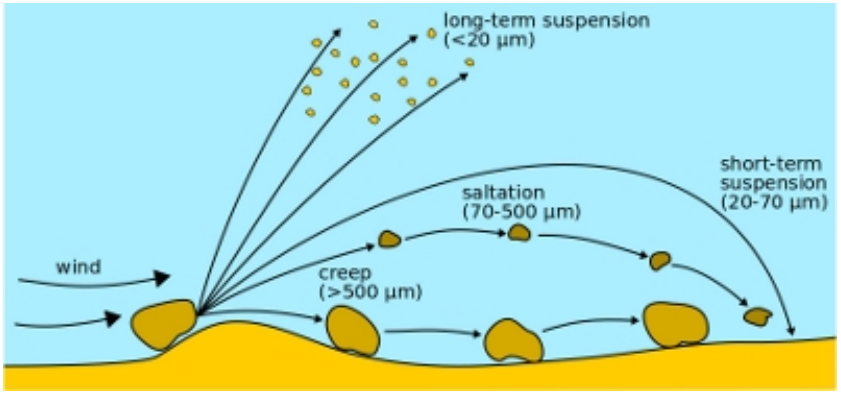

FIGURE 1.5: Dust emission processes (www.wmo.int/pages/prog/arep/wwrp/new/images/dust-uptake-400px.jpg; 21.12.2016).

1.3.2 Model description

The comprehensive aerosol-climate model ECHAM6-HAM2 (Stier et al., 2005; Zhang et al., 2012) is applied in our study. It is composed of the sixth generation of the atmospheric general circulation model ECHAM6 (Stevens et al., 2013) and an extension HAM, which incorporates atmospheric aerosols into the climate system (Stier et al., 2005). ECHAM6 is based on fundamental physical equations in combination with parametrization of small-scale processes, e.g. clouds and convection. A spectral method is applied to solve the dynamical equations. Nonlinear terms, including parametrization, are described on an almost regular Gaussian grid (Roeckner et al., 2003). In all simulations, we use a model resolution of T63L31 corresponding to a horizontal resolution of approximately 1.9°x1.9° and 31 vertical (hybrid)sigma-pressure levels in the atmosphere. The components introduced by the aerosol module HAM are mineral dust, sulphate, black carbon, organic carbon and sea salt. The aerosol concentrations from natural sources are calculated interactively in the model. In the analysis, we focus only on mineral dust.

The amount of emitted mineral dust is calculated following Tegen et al. (2002). Dust particles are grouped in 192 dust size classes with diameters ranging from 0.2 to 1300μm. After exceeding a threshold friction wind velocity, that is specific for each size class and depends on soil moisture and texture, dust fluxes increase nonlinearly as a function of wind velocity u^*. At the critical wind friction velocity, the strength of aerodynamic lift and drag and the strength of forces, that hold surface particles together, are balanced. To account for inter-particular cohesion forces, Iversen and White (1982) introduced a semi-empirical formulation, which is fitted to experimental data. Marticorena and Bergametti (1995) extended this approach by specifying a parametrization for the threshold friction velocity u_t^*, which is only a function of the particle diameter D_p (Fig. 1.4). The horizontal

flux G is calculated as:

$$G = C\frac{\rho_a}{g} \cdot u^{*3} \cdot \sum_i [(1 + \frac{u_t^*(Dp_i)}{u^*})(1 - \frac{u_t^{*2}(Dp_i)}{u^{*2}}) \cdot s_i] \text{ for } u^* \geq u_t^*. \tag{1.1}$$

C is a constant of proportionality with a value of 2.61 determined from wind tunnel experiments (White, 1979). ρ_a is the air density, g the gravitational acceleration, and s_i is the relative surface area covered by each size fraction i. The main mechanism considered in the scheme is saltation bombardment (Fig. 1.5). The finest particles are suspended in upper layers and can be transported over long distances.

Potential dust sources are defined as surface areas, where dust particles are emitted under certain conditions, e.g. the wind friction velocity has to exceed a critical limit, the soil is not covered by snow, and the upper soil layer has to be dry. They include bare soil regions and areas that are covered by sparse vegetation such as grasses, shrubs or crops. Additionally, the role of exposed paleolake beds as preferential dust sources under dry conditions is accounted for in the model. The surface material deposited in the paleolake basins is assumed to consist of silt-sized aggregates, which makes them a highly productive dust source (Tegen et al., 2002). The paleolake distribution is determined explicitly applying the high-resolution water routing and storage model HYDRA (Coe, 1998). To account for enhanced dust emission from preferential dust sources in the model, the critical threshold friction velocity, at which dust is suspended to the atmosphere, is reduced in these areas.

An effective surface ratio A_{eff} of each grid cell, which depends on the vegetation cover, is available as potential dust source. In the standard model version, temporal and spatial changes in vegetation cover are derived from satellite observations as the fraction of absorbed photosynthetically active radiation (FPAR) (Tegen et al., 2002). To make use of the model beyond times at which satellite data exist, we use a model version equivalent to Stanelle et al. (2014), where the standard version is extended to determine potential dust source areas directly depending on the land surface cover. In the land component JSBACH of MPI-ESM1, each grid cell is divided into a bare soil fraction f_{bare} and a vegetation fraction f_{veg}. The vegetated part of the grid cell is subdivided into a composition of maximal 11 plant functional types (PFT), where each PFT covers a fraction $f_{veg}(PFT)$ of f_{veg}. Based on this terminology, Stanelle et al. (2014) formulates several rules to determine potential dust sources:

- The bare soil fraction of a grid cell f_{bare} is a potential dust source.
- Dust can be emitted from areas that are covered by sparse vegetation such as grasses, shrubs or crops. These areas are considered in the model by defining a gap

fraction within the vegetated area $f_{gap}(PFT)$, which is a function of the maximum leaf area index (LAI) of the PFT.

- Snow may cover parts of the bare soil or vegetation, which prevents dust emission. The fractional area covered with snow f_{snow} is assumed to be equal for all subdivisions of the grid cell.
- Dust emission is disabled from the lake fraction of a grid cell f_{lake}.
- Dust can not be emitted if the upper most layer of the soil is wet. The skin reservoir, which is not thicker than 10^{-3}cm, is used as a measure of surface soil wetness. Dust emission is possible, if the filling of the reservoir is less than 10^{-6}cm.

In this thesis, we only consider times at which anthropogenic emissions are negligible and thus an explanation how agricultural lands are handled as potential dust sources is not necessary.

Based on these assumptions, the bare soil fraction of a grid cell acting as a potential dust source $f_{pot,bare}$ is calculated as:

$$f_{pot,bare} = (1 - f_{snow}) \cdot (1 - f_{lake}) \cdot f_{bare}. \tag{1.2}$$

The fraction of a grid cell that is covered by a specific PFT $f_{pot}(PFT)$ and is a potential dust source is given by:

$$f_{pot}(PFT) = (1 - f_{snow}) \cdot (1 - f_{lake}) \cdot (1 - f_{bare}) \cdot f_{gap}(PFT) \cdot f_{veg}(PFT). \tag{1.3}$$

In summary, the effective surface ratio A_{eff} available for dust emission is the sum of potential dust source areas:

$$A_{eff} = f_{pot,bare} + \sum_{PFT} f_{pot}(PFT). \tag{1.4}$$

The amount of fine particles, passing through a unit area of a horizontal layer per unit time, is the (vertical) dust flux D. The ratio between vertical and horizontal emission fluxes is prescribed for different soil types based on empirical measurements and depends on particle size distribution and surface properties following White (1979):

$$D = \alpha \cdot A_{eff} \cdot G \cdot I_{\theta}, \tag{1.5}$$

with $I_{\theta} = 0$ when upper-layer soil moisture is at field capacity and 1 otherwise. The horizontal flux G is given in eq. (1.1). α denotes the ratio of the vertical to the horizontal dust flux and depends on size distribution and surface properties. Soil types are clay,

silt, medium/fine sand and coarse sand (Tegen et al., 2002). Vertical emission fluxes are then integrated over all size classes and divided into aerosol modes, for which log-normal distributions are prescribed: accumulation mode (mass mean radius (mmr)=0.37 μm, standard derivation σ=1.59 μm) and coarse mode (mass mean radius (mmr)=1.75 μm, standard derivation σ=2 μm). Emission into the super-coarse mode is neglected because of the short life time of particles. During the transport, the radii of the particles can change.

Dust and all other aerosols are transported via passive tracers using a semi-Lagrangian scheme (Lin and Rood, 1996). The transport and interaction with the atmosphere is calculated according to Stier et al. (2005). Dust is removed from the atmosphere via dry deposition, sedimentation or wet deposition. Dry deposition describes the sinking of particles through downward turbulent diffusion, whereas sedimentation relates to gravitational settling. Wet deposition is the scavenging of particles by precipitation. The major part of particles in the average size range deposits due to sedimentation, whereas diffusion is only important for extremely fine particles. The proportion of wet deposition, dry deposition and sedimentation points to meteorological conditions.

1.3.3 Model validation

The global aerosol model intercomparison project AeroCom provides a framework to evaluate the performance of global aerosol-climate models and to compare to observations (Huneeus et al., 2011). The study reveals a wide spread of simulated dust emissions, atmospheric burden and depositions between the models under present-day climate, ranging across an order of magnitude, e.g. simulated emissions from North Africa, including the Sahara as the location of the most productive dust sources worldwide (Prospero et al., 2002), vary between 204 and 2888 Tga^{-1} annually.

In Table 1.1, global dust emissions, atmospheric burdens and dust depositions and North African dust emissions of the AeroCom model median are compared to those of different model versions of ECHAM6-HAM2. Simulated global dust fluxes of the latest model version echam6.3-ham2.3 are in good agreement with the AeroCom global median, while emissions from North Africa are a bit smaller in this model version. The previous model versions echam5-ham and echam6.1-ham2.1 show much lower global and regional dust fluxes that range at the lower end of the AeroCom models. The model version echam6.1-ham2.2 predicts the maximal global dust fluxes of all model versions, but lower emissions from North Africa than echam6.3-ham2.3. The simulated global dust emission exceeds that of the AeroCom median somewhat, whereas dust emission from North Africa is lower. The variations of dust fluxes among different model versions could arise from a

different implementation of atmospheric circulation which causes deviations in the wind fields. A more detailed evaluation of model version echam6.1-ham2.1 for present-day conditions is presented in Stanelle et al. (2014). The different model configurations of each chapter of this thesis are given in Table A.1 in Appendix A and are explained in detail in the model set up descriptions of each chapter, respectively.

Model	Emission [Tga^{-1}]	Emission NA [Tga^{-1}]	Burden [Tg]	Wet Dep. [Tga^{-1}]	Dry Dep. [Tga^{-1}]	Sedi. [Tga^{-1}]
AeroCom median (range)	1123 (514-4313)	792 (204-2888)	15.8 (6.8-29.5)	357 (295-1382)	396 (37-2791)	314 (22-2475)
echam5-ham (Stier et al., 2005)	664	401	8.28	374	37	265
echam6.1-ham2.1 (Stanelle et al., 2014)	912 ± 77	491 ± 66	10.9	473	83	358
echam6.1-ham2.2 (Chapter 3)	1170 ± 82	613 ± 59	17 ± 1.2	595 ± 41	110 ± 10	469 ± 36
echam6.3-ham2.3 (Chapter 4)	1137 ± 141	693 ± 93	16.7 ± 2.1	632 ± 78.6	87 ± 15	428 ± 56

TABLE 1.1: Global dust emission, burden and deposition, and emission in North Africa (NA) from the AeroCom models including echam5-ham for the year 2000, from echam6.1-ham2.1 averaged for 10 years and from echam6.1-ham2.2 and echam6.3-ham2.3 averaged for 30 years. Uncertainties in the last three rows are standard deviations of all ensemble years.

1.4 Marine sediment records

This thesis is motivated by findings that were revealed from marine sediment records. Here, we present a brief overview of the origin and location of the sediment records.

The dust records used in our study originate either from sediment traps or sediment cores. Sediment traps are installed in the ocean at different heights where they measure present-day dust fluxes in the water column. In sediment cores, dust layers have accumulated for several thousand years providing an archive of past climates. The terrigenous fraction of the observed sediment records at the marine cores (Table 1.2, Fig. 1.6) was calculated by subtracting the carbonate, opal and organic carbon percentages from the total flux following Wefer and Fischer (1993). The studies of deMenocal et al. (2000) and Adkins et al. (2006) both investigate deposition fluxes at core ODP Site 658C, but the latter

study accounts for sediment redistribution via ^{230}Th normalization similar to McGee et al. (2013a) and Williams et al. (2016). Additionally, the both latter studies apply grain size endmember modeling to separate eolian and hemipelagic fluxes. Further, Albani et al. (2015) provides an updated observational dataset of the sediment records of McGee et al. (2013a) with higher temporal resolution and information about particle size distribution. Adkins et al. (2006) assume that all of the ^{230}Th produced in the water column is efficiently scavenged to the sea floor. Hence, surface deposition fluxes are highly correlated to sediment fluxes at different depths (Table 1.2), which was confirmed by a study of Korte et al. (2017) who installed sediment traps along a transect in the North Atlantic at different heights. The abrupt change in dust deposition between 6 and 5 ka BP is clearly visible in the records of the more southern cores GC68 and ODP658 close to the margin (Fig. 1.7). Dust deposition fluxes are much lower at the northern and more remote cores, but still a somewhat steeper rise is noticeable between 6 and 2 ka BP.

No	Site	lat [°N]	lon [°W]	Depth [m]	Reference
1	ODP 659	18.1	21.0	3070	Tiedemann et al. (1989)
2	BOFS-1	19.0	20.17	3109	Bory and Newton (2000)
3	CB2-1	21.15	20.68	3502	Fischer et al. (1996)
4	CB2-2	21.15	20.69	4092	Ratmeyer et al. (1999)
5	22N25W	21.93	25.23	4120	Kremling and Streu (1993); Jickells et al. (1996)
6	25N23W	24.55	22.83	3870	Jickells et al. (1996)
7	28N22W	28.00	21.98	3600	Jickells et al. (1996)
8	CI 1 upper	29.11	15.45	3605	Ratmeyer et al. (1999)
9	VM20-234	5.33	3.03	3133	Williams et al. (2016)
10	GC 68	19.36	17.28	1396	McGee et al. (2013a); Albani et al. (2015)
11	ODP 658C	20.75	18.58	2263	Adkins et al. (2006)
12	GC 49	23.21	17.85	2303	McGee et al. (2013a); Albani et al. (2015)
13	103GGC	26.06	78.03	965	Williams et al. (2016)
14	GC 37	26.82	15.12	2771	McGee et al. (2013a); Albani et al. (2015)

TABLE 1.2: Site locations, depths and data references of marine sediment cores (1, 9, 10, 11, 12, 13, 14) and sediment traps (2, 3, 4, 5, 6, 7, 8) in the North Atlantic.

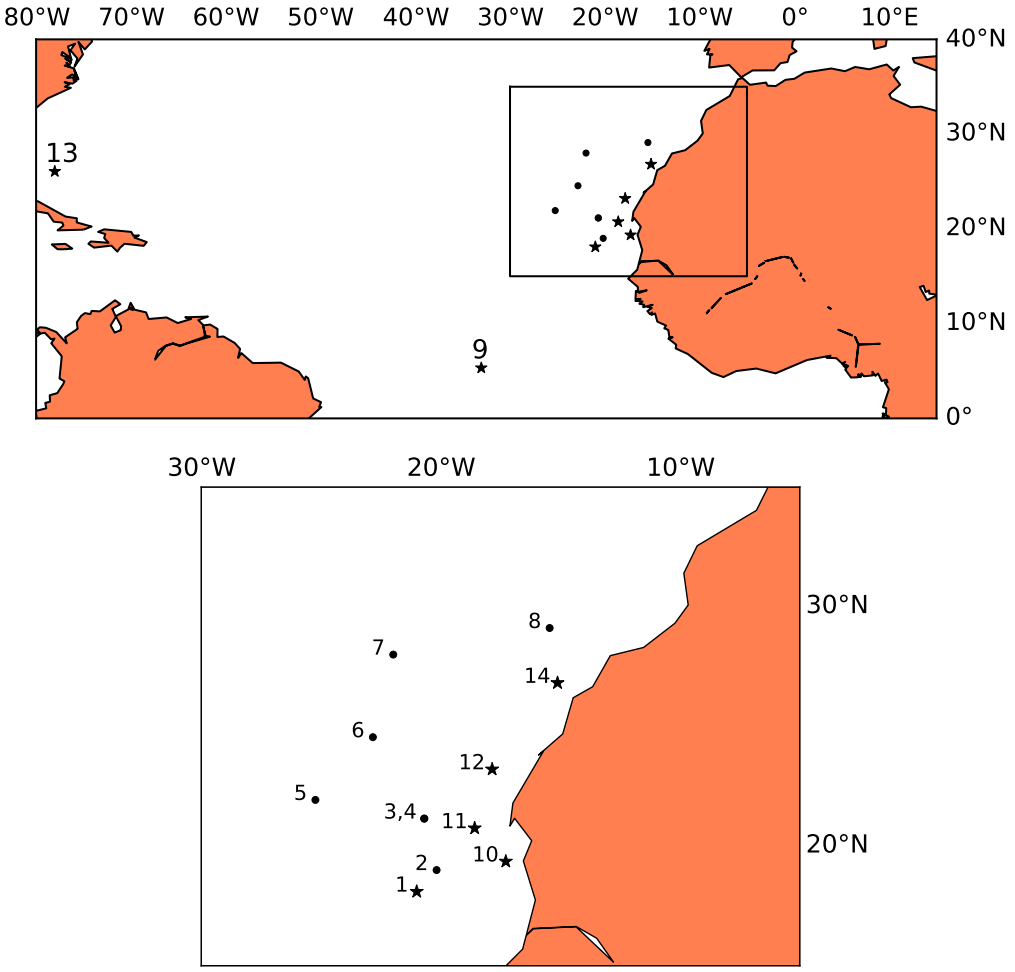

FIGURE 1.6: Site locations of marine sediment cores (marked with a star) and sediment traps (marked with a dot) remote (top) and along the northwest African margin (bottom) corresponding to Table 1.2.

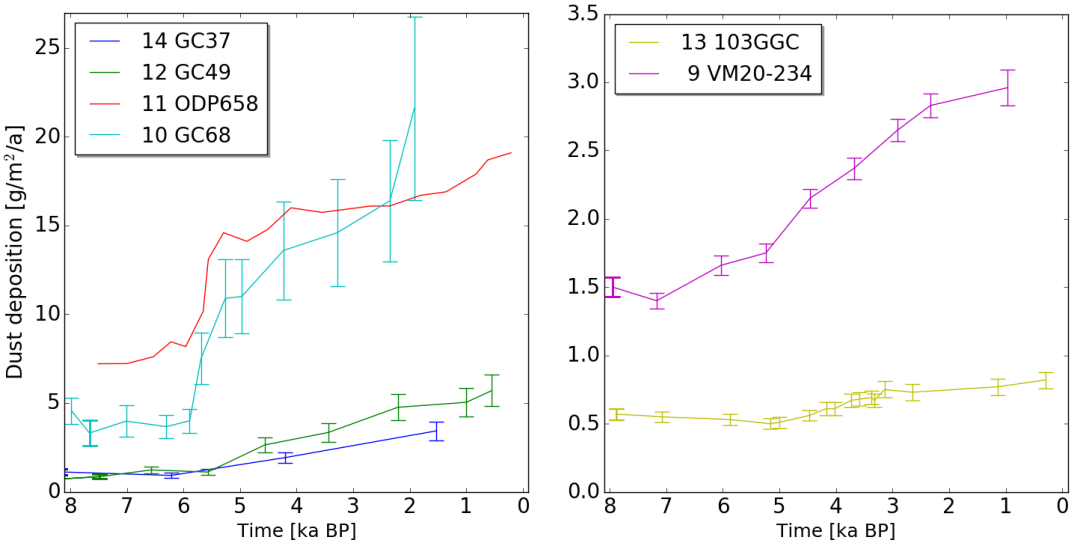

FIGURE 1.7: Dust deposition indicated by marine sediment cores close to the West African margin (left) and at the remote cores (right).

Chapter 2

Drivers of changes in Saharan dust emission and North Atlantic dust deposition during the Holocene

2.1 Introduction

Marine sediment cores along the northwest African margin reveal an abrupt and strong increase in dust accumulation in the North Atlantic of about 140% some 5.5 ka ago (Adkins et al., 2006) up to a factor of 5 about 4.9 ± 0.2 ka BP (McGee et al., 2013a). The change in dust flux has been attributed to varying Saharan vegetation cover predicted by Brovkin et al. (1998) and Claussen et al. (1999) or was related to a change in lake surface area (Cockerton et al., 2014; Armitage et al., 2015). Alternatively, the enhanced dust accumulation is linked to enhanced surface winds and a consequent intensification of coastal upwelling (Adkins et al., 2006; Bradtmiller et al., 2016). However, until now no modeling study exists that explicitly simulated the mid-Holocene dust cycle to explore the link between Saharan land surface cover and North Atlantic dust deposits at the particular location of the marine cores.

Two modeling studies of the dust cycle using general circulation models (GCMs) cover the Holocene era. Albani et al. (2015) performed simulations of a mid-Holocene and a pre-industrial time slice using the Community Earth System Model (CESM) including a Bulk Aerosol Model (CAM4-BAM). Vegetation was set to pre-industrial conditions according to PMIP/CMIP prescriptions for both time slices. For the mid-Holocene simulation, the soil erodibility was scaled for each grid cell based on vegetation cover, which was obtained offline by BIOME4 simulations. Sudarchikova et al. (2015) simulated the global dust cycle for several time slices including pre-industrial and mid-Holocene with focus

on Antarctica using the ECHAM5-HAM model. Paleoclimatic vegetation was simulated with the dynamic vegetation model LPJ-GUESS. They obtained a similar fractional vegetation cover distribution in North Africa for mid-Holocene and pre-industrial, which is in contradiction with paleorecords that specify extensive vegetation indicating a much higher vegetation cover fraction between 15°N and 23°N (Hoelzmann et al., 1998; Jolly et al., 1998b). As sparse or non-vegetated areas are potential dust sources, Saharan dust emission was thus overestimated for the mid-Holocene (results for North African dust emission presented in Sudarchikova (2012)). The extent of paleolakes was not taken into account in either study, despite the fact that areas covered by lakes lose their potential as a dust source. Accordingly, marine sediment records along the northwest African margin (deMenocal et al., 2000; Adkins et al., 2006; McGee et al., 2013a; Albani et al., 2015) indicate a lower dust accumulation rate and less dust emission in North Africa than suggested in the modeling studies. Also in Albani et al. (2015), deviations between modeled and observed dust depositions in the North Atlantic could arise from an underestimation of vegetation cover as models typically fail to capture mid-Holocene vegetation cover as indicated by proxies (Hoelzmann et al., 1998) to its full extent (Doherty et al., 2000; Irizarry-Ortiz et al., 2003; Rachmayani et al., 2015).

To overcome the shortcomings of previous simulation studies on the mid-Holocene dust cycle, we account for a more realistic land surface cover. We prescribe mid-Holocene vegetation conditions in North Africa based on reconstructions of Hoelzmann et al. (1998) and specify the distribution of paleolakes from simulations (Tegen et al., 2002). We investigate Holocene dust emission, transport and deposition explicitly as a function of Saharan land surface characteristics and atmosphere-ocean conditions. To quantify changes in marine dust deposition, we perform equilibrium simulations of the mid-Holocene (6k) and pre-industrial (0k) dust cycle using the coupled climate-aerosol model ECHAM6-HAM2 (version echam6.1-ham2.1). The investigations are guided by the following questions: Can we support the interpretation of enhanced dust accumulation seen in the marine sediment cores as a consequence of changes in North African landscape? Or can already changes in atmosphere-ocean conditions alone explain these observations? Technically, we separate the relative importance of land surface and atmosphere-ocean conditions on dust emission and deposition following the factor separation method of Stein and Alpert (1993).

Part of this chapter was published in Egerer et al. (2016).

2.2 Model setup

We perform equilibrium simulations to study the mid-Holocene (6k) and pre-industrial (0k) global dust cycle. The main setup is composed of four experiments (Table 2.1) to 1) compare with marine sediment records for both 6k and 0k (Section 2.3.1) and 2) identify the drivers of a change in dust flux between 6k and 0k (Section 2.3.2). We separate two factors: a) Saharan land surface conditions (vegetation cover and lake surface area) and b) atmosphere-ocean conditions including orbital forcing, sea surface temperature (SST) and sea ice concentration (SIC).

AO refers to atmosphere and ocean conditions. Orbital parameters are adapted to 0k and 6k respectively following Berger (1978) (Table 2.2). Prescribed SST and SIC for the pre-industrial era and the mid-Holocene respectively are taken from CMIP5 simulations with MPI-ESM (Giorgetta et al., 2013). The setup is defined following the CMIP5 protocol (Taylor et al., 2011). *LV* defines land surface conditions including lake and vegetation cover. Mid-Holocene vegetation distribution in North Africa (17°W - 40°E; 10°N - 30°N) is based on a vegetation map of Hoelzmann et al. (1998). In their approach, pollen data is linked to corresponding biomes; roughly, savanna vegetation is assumed between 10°N and 20°N and steppe vegetation between 20°N and 30°N. In the land surface component JSBACH of ECHAM6-HAM2, biomes are represented as a composition of plant functional types (PFT). Vegetation fraction and cover fractions of all eleven PFTs, surface albedo and water conductivity are set accordingly. Steppe is linked to C4 grasses and a vegetation cover of 58%. Savanna is composed of 80% C4 grasses and 20% tropical evergreen forest, where vegetation covers 80% of the land (Hagemann, 2002). Although the absolute vegetation fraction and the cover fractions of the PFTs are fixed, the leaf area index (LAI) is calculated interactively based on changes in net primary productivity (NPP) during the annual cycle. In JSBACH, a standard vegetation map for pre-industrial conditions was derived from Hagemann (2002) using satellite data. Pre-industrial and reconstructed mid-Holocene vegetation fractions are shown in Fig. 2.1. During the mid-Holocene the extent of lakes was much more pronounced than it is today (Hoelzmann et al., 1998; Gasse, 2000). Thus, the fractional lake mask in the model is adapted to a reconstruction of paleolakes from Tegen et al. (2002). They calculated the maximum possible lake extent by filling up closed topographic basins using a high-resolution water routing and storage model (see Fig. 2.1 for 0k and 6k lake fraction).

In addition to the main simulations, we perform two simulations to separate the effect of altering vegetation and lake cover under mid-Holocene atmosphere-ocean conditions. In the fifth simulation, $AO_{6k}L_{0k}V_{6k}$, mid-Holocene vegetation and pre-industrial lake distribution are prescribed. In the sixth simulation, $AO_{6k}L_{6k}V_{0k}$, only paleolakes are considered, whereas vegetation cover is set to the pre-industrial state (Table 2.1).

	Orbit	SST, SIC	Lakes	Vegetation
$AO_{0k}LV_{0k}$	0k	0k	0k	0k
$AO_{0k}LV_{6k}$	0k	0k	6k	6k
$AO_{6k}LV_{0k}$	6k	6k	0k	0k
$AO_{6k}LV_{6k}$	6k	6k	6k	6k
$AO_{6k}L_{0k}V_{6k}$	6k	6k	0k	6k
$AO_{6k}L_{6k}V_{0k}$	6k	6k	6k	0k

TABLE 2.1: Experimental setup including orbital parameters, sea surface temperature (SST) and sea ice concentration (SIC), lake and vegetation cover; 0k refers to pre-industrial and 6k to mid-Holocene conditions. While differences in AO conditions apply globally, differences in L and V conditions apply only to the Saharan box (17°W - 40°E; 10°N - 30°N).

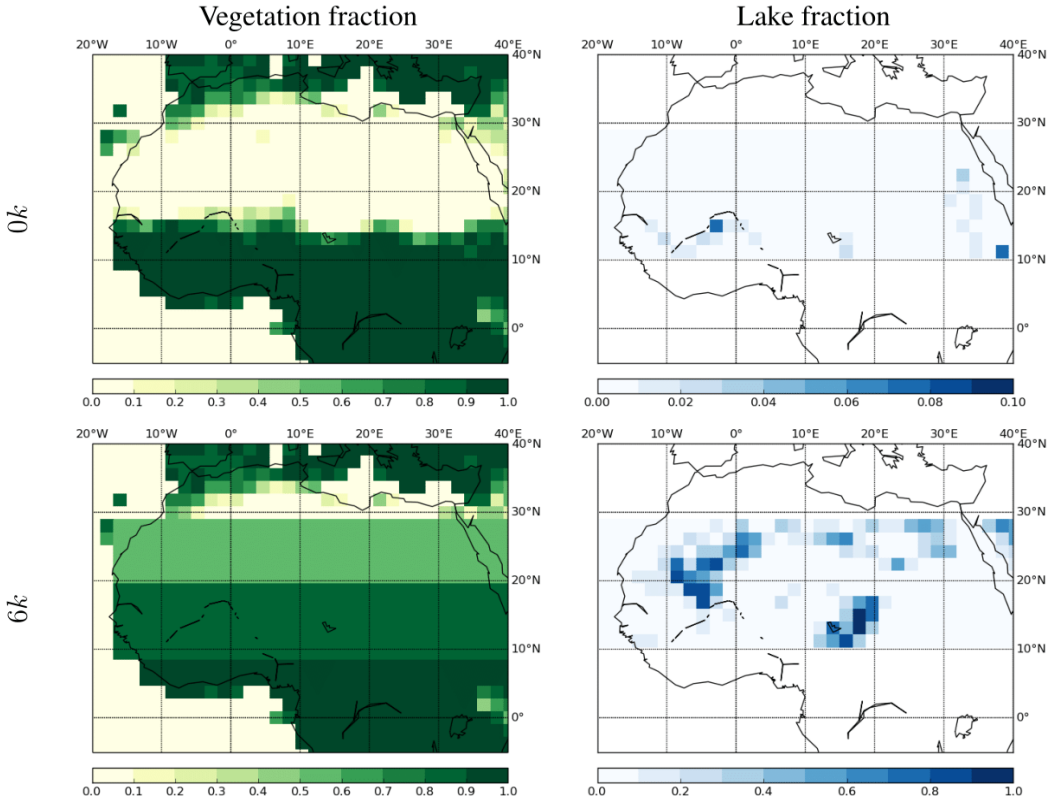

FIGURE 2.1: Vegetation and lake fraction for 0k and 6k. 6k lake fraction is obtained from Tegen et al. (2002) and 6k vegetation fraction is set following Hoelzmann et al. (1998). Note that lake fraction is scaled differently for 0k and 6k.

Each simulation is run for 31 years including one year of spin-up time. Thus, all results refer to an average of 30 years. The 6k setup, including orbital forcing parameters and greenhouse gases, is following the PMIP project standards (Harrison et al. (2001); Table

2.2). 0k and 6k greenhouse gas concentrations of CO_2, CH_4 and N_2O are set equally to 6k values of the PMIP protocol. The control run is denoted by $AO_{0k}LV_{0k}$. In this chapter, a bucket scheme is applied to handle soil moisture: As soon as the water content of the soil layer exceeds a certain threshold, evaporation from the soil stops immediately.

	0k (pre-industrial)	**6k (mid-Holocene)**
Orbital parameters:		
Eccentricity	0.016715	0.018682
Obliquity (°)	23.441	24.105
Precession (°)	102.7	0.87
Greenhouse gases:		
CO_2 (ppm)	280	
CH_4 (ppb)	650	
N_2O (ppb)	270	

TABLE 2.2: Orbital parameters derived from Berger (1978) and greenhouse gas concentrations following the PMIP protocol for 6k (Harrison et al., 2001).

2.2.1 Factor separation

To isolate the impacts of a) land surface conditions and b) atmosphere-ocean conditions on dust emission in North Africa and deposition fluxes in the North Atlantic along the northwest African margin, we apply the factor separation method of Stein and Alpert (1993) to the four main simulations $AO_{0k}LV_{0k}$, $AO_{6k}LV_{0k}$, $AO_{0k}LV_{6k}$ and $AO_{6k}LV_{6k}$. We explain the method exemplified for dust emission. The amount of emitted dust in North Africa is

$$f(s) = \int_{10°N}^{30°N} \int_{17°W}^{40°E} e_s(x,y)dxdy, \quad s \in \{AO_{0k}LV_{0k}, AO_{6k}LV_{0k}, AO_{0k}LV_{6k}, AO_{6k}LV_{6k}\} \tag{2.1}$$

where $e_s(x,y)$ is the simulated dust emission at the coordinates (x,y) for simulation s.

The total difference in dust emission in North Africa between 6k and 0k

$$\Delta_{6k-0k} = f(AO_{6k}LV_{6k}) - f(AO_{0k}LV_{0k}) \tag{2.2}$$

is divided into three components

$$\Delta_{6k-0k} = \Delta_{AO} + \Delta_{LV} + \Delta_{SYN}. \tag{2.3}$$

The contribution Δ_{AO} due to differences in orbital forcing, SST and SIC and the contribution Δ_{LV}, which captures the effects of changed land surface cover, are given by

$$\Delta_{AO} = f(AO_{6k}LV_{0k}) - f(AO_{0k}LV_{0k}), \tag{2.4}$$

$$\Delta_{LV} = f(AO_{0k}LV_{6k}) - f(AO_{0k}LV_{0k}). \tag{2.5}$$

The synergy between both factors reads

$$\Delta_{SYN} = f(AO_{6k}LV_{6k}) - f(AO_{0k}LV_{0k}) - (\Delta_{AO} + \Delta_{LV}) \tag{2.6}$$

$$= f(AO_{6k}LV_{6k}) - f(AO_{6k}LV_{0k}) - f(AO_{0k}LV_{6k}) + f(AO_{0k}LV_{0k}). \tag{2.7}$$

2.3 Results

We find the Sahara and especially the dry non-vegetated areas in Western Africa and the Bodélé Depression in the central Sahara to provide some of the most productive dust sources worldwide (Fig. 2.2), which is in agreement with satellite data (Middleton and Goudie, 2001; Engelstaedter and Washington, 2007). The patterns of deviations in dust emission between the 6k simulation and the pre-industrial control are clearly related to differences in lake patterns (Fig. 2.1), e.g. lake Mega-Chad covered the area where we find the Bodélé Depression today (Schuster et al., 2005). Also in West Africa smaller lakes and wetlands were widespread preventing dust emission.

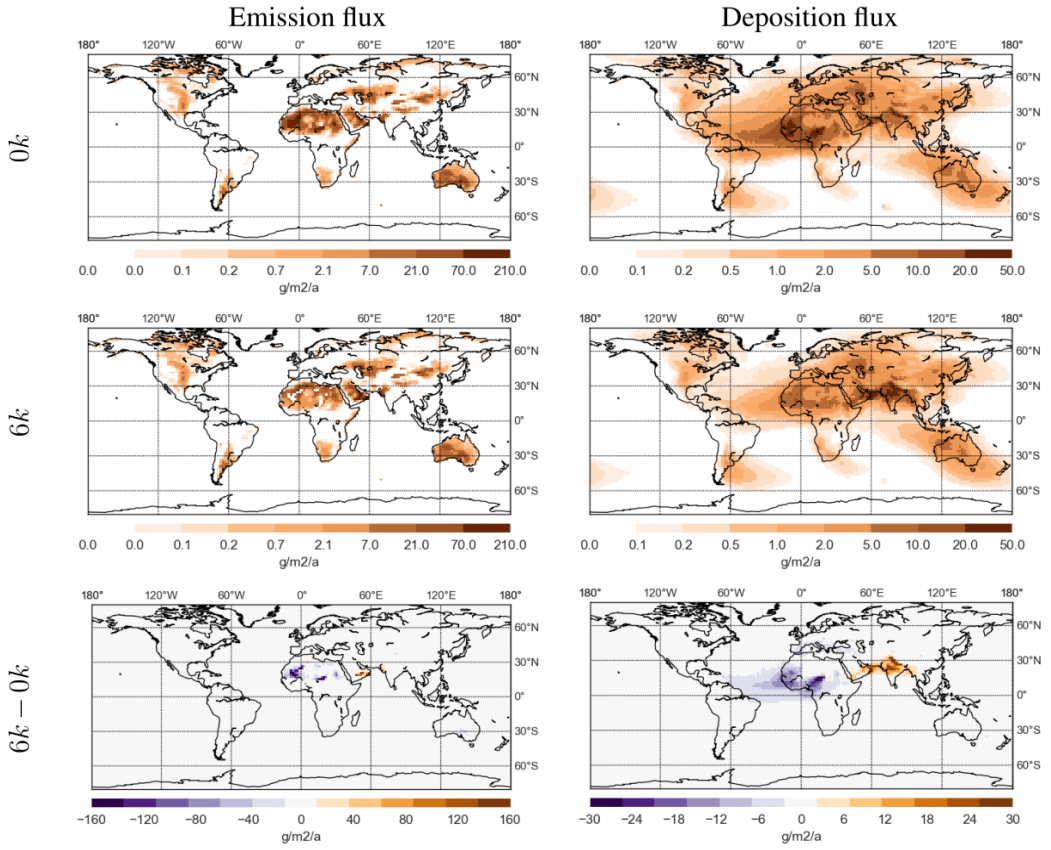

FIGURE 2.2: Simulated global annual mean dust emission flux (left) and dust deposition flux (right) for 0k, 6k and for the difference 6k-0k.

While land surface conditions were modified solely in North Africa, we notice a small area with changed dust emission in the south of the Arabian peninsula and dust depositions expanding from the south of the Arabian peninsula to the Himalayas. Detailed investigations (not shown here) reveal that these anomalies occur only during boreal summer and

we conclude that they result from a strengthening of the West African summer monsoon and a change in wind patterns (Kutzbach and Otto-Bliesner, 1982; Weldeab et al., 2007).

Saharan dust is transported across the Atlantic to the Amazon basin for 0k, which agrees with simulated deposition patterns (Fig. 2.2). They are in agreement with patterns from other modeling studies for the pre-industrial era (Mahowald et al., 1999; Tegen et al., 2002).

2.3.1 North Atlantic dust deposition: Comparison with marine sediment records

We verify our simulation results by comparing with data from marine sediment cores and sediment traps for the pre-industrial control (experiment $AO_{0k}LV_{0k}$; referred to as 0k) and for the mid-Holocene (experiment $AO_{6k}LV_{6k}$; referred to as 6k). An evaluation for both time slices is important because we are interested in differences in dust fluxes between 6k and 0k.

Numerous studies of marine sediment records provide data of dust deposition rates in the North Atlantic which are compared to our pre-industrial control simulation (see Table 1.2 and Fig. 1.6 for site locations). Only few studies present transient Holocene records of lithogenic dust fluxes in the North Atlantic along the northwest African margin between 19°N and 31°N (deMenocal et al., 2000; Adkins et al., 2006; McGee et al., 2013a; Albani et al., 2015) and more remote (Williams et al., 2016). All studies found large differences in dust deposition between the mid-Holocene and the pre-industrial era. A brief introduction to the marine sediment records is given in Section 1.4.

We obtain simulated dust deposition rates in the grid cell whose midpoint is closest to the corresponding site location. The order of magnitude of the simulated fluxes is in agreement with data for both 0k and 6k (Fig. 2.3). Simulated pre-industrial dust deposition fluxes vary between 0.97 $gm^{-2}a^{-1}$ and 18.5 $gm^{-2}a^{-1}$ compared to an observed data range of 0.82 $gm^{-2}a^{-1}$ to 22 $gm^{-2}a^{-1}$. Simulated mid-Holocene deposition fluxes vary between 0.19 $gm^{-2}a^{-1}$ and 6 $gm^{-2}a^{-1}$ and thus slightly exceed those indicated by marine sediments (McGee et al., 2013a), which range from 0.57 $gm^{-2}a^{-1}$ to 4.1 $gm^{-2}a^{-1}$ (Table 2.3). The spatial log correlation coefficient of observed and modeled values at different sites (Fig. 1.6) is 0.89 for 0k and 0.85 for 6k. Changes in dust deposition between the mid-Holocene and pre-industrial era are depicted by calculating the ratio between the 0k and 6k simulated dust deposition rates corresponding to the sediment cores of McGee et al. (2013a) and Adkins et al. (2006) (Table 2.3). At the cores close to the northwest African margin, the incremental factor of simulated dust deposition fluxes between 0k and 6k varies from 2.1 to 3.1 and increases monotonously from north to south.

McGee et al. (2013a) calculated a ratio between 3.7 and 5.4 between 0k and 6k, whereas a ratio of 2.4 was found in the study of Adkins et al. (2006). In contrast, at the remote cores VM20-234 and 100GGC, the incremental factor is much higher in our simulations, 8.4 and 5.1, compared to 2.0 and 1.4 in the marine records. Obviously, in the mid-Holocene simulation, dust particles deposit earlier and closer to the margin compared to the data, resulting in an overestimation of simulated near-margin dust deposition and an underestimation of simulated remote dust deposition.

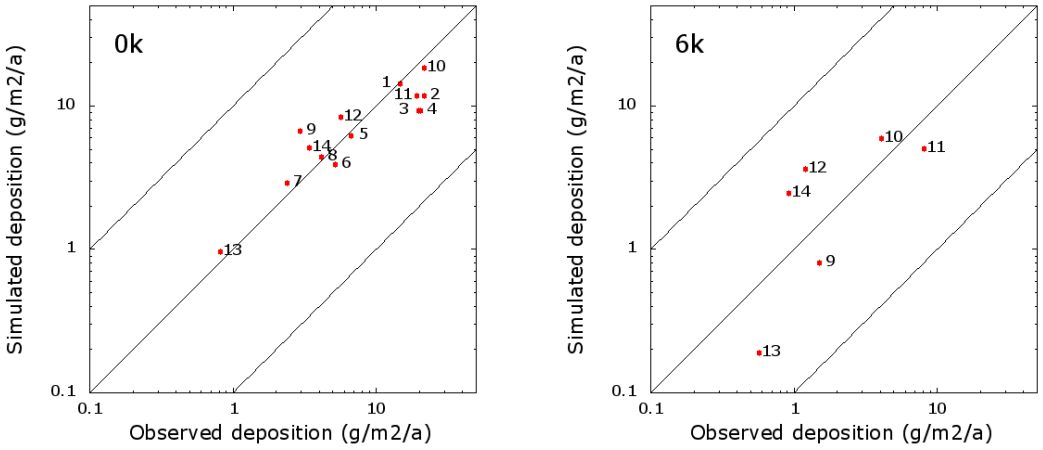

FIGURE 2.3: Simulated dust deposition flux for 0k (left, $AO_{0k}LV_{0k}$) and 6k (right, $AO_{6k}LV_{6k}$) compared with marine sediment records (Table 1.2). Log correlation coefficients are: 0.89 (0k) and 0.85 (6k).

No	Site		Dep. flux [$gm^{-2}a^{-1}$]		
			0k	6k	0k:6k
9	VM20-234	sim	6.7	0.8	8.4
		obs	3.0	1.5	2.0
10	GC 68	sim	18.5	6.0	3.1
		obs	22.0	4.1	5.4
11	ODP 658C	sim	11.9	5.0	2.4
		obs	19.2	8.1	2.4
12	GC 49	sim	8.3	3.7	2.3
		obs	5.5	1.2	4.6
13	100GGC	sim	0.97	0.19	5.1
		obs	0.82	0.57	1.4
14	GC 37	sim	5.1	2.5	2.1
		obs	3.4	0.92	3.7

TABLE 2.3: Simulated and observed dust deposition flux at the marine sediment cores (Table 1.2, Fig. 1.6) for 0k, 6k and corresponding flux ratios 0k:6k.

An increase in dust fluxes from north to south close to the northwest African margin was observed by McGee et al. (2013a). This is also seen in our model results (Fig. 2.4). To determine the north-south gradient, simulated dust deposition rates in the three ocean grid cells that are closest to the northwest African margin between 19°N and 27°N are considered (Fig. 2.4). We interpolate the simulated dust deposition fluxes linearly as a function of latitude applying the least square method (straight line in Fig. 2.4). For 0k, simulated dust deposition rates increase thus by 1.76 $gm^{-2}a^{-1}$ per degree latitude; for 6k, they increase by 0.67 $gm^{-2}a^{-1}$ per degree latitude. The north-south gradient obtained from marine sediment records (Table 1.2) differs slightly from ours with dust accumulation increasing by 2.55 $gm^{-2}a^{-1}$ per degree latitude for 0k and 1.47 $gm^{-2}a^{-1}$ per degree latitude for 6k.

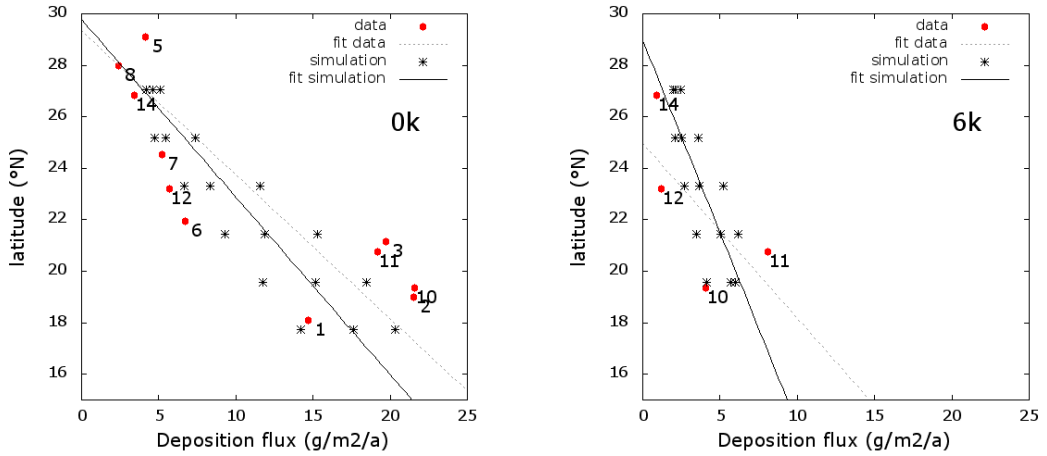

FIGURE 2.4: Simulated dust deposition flux for the three ocean grid cells that are closest to the northwest African margin for 0k (left) and 6k (right) at different latitudes compared with marine sediment records (Table 1.2). Only the marine cores which are close to the northwest African margin are considered here (Fig. 1.6, bottom). The straight lines are linear interpolations obtained with the least square method.

Additional to dust accumulation rates, McGee et al. (2013a) and Albani et al. (2015) presented particle size distributions in the marine cores. Using endmember modeling, McGee et al. (2013a) separated eolian inputs from hemipelagic inputs for 0k fluxes and presented best-fit Weibull functions to estimate the endmember contributions. We compare the size distribution of simulated deposition fluxes in the coarse mode (accounting for 98% of all aerosols) at the position of marine core GC68 to the observed dust size distribution in the sediment core as reported in Albani et al. (2015) for 0k and 6k and McGee et al. (2013a) for 0k (Fig. 2.5). Marine core GC68 is representative for the cores GC49 and GC37, since simulations and observations show a similar distribution for those cores (not shown). Note that our model output contains only the size distribution of all aerosols instead of the dust size distribution exclusively. However, the median diameter

of most other aerosols is much smaller than the one of dust. Dust is the only representative of the insoluble coarse mode. In the soluble coarse mode, only sea salt particles have an approximately similar mass mixing ratio as mineral dust. The concentration of the remaining aerosols is insignificant. In our model output, we find a similar aerosol median diameter for soluble and insoluble particles. Thus, we assume that the aerosol size distribution in the coarse mode obtained from our model output is in principle representative for the dust size distribution. We notice a quite similar particle size distribution for 0k and 6k in our model results (Fig. 2.5). This is in agreement with data and model results of Albani et al. (2015), who stated that during the Holocene the temporal variability of the dust size distribution is very limited. Compared to sediment records of Albani et al. (2015) and McGee et al. (2013a), the simulated mean aerosol diameter is relatively small (Fig. 2.5). Mahowald et al. (2014) pointed out that the atmospheric surface concentrations are in general finer than the ones deposited in marine cores because coarser particles are removed preferentially from the atmosphere whereas finer particles are transported further downwind to the Atlantic Ocean. The particle size distribution in our study refers to dust deposition fluxes at the ocean's surface, which is finer than the accumulated dust in the deep ocean. The mean diameter of simulated deposited dust particles is in average higher than the one obtained from simulated atmospheric surface concentrations along the northwest African margin of Mahowald et al. (2014; Fig. 8k,l) but smaller than of observed values (Mahowald et al. 2014; Fig. 8k).

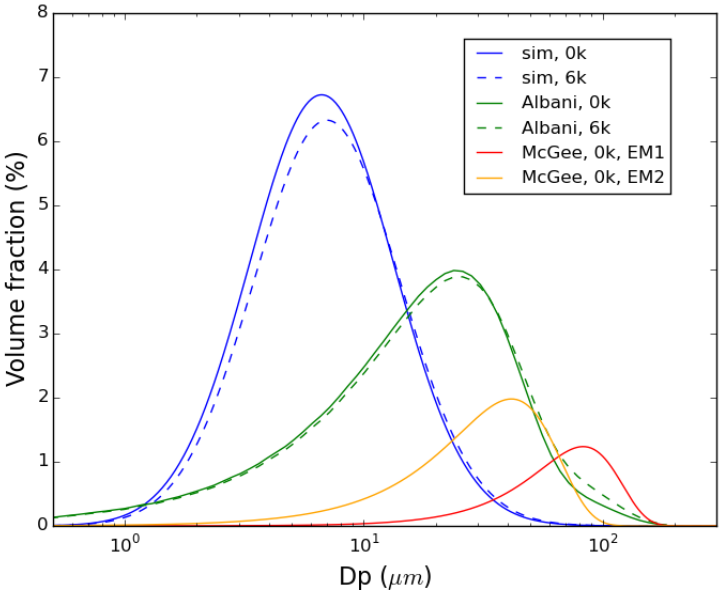

FIGURE 2.5: Simulated aerosol size distribution of deposited fluxes in the coarse mode at the position of marine core GC68 (blue), dust size distribution in the marine core of Albani et al. (2015) (green) for 0k (solid) and 6k (dotted) and best-fit Weibull functions that represent the contribution of the endmember (EM) corresponding to eolian inputs (EM1 (red) and EM2 (orange)) in McGee et al. (2013b)) for 0k. Curves are normalized to an area of 1.

2.3.2 Influence of land surface conditions and atmosphere-ocean conditions on dust emission and deposition

The simulated dust emission, atmospheric burden, total deposition and precipitation in North Africa (17°W–40°E; 10°N–30°N) and the global life time of dust in the atmosphere for all experiments are summarized in Table 2.4. Additionally, percentages of wet deposition, dry deposition and sedimentation of the total deposition are presented. Standard deviations of the 30 year dust emission ensemble are given.

Exp.	Emission [Tga^{-1}]	Burden [Tg]	Wet Dep. [%]	Dry Dep. [%]	Sedi. [%]	Total Dep. [Tga^{-1}]	Global life time [day]	Precip. [mm day^{-1}]
$AO_{0k}LV_{0k}$	352.6 ± 44.3	2.62	20.6	9.6	69.8	144.9	4.4	0.66
$AO_{6k}LV_{0k}$	360.5 ± 29.4	2.73	34.4	6.6	59.0	165.3	4.3	0.93
$AO_{0k}LV_{6k}$	107.8 ± 12.3	1.04	43.4	4.7	51.9	70.2	3.7	1.79
$AO_{6k}LV_{6k}$	96.1 ± 15.4	0.99	51.1	3.9	45.0	72.0	3.7	1.97
$AO_{6k}L_{0k}V_{6k}$	174.2 ± 28.8	1.69	47.2	3.2	49.6	100.9	4.1	1.72
$AO_{6k}L_{6k}V_{0k}$	177.7 ± 18.7	1.38	41.0	6.4	52.6	101.6	3.6	1.24

TABLE 2.4: Dust emission, burden, deposition and precipitation in North Africa (17°W - 40°E; 10°N - 30°N) and global life time of dust for altering atmospheric and ocean (AO) and land surface conditions (LV).

Pre-industrial land surface conditions result in much higher dust emissions compared to mid-Holocene land surface conditions, independently of atmospheric and ocean boundary conditions. Emissions in North Africa are 3.3 to 3.8 times higher for AO_xLV_{0k} compared to AO_xLV_{6k} with $x \in \{0k, 6k\}$. Dust deposition rates and the dust burden in the atmosphere above North Africa increase by a factor of 2.1 to 2.3 and 2.5 to 2.8, respectively. In experiment $AO_{6k}LV_{0k}$, the dust cycle is enhanced only slightly compared to the pre-industrial control ($AO_{0k}LV_{0k}$). On the other hand, for mid-Holocene land surface cover (LV_{6k}), mid-Holocene atmosphere-ocean conditions reduce emission and enhance deposition slightly (compare $AO_{0k}LV_{6k}$ and $AO_{6k}LV_{6k}$ in Table 2.4).

Is the suppression of dust emission by land surface conditions due to increased lake surface area or rather linked to enhanced vegetation cover? In experiments $AO_{6k}L_{0k}V_{6k}$ and $AO_{6k}L_{6k}V_{0k}$, we change lake surface area and vegetation cover separately; one is set to 6k conditions, while the other one remains in the pre-industrial state. In either experiment, dust emission is approximately halved and deposition reduces to about 70% compared to the pre-industrial control (Table 2.4). Emission and deposition fluxes are still higher than fluxes obtained with fully mid-Holocene land surface cover. The burden is slightly higher for $AO_{6k}L_{6k}V_{0k}$ compared to $AO_{6k}L_{0k}V_{6k}$. In conclusion, paleolakes and mid-Holocene vegetation both contributed nearly to the same extent to a reduced dust cycle during the mid-Holocene.

About 20.6% of the simulated total deposition in North Africa is due to wet deposition for the pre-industrial control ($AO_{0k}LV_{0k}$) compared to about 51.1% for mid-Holocene conditions ($AO_{6k}LV_{6k}$) corresponding to increased annual rainfall from 0.66 mm day^{-1} to 1.97 mm day^{-1} (Table 2.4). Consequently, the global life time of dust in the atmosphere decreases from 4.4 to 3.7 days when mid-Holocene land surface is prescribed because particles are washed out more rapidly from the atmosphere. This result is almost unaffected by a change in orbit and ocean conditions. Only about 41% of Saharan dust is deposited in the emission area for pre-industrial conditions. Hence, a large amount of dust is transported downwind beyond North Africa to the North Atlantic and even reaching to the Amazon area (Fig. 2.2). In contrast, the ratio of deposited versus emitted dust in North Africa is about 75% for mid-Holocene conditions, which is related to shorter life times, enhanced rainfall and a higher impact of wet deposition.

2.3.3 Factor analysis of controls on dust emission and deposition

We separate the impacts of a) land surface conditions and b) atmosphere-ocean conditions on dust emission in North Africa and North Atlantic deposition fluxes along the northwest African margin applying the factor separation method of Stein and Alpert (1993) as briefly introduced in Section 2.2.1. In Table 2.5, the total difference Δ_{6k-0k}, the contribution Δ_{AO} due to differences in orbital forcing, SST and SIC, the contribution Δ_{LV}, which captures the effects of changed land surface cover, and the synergy between both factors Δ_{SYN} are presented for dust emission in North Africa and deposition along the northwest African margin. Differences due to changes in land surface conditions Δ_{LV} vary not more than 5% from the total differences Δ_{6k-0k}. We conclude that changes in land surface cover are the main driver of changes in dust emission in North Africa and associated changes in dust deposition along the northwest African margin during the Holocene. The impact of atmosphere-ocean conditions Δ_{AO} is even slightly negative for dust emission and has a negative effect of 16.5% of the total difference for dust deposition

in the North Atlantic. The synergy effect accounts for 7.6% of dust emission and 20.4% of dust deposition.

	Δ_{6k-0k} [Tga^{-1}]	$\Delta_{AO}/\Delta_{6k-0k}$	$\Delta_{LV}/\Delta_{6k-0k}$	$\Delta_{SYN}/\Delta_{6k-0k}$
Emission	-256.5	-3.1%	95.4%	7.6%
Deposition	-26.6	-16.5%	96.1%	20.4%

TABLE 2.5: Difference in simulated dust emission in North Africa (17°W–40°E; 10°N–30°N) and simulated dust deposition along the northwest African margin (30°W–17°W; 5°N–35°N) between 6k and 0k and contribution of land surface conditions, atmosphere-ocean conditions and synergy effects to the total difference.

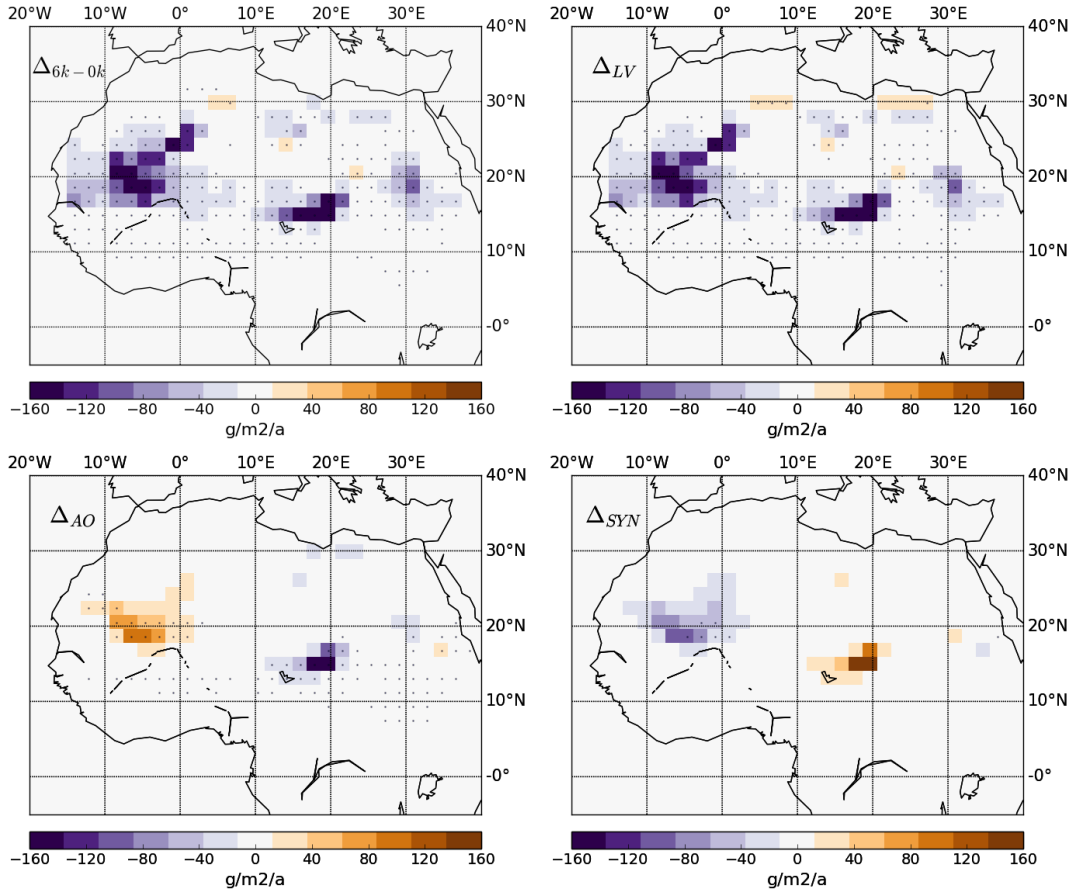

FIGURE 2.6: Differences in simulated dust emission in North Africa (17°W–40°E; 10°N–30°N) between 6k and 0k, Δ_{6k-0k} (top left), Δ_{LV} (top right), Δ_{AO} (bottom left) and the synergy effect Δ_{SYN} (bottom right). Hatched areas show significant differences on 99% confidence level.

Comparing patterns of dust emission in North Africa (Fig. 2.6) and North Atlantic dust deposition (Fig. 2.7) visually, highlights the large impact of land surface conditions. The patterns of the contribution Δ_{LV} and the total difference Δ_{6k-0k} are almost identical. Mid-Holocene atmosphere-ocean conditions with fixed pre-industrial land surface ($AO_{6k}L_{0k}$) lead only to local changes in dust emission. Interestingly, we find an increase

in dust emission from the Western Sahara, whereas less dust is emitted from the Bodélé Depression. Dust deposition in the North Atlantic does not differ significantly compared to the control and is even slightly enhanced between 10°N and 15°N.

Relating Fig. 2.6 to Fig. 2.7, this analysis demonstrates that emission in North Africa is directly linked to deposition in the North Atlantic along the northwest African margin. In our simulations, we identify land surface conditions to be the main control on dust emission and deposition with a contribution of more than 95%. Changes in dust transport due to changes in atmospheric processes alone play a minor role.

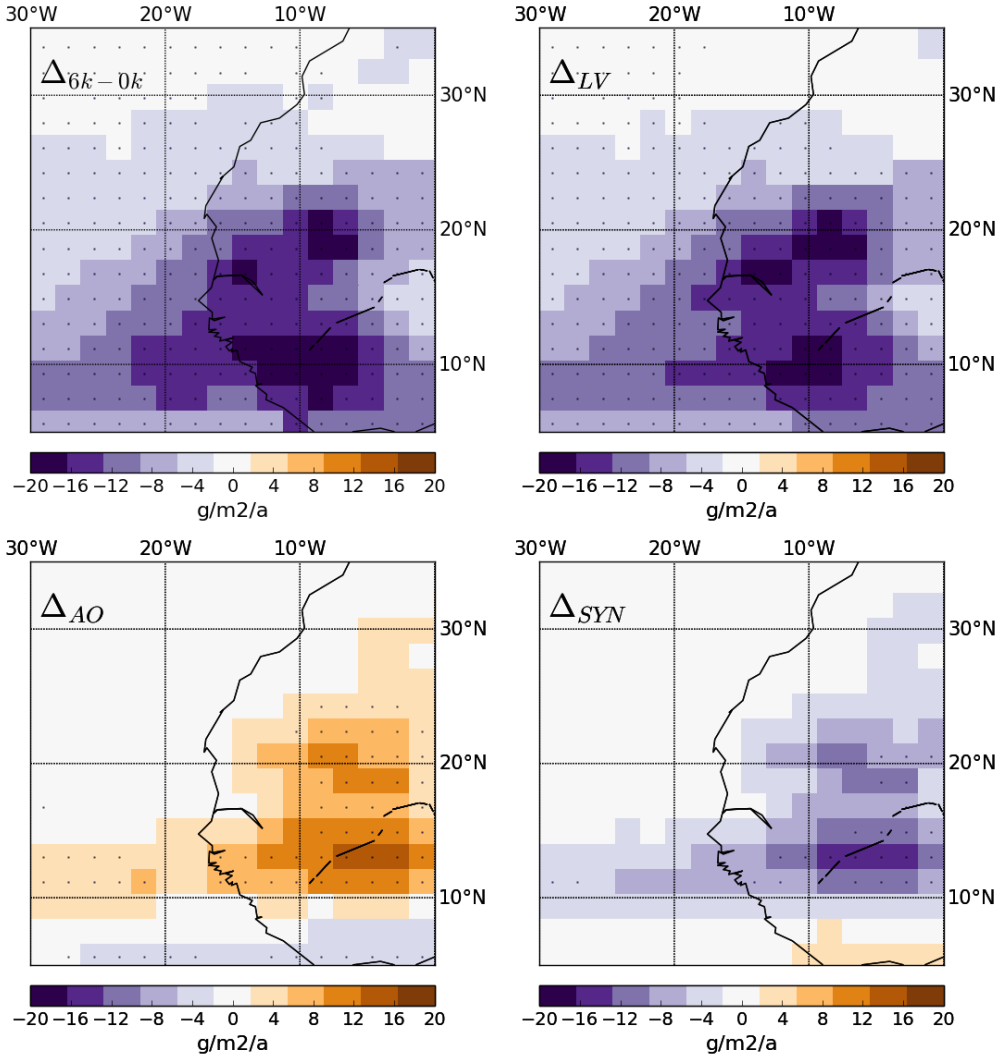

FIGURE 2.7: Differences in simulated dust deposition along the northwest African margin (30°W–17°W; 5°N–35°N) between 6k and 0k Δ_{6k-0k} (top left), Δ_{LV} (top right), Δ_{AO} (bottom left) and the synergy effect Δ_{SYN} (bottom right). Hatched areas show significant differences on 99% confidence level.

2.3.4 Annual cycle of dust emission

An analysis of the annual cycle of dust emission in relation to meteorological conditions is provided to get a deeper understanding of our simulation results. We present the annual cycle of dust emission for our main experiments and relate them to annual wind patterns.

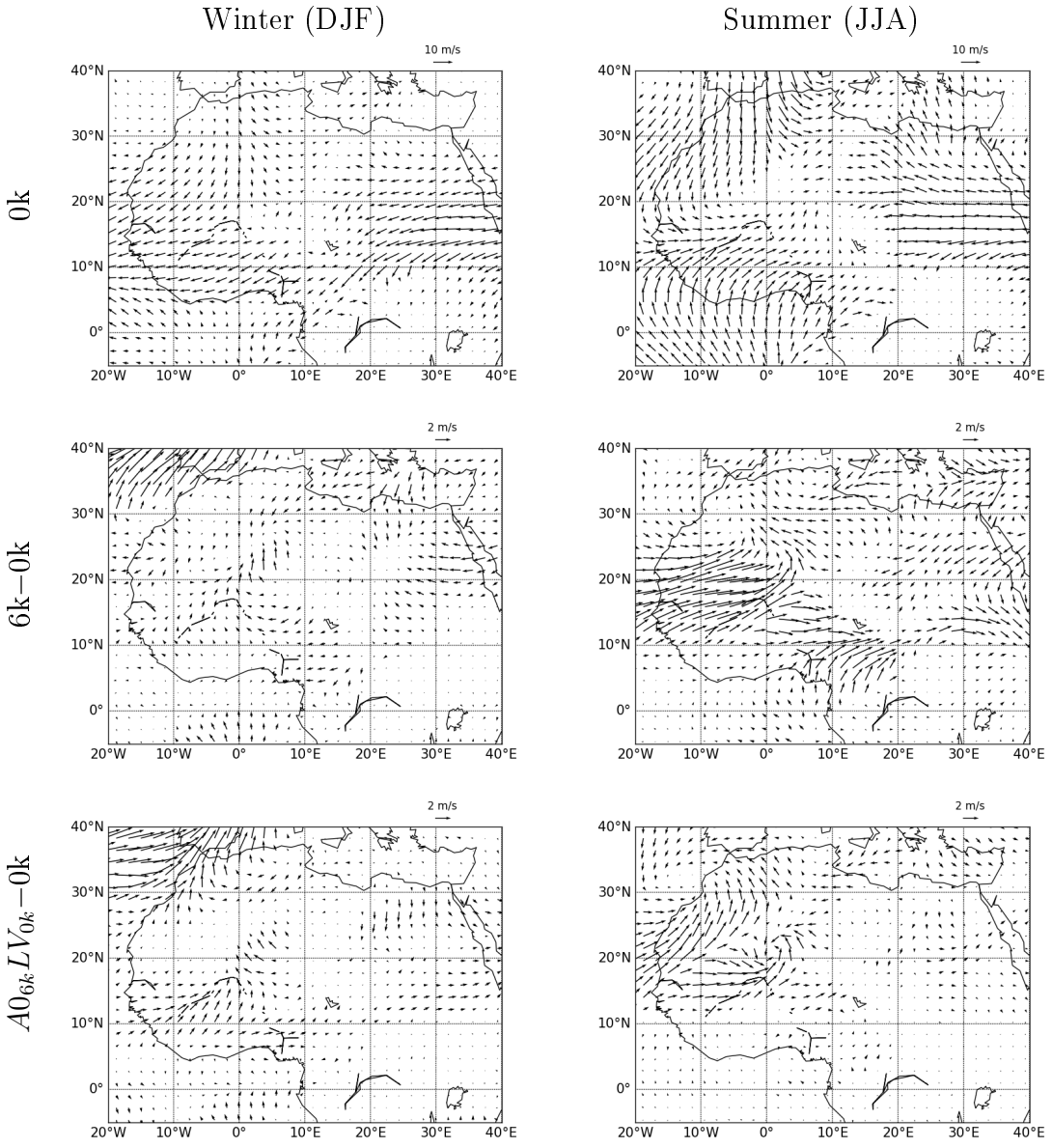

FIGURE 2.8: Simulated 10m wind speed and directions for winter (DJF; left) and summer (JJA; right) for 0k and for the differences 6k−0k and $A0_{6k}LV_{0k}-0k$.

North African dust emission is linked to a distinct annual cycle (Engelstaedter and Washington, 2007). Northeasterly near surface trade winds below 1000m height are responsible for the majority of dust transport from the Saharan desert toward the North Atlantic during the winter and early spring (Ratmeyer et al., 1999; Engelstaedter and Washington, 2007). In our simulations, northeasterly winds are strongest along the coast during winter and spring (Fig. 2.8, top). Accordingly, maximum dust emission rates occur from February till April (Fig. 2.9). Additionally, towards the summer, dust is lifted up and transported by the Saharan Air Layer (SAL) (Carlson and Prospero, 1972), that is coupled to the African Easterly Jet at 1000m to 5000m height (Tiedemann et al., 1989). Accordingly, we notice a second smaller peak of dust emission around June in the control run. Dust activity decreases towards the end of the year in all regions (Fig. 2.9). The Bodélé Depression in central Chad is active throughout most of the year. In this region, dust is emitted and lifted up by Harmattan winds. The annual cycle of simulated dust emission in our study is in agreement with regional observations (Pye, 1987), satellite data (Herman et al., 1997) and a modeling study of the modern dust cycle (Werner et al., 2002). Mid-Holocene wind patterns hardly change during winter compared to the pre-industrial control, whereas during the summer months, the ITCZ propagates further north (Fig. 2.8, middle). Surface winds from the Eastern Atlantic Ocean to the Sahel area in the southwest induced by the West African monsoon intrude further north. Consequently, the transport of dust from North Africa to the North Atlantic is reduced.

If orbital forcing is adjusted to mid-Holocene conditions and pre-industrial land surface is kept ($AO_{6k}LV_{0k}$), we obtain only a slight increase in annual dust emission (Section 2.3.2) in our simulations, but the annual cycle changes significantly (Fig. 2.9, bottom left). The corresponding patterns of simulated dust emission show enhanced dust productivity in the Western Sahara compared to the control run (Section 2.3.3), where dust productivity increases towards the summer (Engelstaedter and Washington, 2007). Accordingly, dust emission is maximal during summer (June to August) in our simulation. Although the total amount of annual dust emission hardly changes, there is a clear shift in source regions and the annual cycle when only mid-Holocene atmosphere-ocean conditions are set. This is most likely due to a change in the contribution of processes that are responsible for dust emission during the Holocene. A further in-depth analysis of important meteorological processes on dust emission for the mid-Holocene remains to be assessed. Dust emission is strongly prevented throughout the year when mid-Holocene vegetation and lakes are prescribed (LV_{6k}). Hereby, the annual cycle of dust emission is closely linked to seasonal plant growth. The leaf area index and the soil moisture increase during the summer months, when the West African monsoon becomes active. Nonetheless, the change of atmosphere-ocean conditions from 0k to 6k tends to shift the

time of maximal dust productivity from March-May to May-July (compare $AO_{0k}LV_{6k}$ and $AO_{6k}LV_{6k}$).

The analysis of the annual cycle of dust emission shows that mid-Holocene land surface cover suppresses dust emission throughout the year, which results in reduced annual dust emission. Although mid-Holocene atmosphere-ocean conditions do not result in a significant reduction of the total annual amount of emitted dust in North Africa, they affect the atmospheric circulation, what is reflected in a changed annual cycle and a shift of dust source regions.

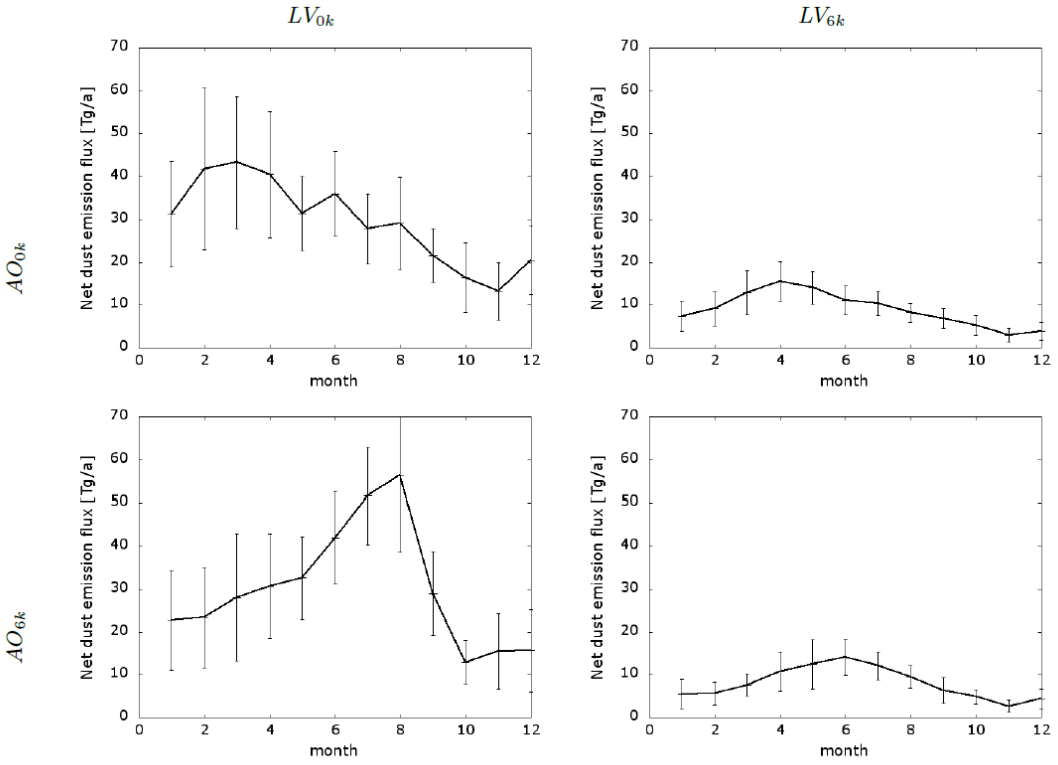

FIGURE 2.9: Mean annual cycle of simulated dust emission for altering atmosphere-ocean (AO) and land surface (LV) conditions in North Africa (17°W–40°E; 10°N–30°N).

2.3.5 Simulated mid-Holocene and pre-industrial climate conditions

We investigate changes in simulated temperature, precipitation and wind between the experiments and the pre-industrial control run, and compare to results of the third phase of the Paleoclimate Modelling Intercomparison Project (PMIP3) (Braconnot et al., 2011, 2012) and paleo evidence (Bartlein, 2011) to ensure that Holocene climate variability is sufficiently well presented in our model.

Temperature

Two opposing effects influence Holocene temperature changes in the Sahara (Hales et al., 2004): Increased evapotranspiration due to enhanced vegetation, extended lake surface area and wetter soils cools the climate, whereas the lower albedo of vegetation, lake surface and wet soils increases the amount of absorbed solar radiation resulting in a warming of the surface (Charney, 1975). In the $AO_{6k}LV_{0k}$ simulation, where only the oceans and orbital forcing are adapted to mid-Holocene conditions, we find a surface cooling of up to 2K in the Sahel due to the strengthening of the West African monsoon in the summer months (Fig. 2.10). These changes in simulated temperature are consistent with those of the PMIP model mean (Braconnot et al., 2012). In the simulations with enhanced prescribed vegetation and lakes (LV_{6k}), the surface cooling in the Sahel is increased. At the same time, the albedo effect is dominant in the more northern and more arid regions resulting in a surface warming of up to 5K. This is consistent with paleo evidence which predicts a surface warming of between 2K and 10K in the northern Sahara (Bartlein, 2011). However, in most of the PMIP models, the surface warming in the northern Sahara could not be reproduced because the vegetation does not extend as far north as indicated by pollen records (Jolly et al., 1998b). Consequently, less incoming solar radiation is absorbed by the surface due to the higher albedo of the unvegetated soil. In the northwest Sahara, where lakes are widespread, there is only a slight surface warming in our LV_{6k} simulations because both, evapotranspiration and albedo effect, are nearly balanced. In the 6k simulation, the surface cooling is slightly stronger in the Sahel and southern Sahara and the surface warming is slightly weaker in the northern Sahara compared to the $AO_{0k}LV_{6k}$ simulation because the monsoon intrudes a bit further north.

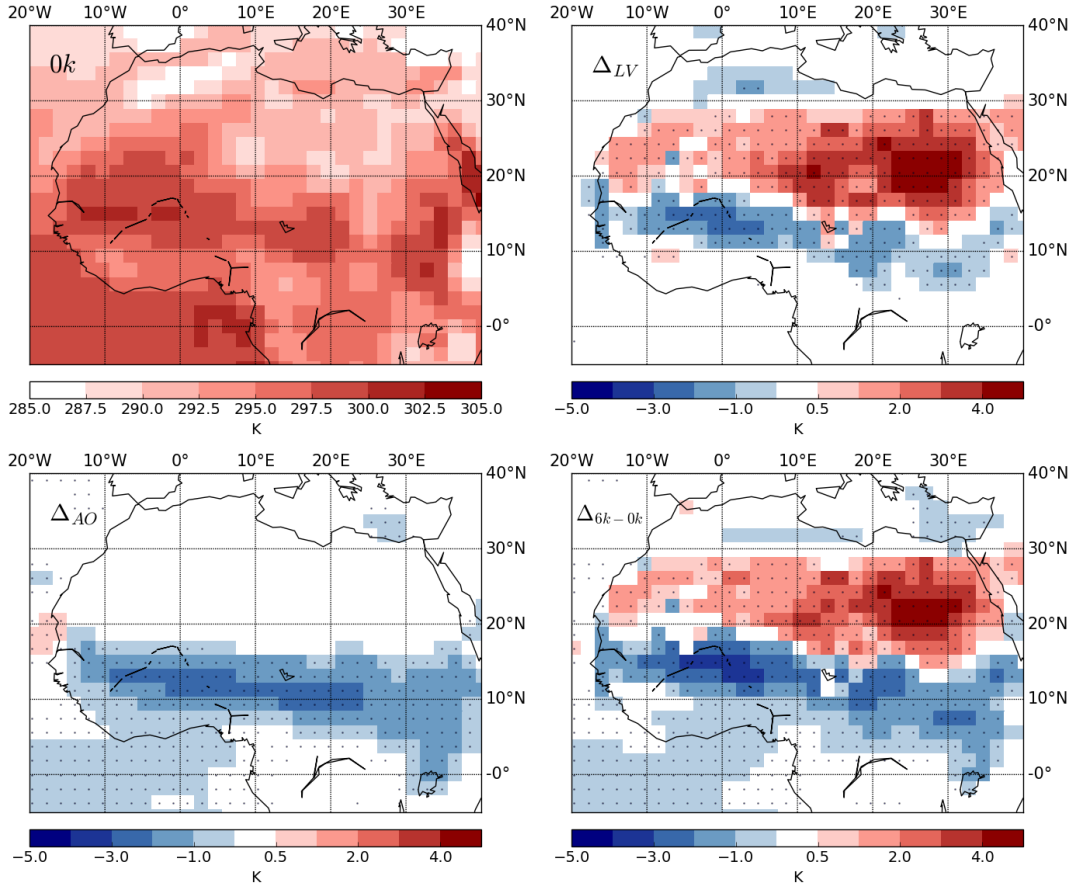

FIGURE 2.10: Simulated mean annual temperature for 0k (top left) and for the differences Δ_{LV} (top right), Δ_{AO} (bottom left) and Δ_{6k-0k} (bottom right). Hatched areas show significant temperature differences on 99% confidence level.

Precipitation

Increased evapotranspiration and lower albedo during the mid-Holocene both result in higher rainfall (Hales et al., 2004). Precipitation is enhanced up to 1 mm/day in the Sahel for the $AO_{6k}LV_{0k}$ simulation compared to the pre-industrial control (Fig. 2.11), which is consistent with the PMIP results (Braconnot et al., 2012). In general, global circulation models (GCM) underestimate the extent of the North African summer monsoon and precipitation during the mid-Holocene (Braconnot et al., 2007; Perez-Sanz et al., 2014). Several studies emphasize the role of land surface-precipitation feedbacks as crucial to simulate realistic mid-Holocene climate conditions in North Africa (Claussen et al., 1999; Irizarry-Ortiz et al., 2003; Rachmayani et al., 2015).

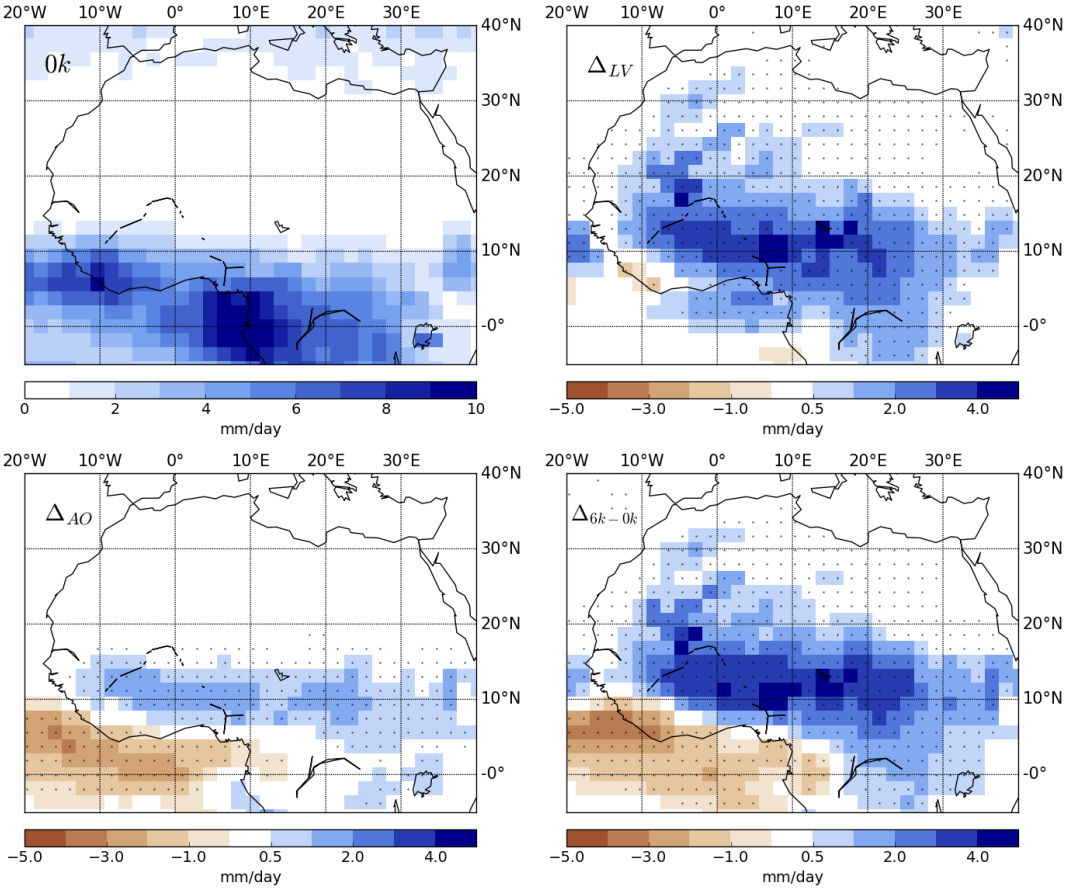

FIGURE 2.11: Simulated mean annual precipitation for 0k (top left) and for the differences Δ_{LV} (top right), Δ_{AO} (bottom left) and Δ_{6k-0k} (bottom right). Hatched areas show significant precipitation differences on 99% confidence level.

In the 6k simulation, precipitation increases up to 4 mm/day in the Sahel compared to the pre-industrial control due to enhanced vegetation and lake surface area. Between 10°N and 18°N, the model overestimates the increase in precipitation compared to paleo evidence (Bartlein, 2011), but north of 18°N an increase of 1-2 mm/day in North Africa seems realistic. Precipitation changes in the 6k simulation and the $AO_{0k}LV_{6k}$ simulation are very similar (Fig. 2.11). This indicates that vegetation and lakes are dominant in enhancing rainfall during the mid-Holocene, whereas the additional effect of changed orbit and ocean conditions is minor. Regarding the dust cycle, enhanced vegetation cover and lake surface area do not only have a direct effect by covering source areas and hence suppressing dust emission, but additionally land surface-precipitation feedbacks cause enhanced washing out of particles by rainfall.

Wind

We notice a weakening of northeasterly winds of about 3-4 m/s during the summer in the 6k simulation compared to the control (Fig. 2.8, middle), whereas northeasterly winds decrease about 2 m/s in experiment $AO_{6k}LV_{0k}$. Changes in wind patterns are most

likely related to a northward shift of the monsoon and enhanced precipitation during the summer. Because the increase in precipitation during the mid-Holocene is not underestimated in our simulation $AO_{6k}LV_{6k}$ in contrast to most GCM mid-Holocene experiments, we ensure that changes in wind patterns are reasonable in our study. Northeasterly winter winds do not change very much, neither in simulation $AO_{6k}LV_{0k}$ nor in simulation $AO_{6k}LV_{6k}$ (Fig. 2.8). This is in contrast to Bradtmiller et al. (2016), who suggest a significant decrease in winter surface winds as the cause of a reduction in coastal upwelling and productivity during the mid-Holocene. This may be related to a general underestimation of high-speed wind events in GCMs (e.g. Capps and Zender (2008)).

In the pre-industrial control, we identify the AEJ with its core located at around 500 hPa between 10°N and 15°N and the TEJ at 200 hPa height between 5°N and 8°N (Fig. 2.12). A shift in orbit and ocean conditions (simulation $AO_{6k}LV_{0k}$) causes a northward shift of the AEJ, which is amplified due to mid-Holocene land surface conditions in simulation $AO_{0k}LV_{6k}$ and $AO_{6k}LV_{6k}$. Also, the TEJ is strengthened. Easterly surface winds are weaker between 15°N and 20°N for $AO_{6k}LV_{0k}$ and up to 27°N in the 6k simulation, primarily due to the weakening of northeasterly summer winds (Fig. 2.8).

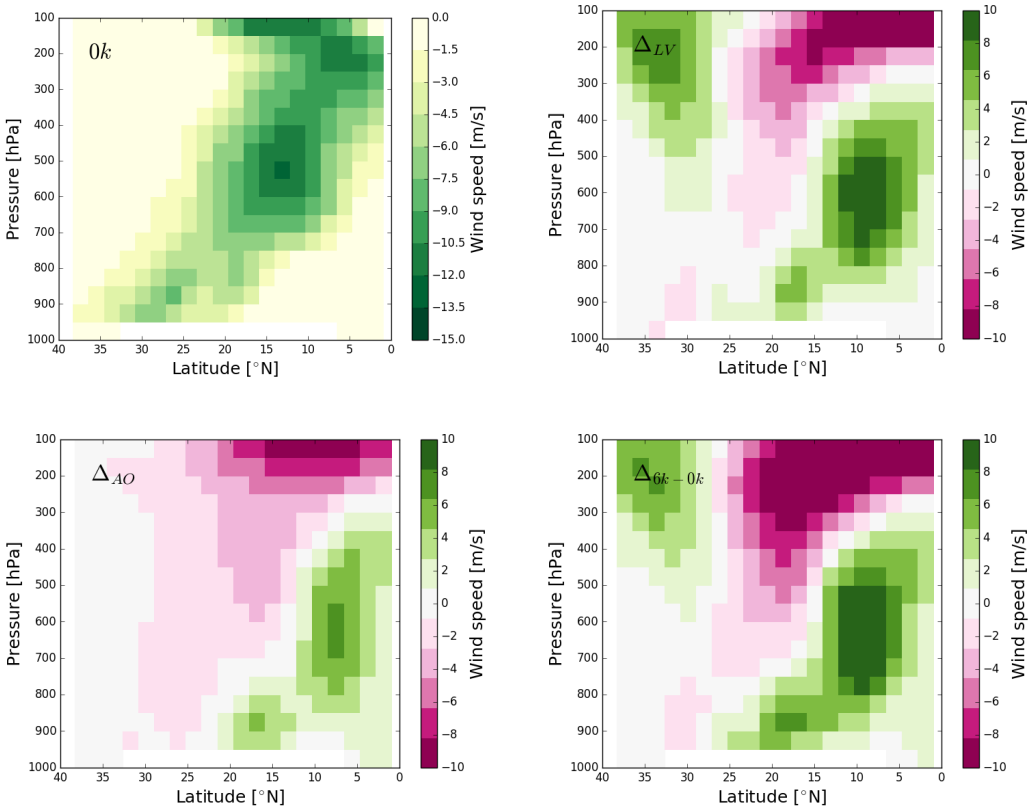

FIGURE 2.12: Simulated mean zonal wind speed during summer (JJA) for 0k (top left) and for the differences Δ_{LV} (top right), Δ_{AO} (bottom left) and Δ_{6k-0k} (bottom right).

2.4 Discussion and conclusions

We have explored whether the sudden increase in dust deposition fluxes into the North Atlantic between the mid-Holocene (6 ka BP) and the pre-industrial era (1850 AD) as indicated by marine sediments (deMenocal et al., 2000; Adkins et al., 2006; McGee et al., 2013a; Albani et al., 2015) were induced by variations in North African land surface cover or rather related to a change in atmosphere-ocean conditions. We have analyzed the relative contribution of these drivers to a change in Saharan dust emission and North Atlantic dust deposition by simulating the dust cycle for both eras. In our simulations, orbital forcing parameters and ocean conditions are adjusted respectively and mid-Holocene land surface conditions are fixed according to vegetation reconstructions from pollen data (Hoelzmann et al., 1998) and simulations of lake surface area (Tegen et al., 2002).

We find decreased dust activity in North Africa during the African Humid Period (AHP) at 6 ka BP, where dust emission fluxes from the Saharan desert are reduced to about 27% of pre-industrial fluxes and associated dust deposition in the North Atlantic is reduced by a factor between 2.1 and 3.1 for specific site locations along the northwest African margin. The latter result is consistent with a marine sediment record of Adkins et al. (2006) that indicates lower deposition fluxes by a factor of 2.4 for the mid-Holocene compared to pre-industrial, but not with the records of McGee et al. (2013a), who find an average factor of 4.5 for the corresponding sites. McGee et al. (2013a) argue that the amplitude of a change in dust flux is underestimated by Adkins et al. (2006) because the record does not separate eolian and fluvial/shelf inputs. The relatively low contrast of mid-Holocene and pre-industrial fluxes in our study compared to McGee et al. (2013a) arises from higher simulated mid-Holocene deposition rates in the North Atlantic, whereas simulated pre-industrial fluxes are approximately similar to the data. In contrast, simulated mid-Holocene dust deposition is lower compared to dust records of more remote sites close the Bahamas and in the tropical North Atlantic (Williams et al., 2016). This is because in our simulations, particles deposit earlier and closer to the margin compared to observations. Despite the uncertainties in quantifying dust deposition fluxes, prescribing land surface cover according to paleorecords (Hoelzmann et al., 1998) reduces the deviation between simulated deposition and dust accumulation from marine records for the mid-Holocene compared to previous simulation studies (Albani et al., 2015). Comparing dust deposition fluxes at the surface to deep sea sediment accumulations while disregarding ocean currents and other disturbances could entail biases in the fluxes. However, Ratmeyer et al. (1999) argued that in the area of the chosen cores, there is a fast and mostly undisturbed downward transport of lithogenic material in the

water column. Thus, sedimentation fluxes mostly correlate well between upper and lower ocean depths and the surface.

Our simulations show a north-south increase of dust deposition rates along the northwest African margin during the mid-Holocene and pre-industrial era, which is consistent with observations of McGee et al. (2013a). The increase in dust deposition with decreasing latitude can presumably be attributed to the wind climatology. According to NCEP reanalysis data (Kalnay et al., 1996), present-day surface winds increase from north to south along the northwest African margin and can thus transport higher amounts of dust to the ocean. We have compared the particle size distribution in the marine sediment cores presented by Albani et al. (2015) and McGee et al. (2013b) with the particle size distribution of simulated aerosol deposition fluxes. In agreement with marine records (Albani et al., 2015), we find neither large spatial nor temporal variability in Holocene particle size distribution. Compared to observations of Albani et al. (2015) and McGee et al. (2013b), the simulated mean aerosol diameter is relatively small. Partially, the discrepancy in size arise because dust particles at the ocean's surface are in general finer than those accumulated in the deep ocean. But in general, models underestimate the particle size distribution compared to observations (Mahowald et al., 2014), e.g. van der Does et al. (2016) found particles as large as 200μm in sediment traps in the North Atlantic.

We identify land surface cover to be the main control on dust emission in North Africa and associated dust deposition in the North Atlantic. It potentially covers dust sources and alters the atmospheric circulation. The direct link between patterns of dust emission fluxes in North Africa and deposition fluxes in the North Atlantic is demonstrated via a factor separation analysis. Enlarged lake surface area and expanded vegetation cover contribute equally to the reduced dust cycle of the mid-Holocene, although paleolakes covered a much smaller area than vegetation. Paleolakes suppressed dust emission completely on a particular area, whereas vegetation was spread out in the whole Sahara, but gaps in between grasses and shrubs still enabled dust emission. Additionally, the West African monsoon propagates further north during mid-Holocene summer. The enhanced rainfall in more northern areas contributes to the reduction of dust transport by effectively washing out particles from the atmosphere.

During the mid-Holocene, vegetation of low stature, such as grasses and shrubs, was predominant in North Africa. Due to the patchy distribution of the vegetation (Jolly et al., 1998b), there still remained larger areas of bare soil, which served as potential dust sources. In the model, dust emission from these vegetated areas is implemented in the following way: A grid box is divided into fractions of bare soil and vegetation. In addition to the bare soil areas, the model accounts for 'gaps' within the vegetated

area, where dust emission can occur (Stanelle et al., 2014). Thus, although a relatively high vegetation fraction is prescribed for the mid-Holocene (58% for steppe and 80% for savanna), our model predicts a reasonable amount of emitted dust. Biases may occur from the rather simplistic reconstructed vegetation cover of (Hoelzmann et al., 1998) as homogeneous vegetation is prescribed for a large area due to the lack of detailed information on vegetation cover. A more diverse vegetation cover could influence near surface winds. Dust emission occurs only above a threshold wind velocity and is very sensitive to changes in near surface winds. Hence, the distribution of vegetation surely influences dust emission locally. Nevertheless, we assume that the total amount of emitted dust and the corresponding deposited amount of dust in the North Atlantic is not significantly affected by a uniform vegetation distribution.

The prescribed mid-Holocene lake surface area rather represents the potential maximum lake extent from filling up topographic depressions assuming unlimited water supply (Tegen et al., 2002). As a results, lakes cover about 12% of North Africa in our mid-Holocene simulation, whereas paleo reconstructions indicate a lake surface area of about 7.6% (Hoelzmann et al., 1998). Thus, dust emission is underestimated in our mid-Holocene simulation because more dust sources are disabled by lakes. Considering this bias, it seems likely that the relative importance of vegetation cover on the suppression of dust emission is higher than the one of lakes.

In addition to the direct suppression of mid-Holocene dust emission by extended land surface cover, land surface-precipitation feedbacks further reduce dust transport and deposition by changing wind and precipitation patterns (Coe and Bonan, 1997; Claussen et al., 1999; Rachmayani et al., 2015). In our simulations, these feedbacks are reflected by enhanced precipitation and a higher fraction of wet deposition compared to dry deposition and sedimentation during the mid-Holocene. Due to enhanced precipitation, dust particles are washed out more rapidly from the atmosphere. The fraction of wet deposition of the total deposition increases from about 20% at 0k to about 51% at 6k corresponding to a three times higher amount of rainfall and a decrease in global life time of dust. The partitioning of the direct masking effect by vegetation and lake surface cover and the indirect effect of land surface-climate feedbacks on a suppression of dust emission remains to be assessed. Mid-Holocene atmosphere-ocean conditions alone (experiment $AO_{6k}LV_{0k}$) affect the total amount of emitted and deposited dust only marginally compared to the control. They have, however, an impact on the annual dust cycle and dust source regions. In experiment $AO_{6k}LV_{0k}$, precipitation in the southern Sahara is enhanced by about 1 mm/day compared to 0k and the monsoon propagates further north during summer. Nevertheless, the amount of precipitation and the northward propagation of the West African monsoon during summer is underestimated in comparison with paleo evidence (Bartlein, 2011). This bias is common to most PMIP models (Braconnot

et al., 2012; Perez-Sanz et al., 2014). We found that in experiment $AO_{6k}LV_{6k}$, where additionally a more realistic mid-Holocene land surface is prescribed, changes in precipitation between 6k and 0k are even overestimated in the southern Sahara and are in agreement with paleodata of Bartlein (2011) north of 20°N. Also, changes in temperature that are indicated by paleo data (Bartlein, 2011) are captured satisfactorily in the simulations. Uncertainties in the simulated physical climate that arise from model biases for pre-industrial times are reported in Giorgetta et al. (2013) for MPI-ESM1 (including ECHAM6 as the atmospheric component) in the frame of CMIP5. They mention a dry bias in the tropics over land north of the equator at present-day. However, since differences in precipitation between 6k and 0k are in agreement with paleo evidence, we assume that the bias has no significant effect. A weakening of northeasterly winds in experiment $AO_{6k}LV_{6k}$ of about 3-4 m/s compared to the pre-industrial control and of 2 m/s in experiment $AO_{6k}LV_{0k}$ was found during summer, which is related to the enhanced monsoon and precipitation. Weakened surface winds during winter are related to a reduction in coastal upwelling during the mid-Holocene as noted by Adkins et al. (2006) and Bradtmiller et al. (2016). In our simulations, we do not find a substantial change in northeasterly winter winds during the Holocene which might be due to a general underestimation of high-speed wind events by the relatively coarse global-scale GCMs (e.g. Capps and Zender (2008)).

The implications of an abrupt increase in dust deposition on the characterization of the Holocene landscape transformation remains to be assessed: Do land surface-climate feedbacks generate a sudden reduction of vegetation cover or lake surface area, resulting in a sudden exposure of dust source areas? Or can the abrupt change in dust deposition in the North Atlantic be interpreted as a nonlinear response of Saharan dust emission to a gradually changing surface? These questions are addressed in the upcoming chapters.

Chapter 3

Could gradual changes in Holocene Saharan landscape have caused the observed abrupt shift in North Atlantic dust deposition?

3.1 Introduction

An abrupt increase in dust deposition within centuries is seen in marine sediment records along the northwest African margin between 19°N and 27°N some 5 ka ago (deMenocal et al., 2000; Adkins et al., 2006; McGee et al., 2013a). Modeling studies show an abrupt decrease of vegetation cover due to amplifying vegetation-climate feedbacks (Brovkin et al., 1998; Claussen et al., 1999), vegetation-soil feedbacks (Janssen et al., 2008) or due to a nonlinear response of vegetation to precipitation (Liu et al., 2007). Alternatively, the sharp fall of lake levels at the end of the AHP (Gasse, 2000; Lézine et al., 2011) has been attributed to positive feedbacks between precipitation and surface waters (Krinner et al., 2012). These positive feedbacks could favour multiple stable states enabling the rapid transition from a highly vegetated humid state to a hyperarid desert state under a gradually developing orbital forcing (Brovkin et al., 1998; Claussen, 1998). The sudden decline of vegetation and lake levels may result in a rapid activation of dust sources and an associated abrupt increase in North Atlantic dust deposition (deMenocal et al., 2000).

In contrast, a more gradual vegetation decline, extending over several millennia, was found in other modeling studies (Renssen et al., 2003) and was indicated by paleoenvironmental records from the eastern Sahara (Kröpelin et al., 2008; Shanahan et al.,

2015). Two arguments seemingly support that even a gradual decline of vegetation and lakes may have led to abrupt dust deposition changes in the North Atlantic during the Holocene: 1) a vegetation fraction threshold argument and 2) a latitudinal threshold argument. For the first argument, one might expect that the smaller surface roughness length of reduced vegetation cover results in a strengthening of surface winds. Dust emission is proportional to the cube of the wind surface velocity, as long as a threshold value of wind surface velocity for dust mobilization is exceeded. This was confirmed by observations in the field and by wind tunnel experiments (Shao et al., 1993). The high sensitivity of dust emission to changes in wind speed may force a sudden increase of dust release when the vegetation fraction falls below a certain threshold. The second argument is based on the assumption that vegetation and lakes shifted southward during the Holocene as a consequence of the West African monsoon retreat (Lézine et al., 2011; Shanahan et al., 2015). Thereby, highly productive dust sources that today feed the marine cores may have become active in a short period of time despite a gradual retreat of the summer monsoon. Especially desiccated paleolake basins in Western Africa or in the Bodélé depression provide fine grained material that can be activated easily (Prospero et al., 2002). In both scenarios, changes in wind systems implied by the changed land surface might additionally influence the dynamics of dust emission and transport. Yet, published simulations that include interactive dust are restricted to specific time slices, e.g. present-day (Tegen et al., 2002), pre-industrial and mid-Holocene (Albani et al., 2015; Egerer et al., 2016) and the last glacial maximum (Mahowald et al., 1999). Thus, they are not suitable for investigating the relation between the dynamics of North Atlantic dust deposition and Holocene Saharan landscape changes.

In this chapter, we perform two series of equilibrium simulations using the coupled aerosol-climate model ECHAM6-HAM2 (version echam6.1-ham2.2) to explore the effect of a gradual retreat of vegetation and lakes on North Atlantic dust deposition. To do so, we construct two scenarios, each addressing one of the above mentioned arguments: 1) a prescribed gradual and spatially homogeneous decrease of vegetation cover and lake surface area over North Africa, and 2) a prescribed gradual southward retreat of vegetation and lakes. In both scenarios, the overall North African land surface cover is prescribed for several states as a stepwise linear decrease. We investigate whether either of these scenarios results in an abrupt change in simulated dust deposition at the grid cells around the marine sediment cores due to a vegetation fraction threshold on dust emission or due to a latitudinal threshold on dust emission. If instead gradually changing land cover entails a gradual change in North Atlantic dust deposition, we argue that the rapid changes observed in dust proxy records can only be explained by a more rapid landscape transformation. Thereby, this study contributes to the longstanding debate

of whether the mid-Holocene 'green' Sahara converted abruptly or more gradually to today's hyperarid desert. Part of this chapter was published in Egerer et al. (2017).

3.2 Model setup

We simulate dust emission, transport and deposition as a function of North African vegetation cover and lake surface area for the pre-industrial (pi) and the mid-Holocene (mh) state. Additionally, we introduce five intermediate land cover states (I1, I2, ..., I5), for which the vegetation cover fraction and lake surface area decrease stepwise linearly from one state to another.

Pre-industrial and mid-Holocene vegetation are prescribed as latitudinal bands of biomes based on a vegetation reconstruction of Larrasoaña et al. (2013) (Fig. 3.1). In their study, past woody cover fraction was determined from $\delta^{13}C$ data of paleosol carbonates. North African savanna biomes are mixed tree-grass communities characterized by a discontinuous tree canopy. Depending on the woody cover fraction, Larrasoaña et al. (2013) distinguish three savanna types: woodland, wooded grassland and grassland. We represent these biomes as a composition of plant functional types (PFT) in the land component JSBACH of ECHAM6-HAM2 following Hagemann (2002) (Table 3.1). Woodland is represented as a mixture of 50% C4 grasses and 50% tropical evergreen forest with a total vegetation cover of 95%. Wooded grassland is characterized by 80% vegetation cover composed of 80% of C4 grasses and 20% of tropical evergreen forest. Grassland solely consists of C4 grasses and occupies 58% of the land surface. In total, we obtain a mean vegetation fraction of about 77% during the mid-Holocene and about 38% for the pre-industrial reconstruction. Due to the darker and more humid soil of vegetated ground, a soil albedo of 0.18 and a maximum soil moisture depth of 0.655m is set for all biomes (Dallmeyer, 2008). Non-vegetated areas are desert with a soil albedo of about 0.3 and a maximum soil moisture depth of 0.3m. In this chapter, a bucket scheme is applied to handle soil moisture, similar to Chapter 2. The contribution of vegetation to the surface albedo changes seasonally in the model depending on the leaf area index (LAI). Although the vegetation fraction and the cover fractions are fixed, the LAI is calculated interactively based on seasonal changes in temperature and soil water availability.

Mid-Holocene paleolakes are prescribed following a reconstruction of Tegen et al. (2002) similar to Egerer et al. (2016) occupying about 12% of the surface which is clearly higher than 7.6%, which was obtained by paleolake reconstructions of Hoelzmann et al. (1998). The pre-industrial lake distribution is represented fairly well by a standard lake mask for present-day in JSBACH, which is based on satellite data (Loveland et al., 2000). Only about 0.2% of Northern Africa is covered by lakes today (Fig. 3.1).

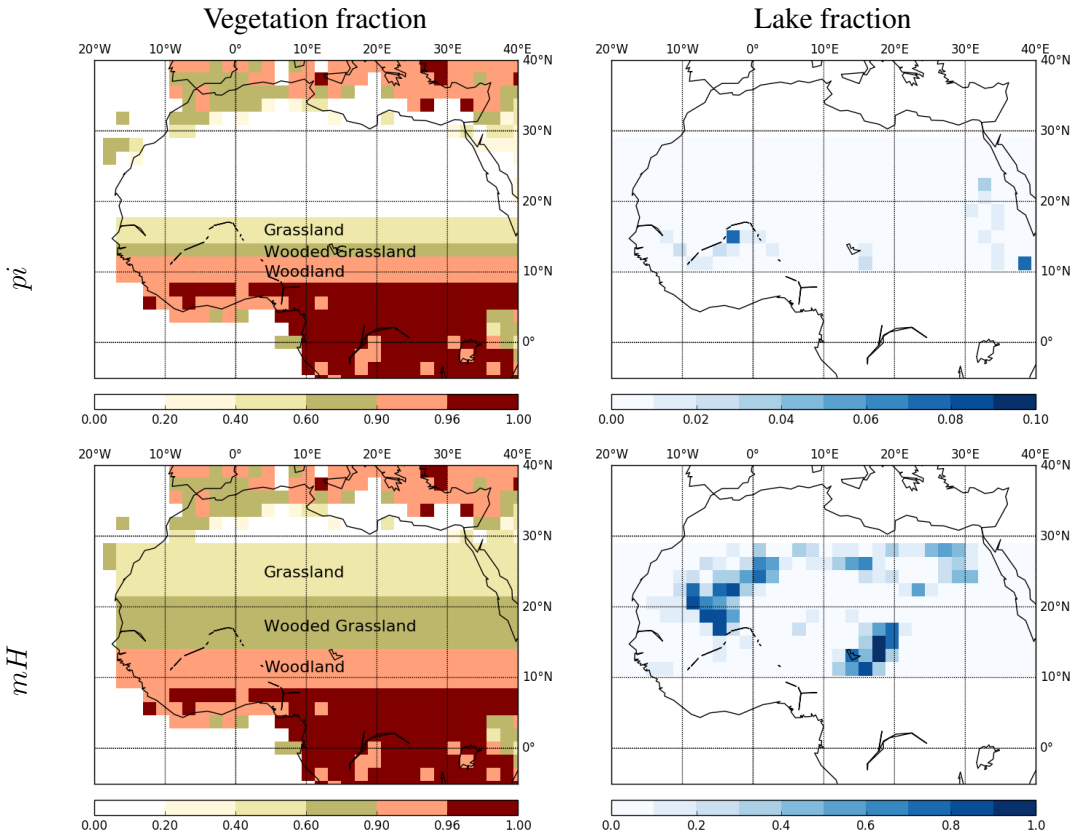

FIGURE 3.1: Prescribed pre-industrial (pi) and mid-Holocene (mh) vegetation distribution following Larrasoaña et al. (2013), pre-industrial lake distribution based on satellite data (Loveland et al., 2000) and a paleolake reconstruction of Tegen et al. (2002). Note that the scale is different for pi and mh lake fraction.

	Woodland	**Wooded grassland**	**Grassland**
Vegetation cover [%]	95	80	58
C4 grass [%]	50	80	100
Tropical evergreen forest [%]	50	20	0

TABLE 3.1: Biome representation as a composition of plant functional types (PFT) in JSBACH (Hagemann, 2002). For desert, the vegetation cover fraction and cover fraction of all PFTs are set to zero.

The linear land cover decline is designed in two different ways:

Scenario 1: The total vegetation cover fraction, the cover fraction of each PFT, soil albedo and maximum soil moisture depth are interpolated linearly between pi and mh land cover in each grid cell in North Africa. Similarly, lake surface fraction is decreased linearly in each grid cell of the North African domain (17°W–40°E; 10°N–30°N).

Scenario 2: Here, we assume a southward retreat of vegetation and lakes in North Africa (17°W–40°E; 10°N–30°N). In each intermediate state, the northern limit of vegetation extent proceeds southward by one grid cell (approximately 1.9°). The latitudinal arrangement of biomes is shifted accordingly (Fig. 3.2). The cover fractions of all PFTs and the total vegetation cover fraction remain for each biome. Thereby, the mean vegetation cover in the North African domain declines approximately linearly. We assume that lakes can not sustain in non-vegetated desert areas and lakes are thus shifted southward in conformity with vegetation cover. In the vegetated area, we scale the paleolake map of Tegen et al. (2002) such that we obtain a linear decline of lake fraction averaged over North Africa.

For all states of both scenarios, pre-industrial orbital parameters and greenhouse gas concentrations are set similar to Chapter 2. Sea surface temperature (SST) and sea ice concentration (SIC) are prescribed to pre-industrial conditions originating from CMIP5 simulations of the MPI Earth System Model (Giorgetta et al., 2013). Hence, changes in atmospheric circulation are only induced by land surface-climate feedbacks. This is a reasonable assumption for our model experiment, because the effect of orbital forcing induced changes on precipitation and atmospheric circulation appears to be minor compared to that of the prescribed land surface conditions (Patricola and Cook, 2007; Egerer et al., 2016). Each simulation is run for 65 years including five years of spin-up.

FIGURE 3.2: Latitudinal extent of biomes for simulations mh, I1-I5 and pi in Scenario 2. The vegetation/desert boundary is highlighted.

3.3 Results

We determine dust emission from North Africa (17°W–40°E; 10°N–30°N) and dust deposition in the grid cells around the marine sediment cores (Table 1.2, Fig. 1.6) for pi, mh, and all intermediate states I1, I2, ... I5 of the two scenarios of prescribed land cover change as described in section 3.2. The decrease of vegetation and lake cover is approximately proportional. Thus, when we express simulated dust emission and dust deposition as a function of mean vegetation fraction, they are at the same time a function of lake surface fraction.

3.3.1 Scenario 1: Homogeneous decrease of vegetation and lake cover

In case of a spatially homogeneous retreat of vegetation and lake cover, the rise in simulated dust emission in North Africa is approximately linear with a slight S-shaped modulation (Fig. 3.3). At the position of the marine cores, the simulated dust deposition changes simultaneously for all site locations (Fig. 3.3) in agreement with McGee et al. (2013a). At a high vegetation fraction (> 0.7), dust deposition fluxes hardly change. Deposition fluxes rise linearly when the vegetation fraction is lower than 0.7. A decline in mean vegetation fraction of 0.1 causes an increase of deposition fluxes of approximately 2.5–4 g/m^2/a for the southern cores, consistent with the marine dust records (Fig 1.7). The total amount of simulated dust deposits at the core sites is much higher than indicated by the marine records, especially during the mid-Holocene (mh) and for the northern cores GC49 and GC37. However, there is no evidence of a sudden change in dust deposition due to a critical threshold of vegetation or lakes on dust emission similar to the abrupt shift seen in marine sediment records (Fig. 1.7).

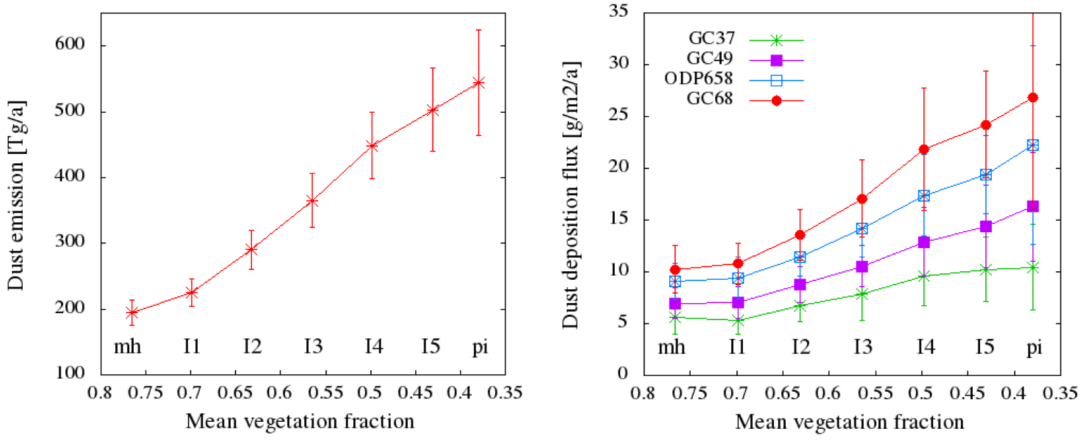

FIGURE 3.3: Simulated dust emission from North Africa (17°W–40°E; 10°N–30°N) (left) and simulated dust deposition flux at the position of the marine cores (right) in case of a homogeneous decrease of vegetation cover and lake surface area.

Accordingly, the precipitation decreases linearly with declining vegetation (Fig. 3.4).

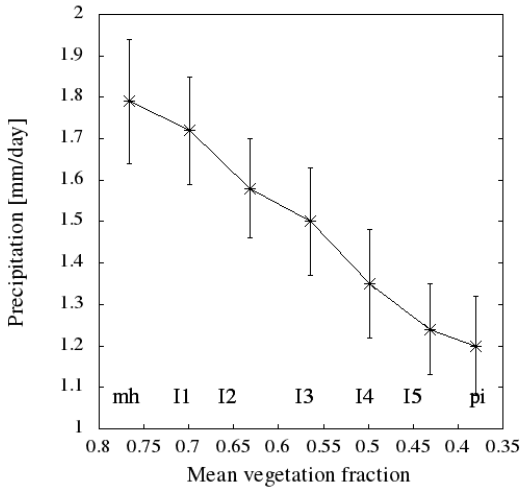

FIGURE 3.4: Simulated precipitation in North Africa (17°W–40°E; 10°N–30°N) in case of a homogeneous decrease of vegetation cover and lake surface area.

3.3.2 Scenario 2: Southward retreat of vegetation and lake cover

Simulated dust emission averaged over North Africa (17°W–40°E; 10°N–30°N) increases approximately linearly with a southward retreat of vegetation and lake cover (Fig. 3.5), i.e. emission fluxes follow the reduction in vegetation and lake covered area. Small deviations at I4, when the vegetation fraction is around 0.5, arise from the prescribed non-uniform stepwise southward retreat of woodland and wooded grassland (see Fig. 3.2).

However, the evolution of dust deposition differs between the core sites (Fig. 3.5). At the position of the most northern site GC37, deposition rises with decreasing vegetation and lake cover, when the maximum northern grassland extent (which is equivalent to the desert boundary) retreats from 28°N to 24°N. There is even a slight decrease in dust deposition, when the desert expands further south than 24°N. At GC49, dust deposition rises as long as the vegetation fraction is higher than 0.5 (when vegetation extends up to 22°N), before it levels off at lower vegetation fractions. At the southern cores (GC68 and ODP658), dust deposition increases slightly at a vegetation fraction above 0.65, strongly increases when the vegetation fraction is between 0.65 and 0.45 and is relatively invariant when the vegetation fraction is below 0.45. The steepest rise in dust deposition is associated with a retreat of the northern grassland boundary and lakes from 26°N to 20°N (Fig. 3.5). In Fig. 3.6, we show the difference in vegetation and lake fraction between I2 and I5, corresponding to a retreat of grassland from 26°N to 20°N, and the obtained emission patterns. We see that especially in northwest Africa, where many lakes were located between these latitudes during the AHP, dust emission at I2 is much lower

compared to I5. When the lakes dry out, the paleolake beds expose fine grained material to deflation by surface winds. Northeasterly Harmattan winds transport the dust to the North Atlantic, especially during spring (Engelstaedter et al., 2006). Consistent with this, we find the highest peak in dust emission during spring in the intermediate simulations (I1,...,I5) of this scenario and a second smaller peak during the summer when dust transport is affected by the West African monsoon (not shown). Additionally, wooded grassland is replaced by grassland between 16°N and 20°N, where increasingly larger gaps in the vegetation cover emerge and enable dust emission. Also in Scenario 2, there is no sudden shift in precipitation in North African (Fig. 3.7). The decrease in precipitation is somewhat lower from mh to I1 and from I5 to pi and somewhat steeper from I4 to I5. But approximately, there is a monotonous decline in precipitation in accordance to the linear decline in vegetation and lake cover.

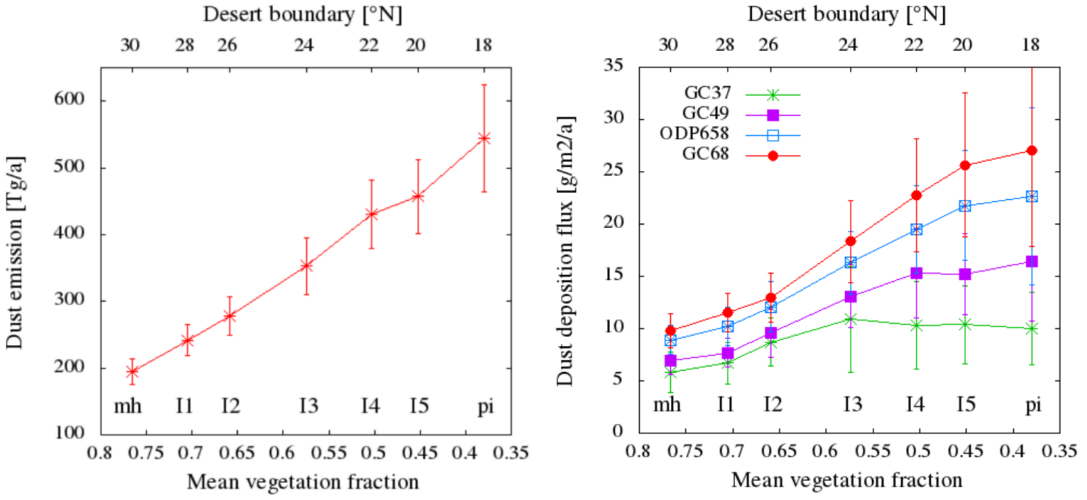

FIGURE 3.5: Simulated dust emission from North Africa (17°W–40°E; 10°N–30°N) (left) and simulated dust deposition flux at the position of the marine cores (right) in case of a southward retreat of vegetation and lakes.

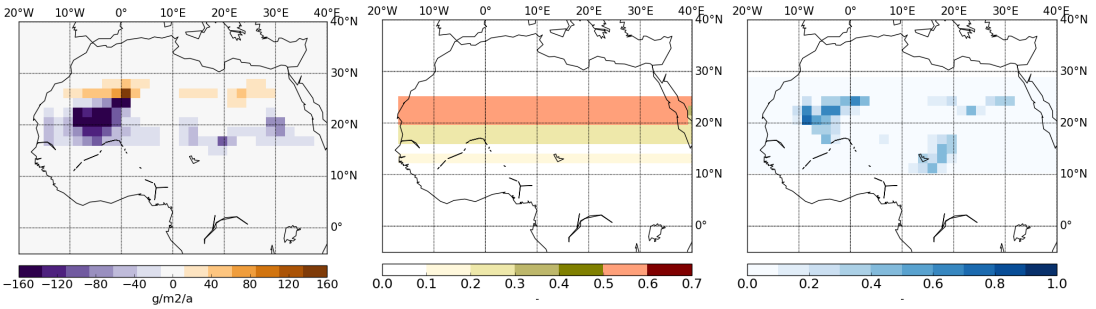

FIGURE 3.6: Difference in simulated (a) dust emission, (b) vegetation fraction and (c) lake fraction between I2 and I5, when the desert boundary retreats from 26°N to 20°N.

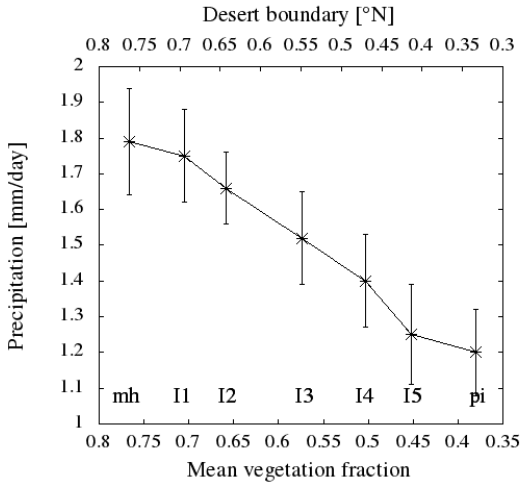

FIGURE 3.7: Simulated precipitation in North Africa (17°W–40°E; 10°N–30°N) in case of a southward retreat of vegetation and lakes.

3.3.3 Changes in surface winds

During the winter (DJF), we see how dust along the northwest African margin is transported by northeasterly trade winds (Fig. 3.8). During the summer (JJA), the ITCZ as the zone of surface wind convergence is shifted northwards. Dust is transported mainly within the Saharan Air Layer at higher altitudes (see Section 1.2).

We find that for prescribed mid-Holocene land surface conditions the northeasterly surface winds slightly enhance along the northwest African coast during winter, whereas during the summer easterly winds are slightly reduced along the coast up to 20°N (Fig. 3.8). However, especially during the summer, changes in surface winds are minor compared to those of the mid-Holocene simulation in Chapter 2. In this previous mid-Holocene simulation, not only changes in land surface conditions, but also changes in orbit and ocean conditions were accounted for. There, we find a northward shift of the ITCZ during the mid-Holocene in the summer months and strongly reduced easterly winds between 15°N and 22°N. We do not find this shift and an associated shift in wind systems in our current simulations.

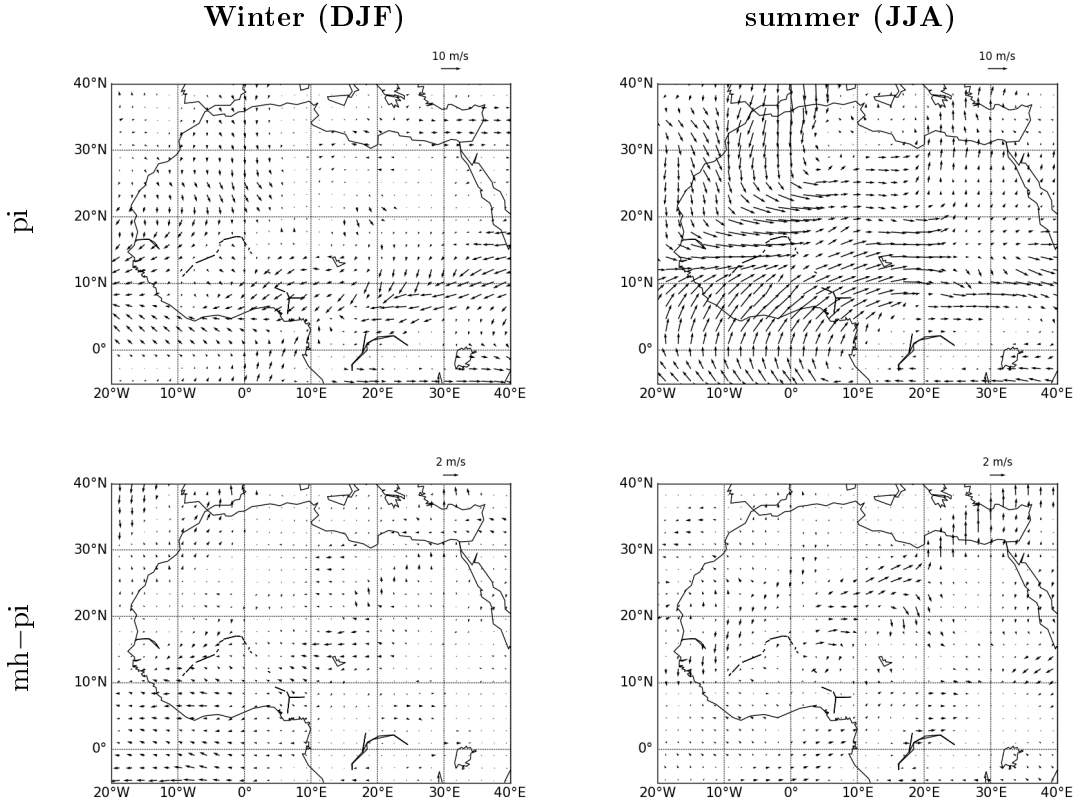

FIGURE 3.8: Simulated 10m wind speed and directions for winter (DJF, left) and summer (JJA, right) for pre-industrial (pi, top) and for the difference between mid-Holocene and pre-industrial (mh−pi, bottom).

3.4 Discussion

In two scenarios, we have explored how the simulated dust flux responds to a prescribed gradual change in vegetation cover and lake surface area from the former 'green Sahara' during the mid-Holocene to today's hyperarid desert. We have compared the simulated dust deposition flux in the North Atlantic to marine sediment records which indicate an abrupt change in dust deposition (deMenocal et al., 2000; Adkins et al., 2006; McGee et al., 2013a; Albani et al., 2015). In the first scenario, vegetation cover and lake surface area are prescribed to decrease gradually and spatially homogeneously in North Africa. We find an approximately linear rise in North African dust emission with decreasing land cover in our simulations. At the position of the North Atlantic cores, the simulated dust deposition first remains low when land cover fractions are high and, later, it increases linearly with decreasing vegetation and lake cover until the desert state is reached. We do neither find evidence of an abrupt change in North African dust emission nor of an abrupt change in dust deposition in the North Atlantic in response to a gradually and homogeneously decreasing vegetation and lake cover.

In the second scenario, vegetation and lakes retreat stepwise southward as suggested by precipitation reconstructions (Lézine et al., 2011; Shanahan et al., 2015). North African dust emission increases approximately linearly in our simulations, proportional to the unvegetated area. The slope of simulated dust deposition in the North Atlantic as a function of prescribed vegetation cover varies between the core sites. The more northern the core, the earlier we find the maximum rise in dust deposition. In contrast, marine sediment records show an abrupt and almost simultaneous change in dust deposition at cores spanning the interval between 19°N and 27°N (McGee et al., 2013a). The maximum rise in dust deposition in the southern cores (GC68, ODP658) is linked to vegetation and lake decline from 26°N to 20°N (Fig. 3.6). Especially in the western Sahara, numerous lakes were located between these latitudes during the mid-Holocene. As the desert boundary retreats southward, former ground covered by lakes turns into a highly productive dust source due to fine grained material in exposed paleolake beds, that is susceptible to wind erosion. However, this somewhat faster change in dust deposition in our simulations is not sufficiently sharp to explain the abrupt marine sediment signal. Hence, we can exclude a sudden exposure of main dust sources by stepwise southward retreating vegetation and lakes to be the exclusive cause for the abrupt shift in dust deposition indicated by the marine records.

In summary, no matter how vegetation and lakes are prescribed to decline gradually, there is no obvious tipping point in North Atlantic dust deposition, but rather an approximately linear rise in deposition with decreasing vegetation and lake fraction. Accordingly, the precipitation in North Africa declines gradually. Because a linear decline of vegetation and lake fraction can not explain the abrupt shift in dust deposition in the marine cores, vegetation and lakes must have retreated rapidly to cause a sudden exposure of bare soil to wind deflation in the area of main dust sources in the northwest Sahara assuming that the model treats the dependence of dust emissions on land surface conditions correctly. This conclusion is consistent with simulation studies of Claussen et al. (1999) and Liu et al. (2006), which show a rapid large scale North African landscape transition around 5.5 ka BP. Liu et al. (2006) argued, that there is a precipitation threshold on vegetation growth, causing a rapid response of vegetation cover to a rather gradually change in precipitation. Alternatively, several feedback mechanisms, potentially amplifying one another, were proposed to cause the emergence of two stable states in the system, i.e. a humid state with enhanced vegetation cover and a dry desert state (Brovkin et al., 1998). An abrupt system shift from one state to another may be triggered by small changes in external forcing. Potential feedback mechanisms include vegetation-precipitation feedbacks (Claussen et al., 1999), vegetation-soil feedbacks (Janssen et al., 2008) or water surface-climate feedbacks (Krinner et al., 2012). The feedbacks might be strengthened by a dust-climate feedback (Pausata et al., 2016).

A synthesis of paleohydrologic data supports a fast north-south retreat of lakes and wetlands at the end of the AHP between 28°N to 19°N with a strong drying out of all water bodies around 4.5 ka BP, and a much more gradual decline between 19°N and 13°N (Lézine et al., 2011). Several studies suggest a more gradual vegetation decline in the southern Sahara: paleohydrologic and -biologic evidence, e.g. from Lake Yoa for non-tropical taxa at 19°N (Kröpelin et al., 2008), Lake Chad (Amaral et al., 2013) and precipitation reconstructions at approximately 15°N (Niedermeyer et al., 2010; Shanahan et al., 2015). The more gradual decline in the southern Sahara and Sahel region is not in contradiction with our results. We find that the northeastern Atlantic is mostly supplied by highly active dust sources in the northwest Sahara (Carlson and Prospero, 1972; Engelstaedter et al., 2006) in accordance with paleo records (Skonieczny et al., 2015). More southern dust sources, including the Bodélé depression as today's most productive dust source worldwide, do not seem to affect dust deposition at the location of the marine cores significantly (Middleton and Goudie, 2001; Cockerton et al., 2014). Our study supports the hypothesis of a rapid large scale transition of landscape in the northern Sahara and does not contradict a more gradual and later landscape change to the south. We argue that spatial differences are to be considered in the debate about the timing and abruptness of Saharan landscape transition during the Holocene.

Spatial differences in the dynamics of dust accumulation are linked to changes in dust sources rather than changes in atmospheric circulation (Cockerton et al., 2014): In contrast to the abrupt change in dust deposition found in North Atlantic sediment cores at around 5.5 ka BP (deMenocal et al., 2000; McGee et al., 2013a), reconstructions from lake sediments show an initially gradual increase in dust accumulation in the Manga Grasslands more south at around 13°N (Cockerton et al., 2014), which only became more rapid after about 1.6 ka BP. Dust transport to the Manga Grasslands is affected by the same wind system as dust transport to the north-eastern Atlantic cores, i.e. the low-level north-easterly trade wind system. Hence, a change in those wind system would affect dust transport to both areas in a similar way and only changes in dust source regions can be responsible for the different timing in dust accumulation.

As pre-industrial orbit and ocean conditions are fixed in our simulations, we do not find a significant shift of the ITCZ and a change in wind systems in the mid-Holocene simulation compared to Chapter 2 with a similar model configuration but mid-Holocene orbit and ocean conditions. However, in Chapter 2, the difference in dust deposition in the North Atlantic is nevertheless quite small between mid-Holocene and pre-industrial orbit and ocean conditions, as long as mid-Holocene land surface is prescribed. Hence, changes in orbit and ocean conditions were assumed to be of minor importance for dust deposition in the North Atlantic.

Further, we have focused on the latitudinal distinction of land surface distribution, whereas we have neglected a differentiation between the eastern and western Sahara. Although several studies suggest an east-west gradient in the termination of the AHP (Liu et al., 2007; Lézine et al., 2011; Shanahan et al., 2015), we argue that longitudinal differences in the vegetation distribution are of minor importance to explain the abrupt increase in dust deposition found in several marine sediment cores because of the dominant West African dust sources. Due to the prescribed vegetation and lakes in our study, feedback mechanisms between climate, vegetation and dust are missing. External forcing accelerated by those feedbacks may help to reduce the gap between results from simulations and paleo reconstructions of North African climate to gain a more comprehensive understanding of Holocene climate change.

3.5 Conclusions

In our simulations, we find that a gradual decline of Saharan landscape during the Holocene results in an almost linear accumulation of North Atlantic dust. We do not find evidence of an abrupt change in dust deposition as indicated by marine sediment records. These results point to a rather fast large scale change of Holocene Saharan landscape, especially in the northwest Sahara, where we find significant dust sources today that were covered by lakes and vegetation during the mid-Holocene. We argue that most likely the landscape transition occurred more rapidly in the northern Sahara and more gradually to the south, from where dust deposition in the North Atlantic cores is barely affected. A spatial and temporal distinction is necessary in the debate whether the transition from the 'green Sahara' to today's desert occurred rather abruptly or gradually.

Chapter 4

Rapid increase in simulated North Atlantic dust deposition due to fast change of northwest African landscape

4.1 Introduction

North Atlantic sediment records show an abrupt increase in dust deposition close to the northwest African margin about 5 ka BP (deMenocal et al., 2000; Adkins et al., 2006; McGee et al., 2013a; Albani et al., 2015), which is also indicated downwind both in a tropical North Atlantic core and at the Bahamas (Williams et al., 2016). The abrupt increase in dust deposition has been attributed to an abrupt Holocene landscape change in North Africa. For instance, modeling studies reveal a sudden large scale decline of North African vegetation cover (Brovkin et al., 1998; Claussen et al., 1999; Liu et al., 2006). Also, paleohydrologic records point to a rapid drying-out of all water bodies at the end of the African Humid period (AHP) about 4.5 ka BP (Lézine et al., 2011). In contrast, pollen records from lake Yoa (Kröpelin et al., 2008), sediment records from the Manga Grasslands (Cockerton et al., 2014) and a modeling study of vegetation cover transition (Renssen et al., 2003) indicate a more gradual change of North African landscape. Paleohydrologic reconstructions show a southward retreat of the tropical rain belt with local differences in the timing and abruptness of the retreat (Shanahan et al., 2015). The origin of the abrupt change in North Atlantic dust deposition in the context of Holocene landscape change in North Africa is thus still a matter of debate.

In Chapter 3, we have tested the hypothesis that a gradual decline of North African vegetation and lake cover results in an abrupt increase in North Atlantic dust deposition due to the nonlinearity in dust activation or due to the heterogeneous distribution of major dust sources. However, we have found no evidence for such an abrupt increase in dust deposition. This suggests that the fast increase in dust deposition has been caused by a fast vegetation decline or by a rapid desiccation of lakes. Fast changes in vegetation cover have been attributed to a precipitation threshold on vegetation (Liu et al., 2006) or they might have been triggered by internal feedbacks between climate and vegetation that amplify the gradual insolation forcing (Brovkin et al., 1998; Claussen et al., 1999). The first one who proposed such a positive vegetation-climate feedback was Charney (1975). According to his theory, the high desert albedo leads to more stable conditions in the air column above compared to its surrounding and thus precipitation is suppressed, which results in a self-stabilization of the desert. Similarly, the mechanism works the opposite way in vegetated areas due to their low albedo. Additionally, increased evapotranspiration due to enhanced vegetation, extended lake surface area and wetter soils promotes enhanced water recycling. Increased precipitation further supports the establishment of vegetation and lakes (Hales et al., 2004). A change in external conditions may trigger an abrupt transition from a humid vegetated to a hyperarid desert state in the presence of these positive feedbacks.

In this chapter, we explore the idea that vegetation-climate feedbacks cause an abrupt change in vegetation cover and associated North Atlantic dust deposition by coupling vegetation, climate and dust dynamically. Therefore, we perform a series of time slice simulations from the mid-Holocene to the pre-industrial era using the global aerosol-climate model ECHAM6-HAM2 (version echam6.3-ham2.3). Ocean conditions for each time slice and a linear decline of lake surface area over time are prescribed. The study is guided by the questions:

1. Do we find an abrupt shift in North Atlantic dust deposition as indicated by sediment records?

2. How was the abrupt shift in North Atlantic dust deposition linked to Saharan landscape transition towards the end of the AHP?

3. What is the role of vegetation-climate feedbacks for the transition of North Atlantic dust deposition?

4. How did the timing and abruptness of the Saharan landscape transition vary spatially?

4.2 Model and experimental setup

4.2.1 Experimental setup

We perform a series of time slice simulations using the global aerosol-climate model ECHAM6-HAM2 (version echam6.3-ham2.3) covering the Holocene from 8 ka BP to the pre-industrial era, 1850 AD, in 2 ka intervals, where, for example, 6k refers to 6 ka BP. The mid-Holocene time slice is hereafter referred to as 6k, the pre-industrial time slice as 0k. We take a pre-industrial control rather than present-day to exclude any anthropogenic impact. Because marine sediment records indicate a rather abrupt change in dust accumulation at about 5.5 ka BP and 4.9 ka BP (deMenocal et al., 2000; McGee et al., 2013a), we add a time slice at 5 ka BP. Vegetation and dust are calculated interactively. To get the dynamical vegetation in equilibrium, we first run 30 years with accelerated vegetation followed by 570 years with non-accelerated vegetation. As an example, the evolution of vegetation cover fraction and changes in cover fractions of grasses, shrubs and trees of the vegetation cover are shown in Fig. 4.1 for the mid-Holocene (6k) time slice. We take the last 200 years for evaluation. We consider a rather long period for evaluation because the dynamic vegetation in JSBACH varies on time-scales of more than 100 years as for example in the grass and shrub fraction.

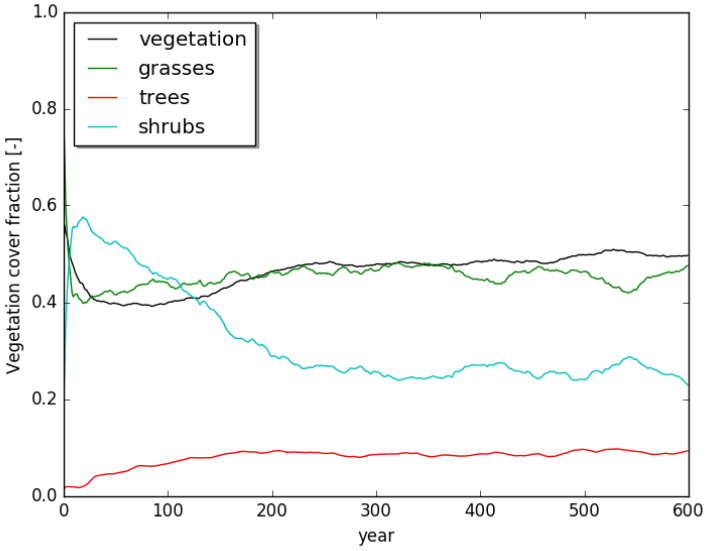

FIGURE 4.1: Temporal evolution of vegetation cover fraction and the cover fractions of grasses, shrubs and trees of the vegetation cover for the mid-Holocene (6k) time slice. The mean of the last 200 years is used for evaluation.

A simple dynamic soil albedo scheme is included in the model for this study, where the soil albedo α_{soil} is parametrized based on plant net primary productivity (NPP):

$$\alpha_{soil} = \alpha_{obs} - (\alpha_{obs} - \alpha_{dark} \cdot \left(\frac{\overline{NPP}}{NPP_{dark}}, 1 \right)), \tag{4.1}$$

where α_{obs} is the standard soil albedo in JSBACH, which is based on present-day observations, α_{dark} is the albedo of darkened soil, which is composed half of tropical summergreen trees and half of rain-green shrubs. α_{dark} is 0.13 in the visible range and 0.22 in the near infra-red range. $\overline{NPP}$ is the 5-years average NPP and NPP_{dark} is the threshold value for NPP to keep the soil dark (Zink, 2014).

Paleohydrologic records show that the maximum of deep lake formation occurred during the early Holocene around 9 ka BP, whereas the maximum extent of water surface was reached only at 6 ka BP and fell thereafter (Lézine et al., 2011). In our study, the lake surface area is set equally for 8 ka BP and 6 ka BP based on a paleolake reconstruction, similar to the mid-Holocene lake mask in Chapter 2 and Chapter 3 (Tegen et al., 2002) (Fig. 2.1). The lake surface area is, thereafter, prescribed to decline linearly in North Africa similar to the first scenario in Chapter 3. Pre-industrial lake surface area is prescribed based on satellite data (Loveland et al., 2000) (Fig. 2.1). Orbital forcing parameters for each time slice are set following Berger (1978). Greenhouse gas concentrations are assumed to have a minor impact and are set similar to Chapter 2 (Fig. 2.2) following the PMIP protocol for the mid-Holocene (Harrison et al., 2001). We prescribe sea surface temperatures (SST) and sea ice concentration (SIC) averaged over 50 years for each time slice to those calculated interactively in a transient Holocene simulation with MPI-ESM1 that does not contain interactive dust (Bader et al., in prep.). In this simulation, the MPI-ESM1 model configuration consists of the atmospheric component ECHAM6 in T63 resolution with 47 vertical layers (Stevens et al., 2013), the ocean component MPI-OM at 1.6° resolution with 40 vertical layers (Jungclaus et al., 2006) and the land surface component JSBACH (Raddatz et al., 2007). A detailed model description and an evaluation of the model performance is given by Giorgetta et al. (2013). The transient Holocene simulation includes orbital and CO_2 forcing and captures the Holocene era from 8 ka BP until present. We use 50-years mean vegetation cover and cover fractions of all 11 PFTs from the model output of the Holocene simulation to initialize the vegetation distribution in North Africa (17°W–40°E; 10°N–30°N) of each time slice in our study. In this chapter, a 5-layer soil scheme is applied to handle soil moisture instead of the simplified bucket scheme used in the previous chapters. In the 5-layer scheme, water can be stored in different layers of the soil. When the soil dries out, water from deeper layers diffuses upward to the surface preventing a sudden stop in surface evaporation. A skin water reservoir (the uppermost 10e-6 cm of the soil) serves

as a measure for the soil wetness. As soon as the skin reservoir is empty, dust emission is possible.

4.2.2 Model validation

Vegetation cover

We compare the vegetation distribution that was simulated in our model including dynamic vegetation with the vegetation reconstructions used in Chapter 2 and 3 (Fig . 4.2). In the pre-industrial (0k) simulation with dynamic vegetation switched on, the vegetation cover distribution is shifted southward by about 2° compared to present-day satellite observations (Hagemann, 2002). The vegetation cover fraction mostly exceeds 80% south of 12°N in agreement with satellite data and the pre-industrial vegetation reconstruction of Larrasoaña et al. (2013), whereas north of 12°N, the vegetation cover fraction is below 40%. In contrast, in the Larrasoaña et al. (2013) reconstruction, grasslands expand up to 18°N (Fig. 4.2). In the mid-Holocene (6k) simulation with dynamic vegetation switched on, the surface is fully covered with vegetation up to 16°N. The reconstructions predict wooded grassland, which is assumed to be similar to the savanna vegetation of Hoelzmann et al. (1998), extending up to 20°N (Chapter 2) and 22°N (Chapter 3), respectively. The dynamically calculated vegetation cover fraction is higher than predicted by the reconstructions up to 16°N. North of 16°N, the simulated vegetation cover diminishes rapidly. North of 20°N, only some areas in the western Sahara exceed a vegetation fraction of 20%, whereas grasslands persist in the reconstructions and cover around 56% of the surface.

While the pre-industrial vegetation distribution is simulated fairly well with the vegetation cover shifted southward by about 2° compared to satellite data, the mid-Holocene northward extent of vegetation is clearly underestimated, only reaching up to 20°N compared to 30°N predicted by reconstructions. Limitations in the model, which are related to the dynamic vegetation and the soil albedo scheme, cause this large discrepancy and are discussed in Section 5.2. Nevertheless, overall, the mid-Holocene vegetation is shifted significantly northward by about 6° compared to the pre-industrial vegetation. In contrast to the PMIP 1 and 2 setup (Harrison et al., 2001; Braconnot et al., 2007), where pre-industrial vegetation is prescribed for the mid-Holocene, this is a large effort. Still, most climate models fail to reproduce the mid-Holocene northward extent of vegetation possibly due to missing climate feedbacks (Hargreaves et al., 2013).

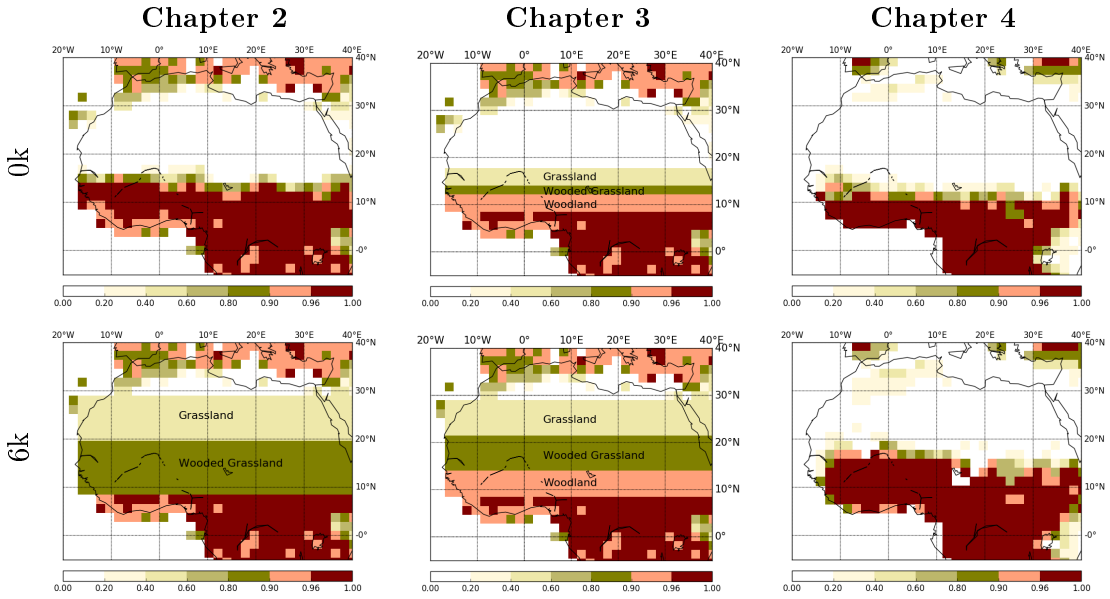

FIGURE 4.2: Reconstruction of vegetation cover adapted from satellite data and Hoelzmann et al. (1998) (Chapter 2), adapted from Larrasoaña et al. (2013) (Chapter 3) and dynamic vegetation (Chapter 4) for 0k (top) and 6k (bottom).

West African monsoon

It is known that ECHAM6 has a dry bias in the Sahel region during the summer for present-day climate and the WAM does not extend sufficiently far north (Eichhorn and Bader, 2016), which results in an overestimation of dust emission.

The simulated precipitation changes between mid-Holocene and pre-industrial in our study clearly exceed those of the precipitation records between 10°N and 15°N by about 800mm/yr and precipitation changes in other modeling studies by about 1000mm/yr (Perez-Sanz et al., 2014) (Fig. 4.3). Only one study with prescribed extensive vegetation and reduced dust predicts higher precipitation changes compared to our study (Pausata et al., 2016). Between 15°N and 20°N, the simulated precipitation changes are slightly lower than those of observations and Pausata et al. (2016) and slightly higher than predicted by all other CMIP5 models. Still, they lie within the uncertainty range of the observations. North of 20°N, the simulated precipitation changes are far below the reconstructed precipitation changes. The overestimation of vegetation between 10°N and 15°N during the mid-Holocene and the lack of vegetation north of 20°N is consistent with an underestimation of the simulated northward extent of the West African monsoon during the mid-Holocene compared to paleorecords (Bartlein, 2011; Perez-Sanz et al., 2014) (Fig. 4.3). Rather than an underestimation of absolute mid-Holocene precipitation changes as in the CMIP5 models, we find a mismatch in the meridional gradient of precipitation changes between our simulations and the reconstructions of Bartlein (2011).

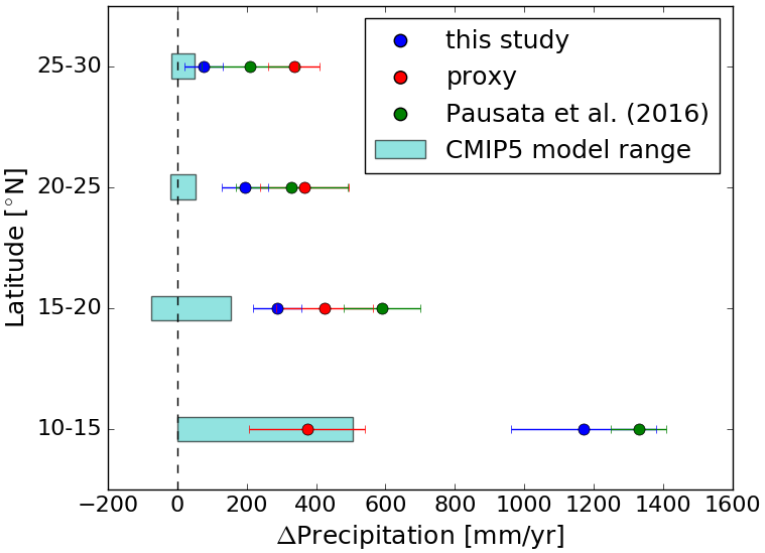

FIGURE 4.3: Comparison of reconstructed and simulated precipitation changes between the mid-Holocene and the pre-industrial era. The simulated zonal mean (17°W–40°E) anomalies between mid-Holocene and pre-industrial precipitation from this study are averaged at the location of grid cells with reconstructions over 5° latitudinal bands between 10°N and 30°N. Proxy data are precipitation reconstructions from Bartlein (2011). Further, the CMIP5 model range (Harrison et al., 2015) and model output from Pausata et al. (2016) are averages for the grid cells with reconstructions. Temporal standard deviations are given for our study and for Pausata et al. (2016) and spatial variation is indicated for the proxy data.

4.3 Results

4.3.1 Do we find an abrupt shift in simulated North Atlantic dust deposition?

We find a rapid increase in simulated dust deposition synchronous for several core sites along the northwest African margin (Fig. 4.4), which is in agreement with marine sediment records (deMenocal et al., 2000; Adkins et al., 2006; McGee et al., 2013a; Albani et al., 2015). In contrast to the marine records, where the most prominent increase in dust deposition occurs at around 5.5 to 4.9 ka BP, we find the sharpest rise in simulated dust deposition along the northwest African margin between 5 and 4 ka BP. Additionally, a significant change occurs between 6 and 5 ka BP in our simulations and, at least at the grid cells around GC68 and ODP658, there is a moderate change between 4 and 2 ka BP. After 2 ka BP, dust depositions remain constant until pre-industrial times, except for GC68, where they even decrease slightly. In the remote sediment cores VM20-234 in the tropical North Atlantic (TNA) and 103GGC at the Bahamas (Williams et al., 2016), the simulated dust deposition increases gradually between 6 and 2 ka BP. From 2 ka BP until pre-industrial, depositions increase further in VM20-234 and remain constant in 103GGC. At all core sites, the simulated dust deposition fluxes remain nearly constant between 8 ka BP and 6 ka BP, which is consistent with the sediment records. A short introduction and the location of the marine cores is presented in Section 1.4.

The simulated deposition fluxes at the core sites along the northwest African margin increase by factors between 2.5 and 3.1 from about 4–5.5 $g/m^2/a$ at 8 ka BP to 10–18 $g/m^2/a$ at 0 ka BP (Fig. 4.4). These ratios are in agreement with both, those indicated by sediment records and those determined in Chapter 2. However, the absolute amount of deposition agrees at GC68 but is slightly higher at the more northern cores in the current study compared to Chapter 2. Compared to the sediment records, the amount of simulated dust deposition agrees well at the more southern sites ODP658 and GC68 but is significantly larger at the northern sites GC49 and GC37 (Fig. 4.4). In the remote sediment cores VM20-234 and 103GGC (Williams et al., 2016), the simulated deposition fluxes agree well with marine records for the mid-Holocene, but are higher by a factor of two for 103GGC and by a factor of three for VM20-234 in the pre-industrial simulations.

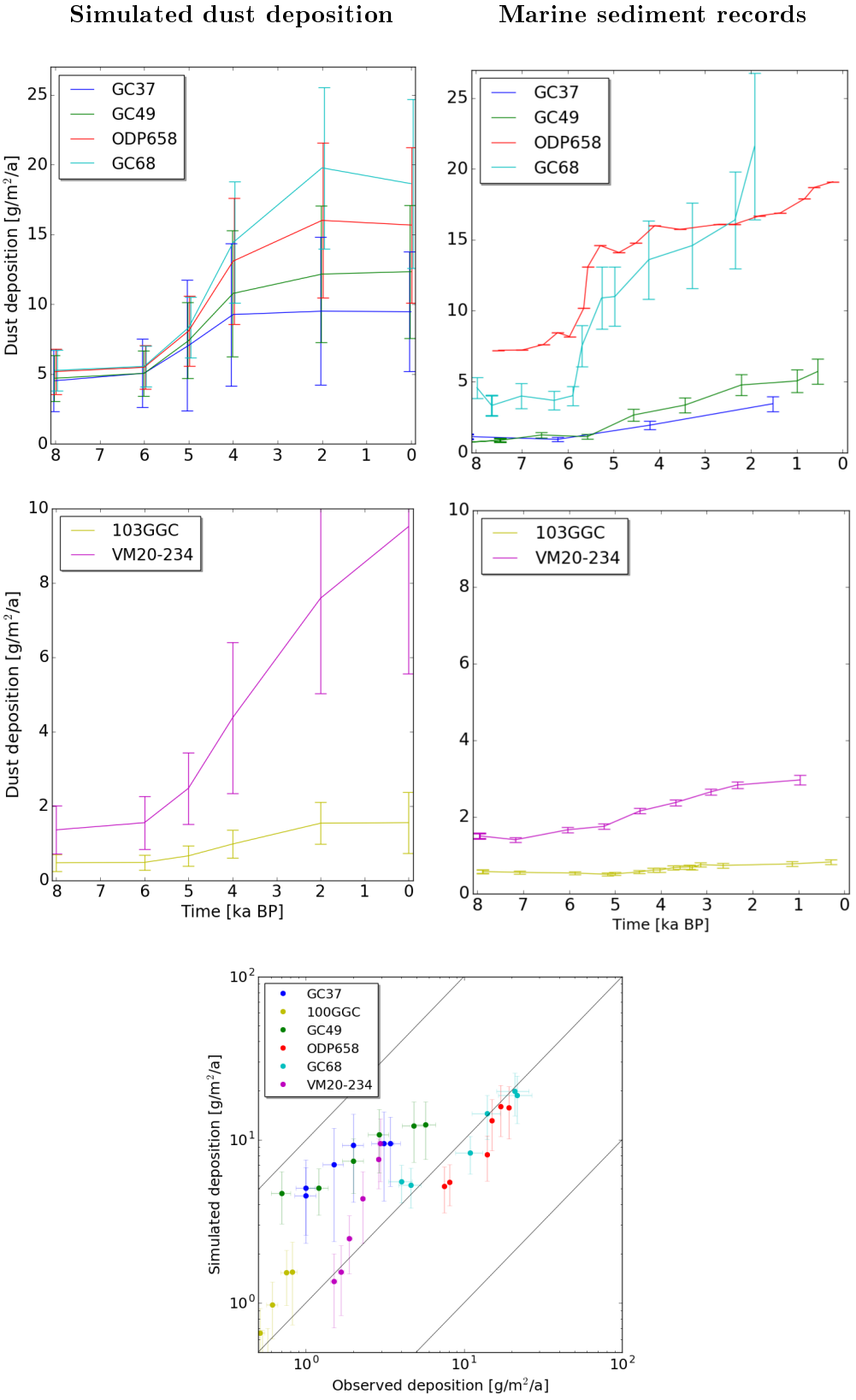

FIGURE 4.4: Simulated dust deposition at the position of the marine cores (top left), dust deposition indicated by marine sediment records (Adkins et al., 2006; McGee et al., 2013b; Williams et al., 2016) (top right) from 8k to 0k and a comparison of simulated and observed dust deposition (bottom).

4.3.2 How is the abrupt shift in North Atlantic dust deposition spatially and temporally linked to Saharan landscape transition?

Satellite observations show that today, the main dust plume is located north of 15°N (Prospero et al., 2002; Engelstaedter et al., 2006) originating from major western Saharan dust sources in Mauritania, Mali and southern Algeria as well as from the Bodélé Depression in the eastern Sahara (Fig. 1.1) (Middleton and Goudie, 2001; Prospero et al., 2002; Engelstaedter et al., 2006). These regions are clearly visible in our simulated dust emission patterns (Fig. 4.5). We assume that dust deposition at the marine cores, which are located north of 19°N, is primarily affected by dust sources north of 18°N due to the northeasterly direction of the near surface winds. To better understand the spatial relation between North African dust sources and North Atlantic dust deposition, we thus consider two domains in North Africa: The northwest Sahara (15°W–10°E; 18°N–30°N, hereafter referred to as NW) and the northeast Sahara (10°E–35°E; 18°N–30°N, hereafter referred to as NE) (Fig. 4.5). We analyze differences in dust emission, vegetation and lake cover from both domains and latitudinal changes between 10°N and 30°N.

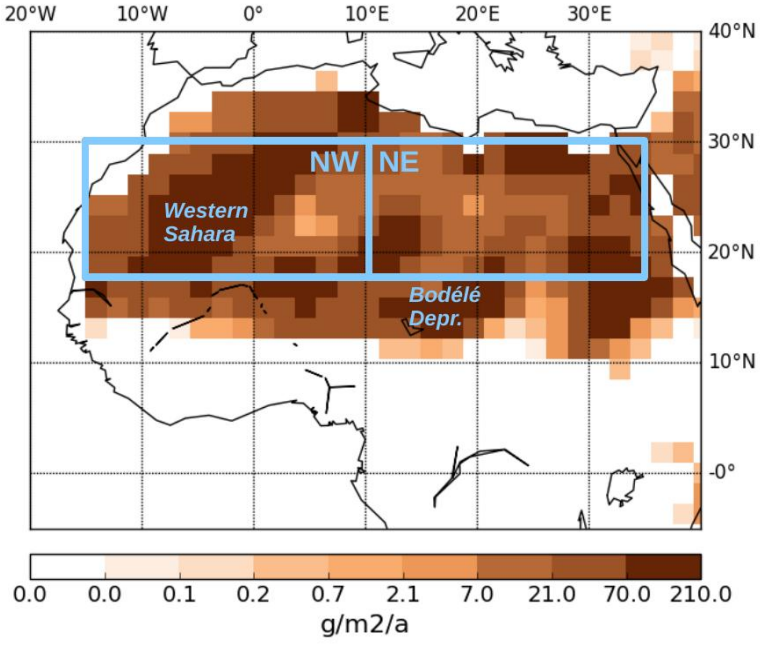

FIGURE 4.5: Simulated dust emission from the northwest Sahara (15°W–10°E; 18°N–30°N, NW) and the northeast Sahara (10°E–35°E; 18°N–30°N, NE). Both domains are marked with a blue frame. Parts of the western Sahara and the Bodélé Depression are major dust sources today.

Zonal differences in Holocene Saharan dust emission and landscape evolution

Simulated dust emission from the NW remains constant between 8 and 6 ka BP, rises strongest between 6 and 4 ka BP, thereafter increases less strong until it remains constant between 2 and 0 ka BP (Fig. 4.6). The evolution of simulated dust emission in the NW during the Holocene is similar to the one of simulated dust deposition at the grid cells around the southern cores GC68 and ODP658 with a strong and rapid change between 6 and 4 ka BP (Fig. 4.4). This points to a strong coupling of northwest African dust sources and dust deposition at the location of the southern dust cores at around 20°N. Hence, the direction of the surface winds must have been quite stable throughout the Holocene. The evolution of dust emission in the NE is, however, different: Simulated dust emission is nearly twice as large during the mid-Holocene in the NE compared to the NW but it increases only slightly thereafter, with a somewhat sharper rise between 6 and 5 ka BP (Fig. 4.6). The absolute increase in dust emission during the Holocene is about five times as high in the NW compared to the NE.

The area covered by vegetation is approximately twice as large in the NW compared to the NE during the mid-Holocene resulting in lower dust emissions (Fig. 4.6). In both areas, the vegetation cover fraction decreases rather gradually from 8 to 2 ka BP, with a somewhat stronger reduction rate between 6 and 4 ka BP, before it remains constant between 2 and 0 ka BP in the NE and even increases somewhat in the NW. Although the pre-industrial vegetation cover fraction is higher in the NW compared to the NE, dust emissions are higher in the NW due to the very effective northwest African dust sources (Middleton and Goudie, 2001; Engelstaedter et al., 2006).

Interestingly, the change in dust emission and dust deposition in the North Atlantic is not only determined by changes in vegetation cover fraction but also changes in the composition of vegetation cover types are important (Fig. 4.6). Shrubs are the dominant vegetation type during the mid-Holocene in the NW. There is a sharp fall in shrub fraction between 6 and 4 ka BP in accordance with the abrupt increase in dust emission and North Atlantic dust deposition. Also, the tree fraction reduces strongest during that period, whereas grasses increase slightly from 6 to 4 ka BP and decrease thereafter to the same level as before. In the NE, all plant types decrease nearly gradually. Only the shrub fraction falls somewhat sharper between 6 and 5 ka BP. Shrubs and trees are much more pronounced in the NW during the mid-Holocene, whereas grasses are predominant in the NE. Nowadays, grasses are the dominant type of vegetation in North Africa in our simulation.

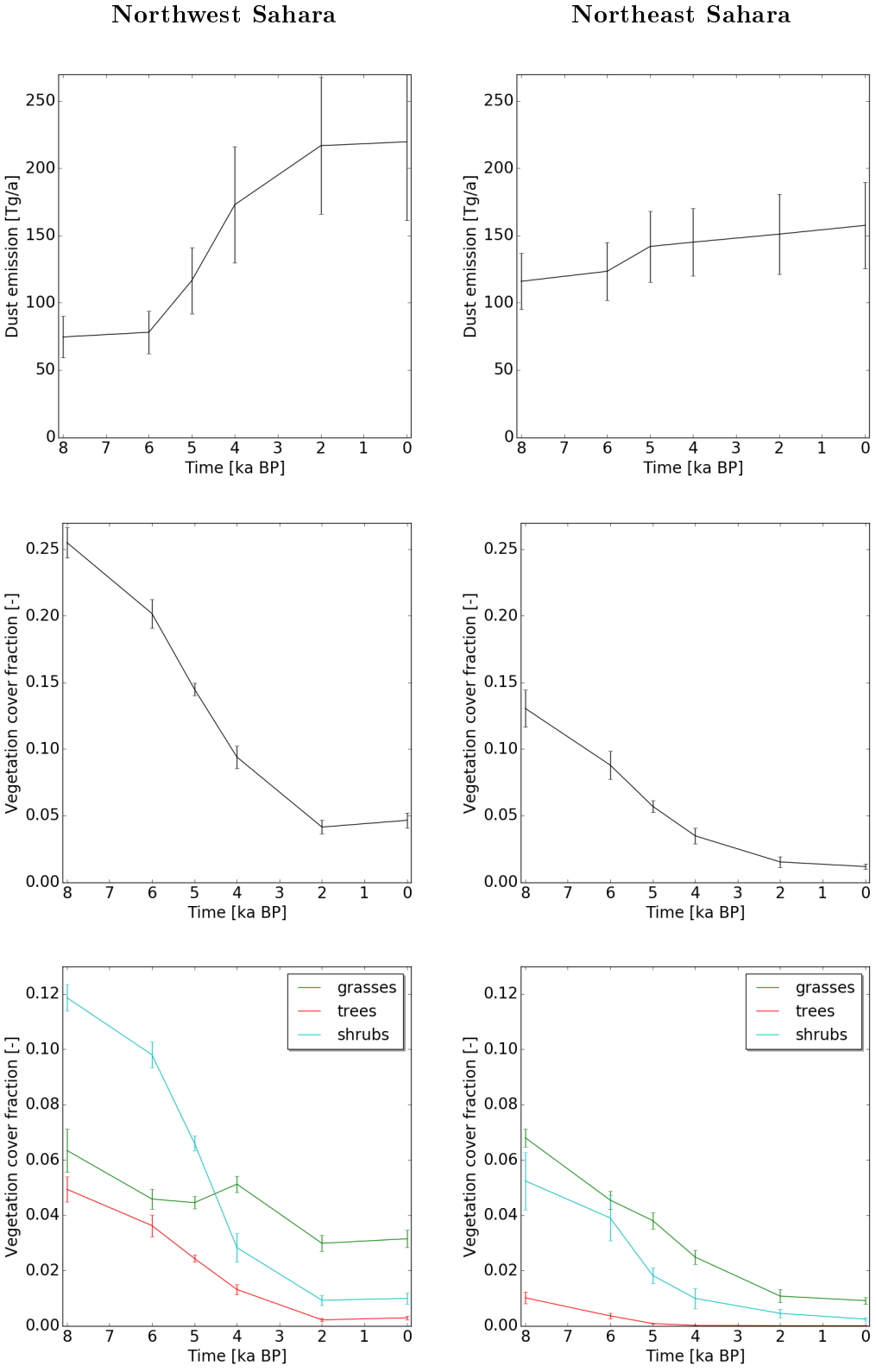

FIGURE 4.6: Simulated dust emission (top), vegetation cover fraction (middle) and cover fractions of grasses, trees and shrubs (bottom) in the northwest Sahara (17°W–10°E; 18°N–30°N, left) and in the northeast Sahara (10°E–35°E; 18°N–30°N, right).

Both domains, the NW and NE, extend over several 1000 square kilometers. Do we find a homogeneous evolution of dust emission in each domain or do subareas with a different evolution of dust emission exist? To locate dust emission sources more specifically, we divide the study domain in areas of 2x2 grid cells, roughly 400x400 km (Fig. 4.8 and 4.9). As an example, we show the area B2 with axes labels in Fig. 4.7. Indeed, south of 18°N (row D,E), dust emission does not increase significantly until 4 ka BP, which justifies the choice of our study domains NW and NE. The steepest rise in dust emission occurs in the areas A5, B2-B4, C2 and C3. These areas include dried-out paleolake basins with fine grained sediments, which can be easily exposed by near surface winds. Accordingly, we see a strong but gradual fall in lake levels in areas A5, B2-B5, C2-4 and D3. A strong shift in vegetation cover is restricted to areas in row C and D. North of that, vegetation cover remains low throughout the Holocene. South of that, the vegetation fraction remains high until present and inhibits dust emission nearly completely. In row C, the rapid reduction of vegetation cover between 6 and 4 ka BP is clearly linked to a sudden rise in dust emission and associated dust deposition at the southern cores GC68 and ODP 658 at around 20°N. In row D, the decrease of vegetation cover is even stronger and occurs later, from around 5 to 2 ka BP. Here, the vegetation density is too high to enable dust emission until 4 ka BP. The rapid decline of vegetation cover in row C and D is tightly coupled with a rapid decrease of precipitation, which points to strong local vegetation-precipitation feedbacks. Also, in areas B2-B4, the reduction of precipitation occurs fast between 6 and 4 ka BP and results partly from the strong lake surface reduction and partly from the moderate vegetation decline.

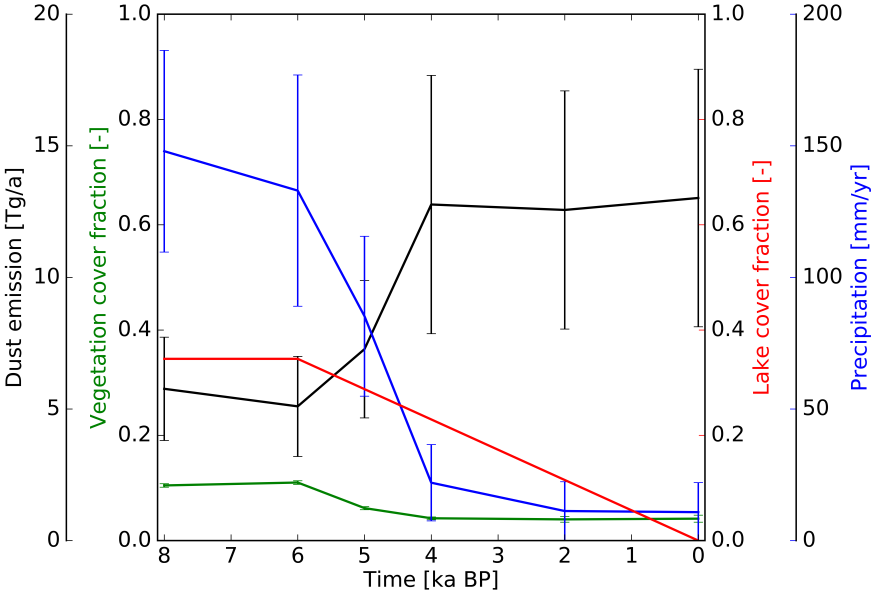

FIGURE 4.7: Simulated dust emission, vegetation cover fraction, lake cover fraction and precipitation in area B2 (approximately 21°W–25°E; 22°N–26°N) of Fig. 4.8 and 4.9. Axes labels and colors are exemplary for all areas in Fig. 4.8 and 4.9.

In conclusion, the strong reduction of lake surface area in NW between 18°N and 26°N and the rapid decline of vegetation cover mainly around 20°N in NW due to local vegetation-precipitation feedbacks cause a sudden increase in dust emission from northwest African dust sources.

In the eastern Sahara, dust emission remains nearly constant or only increases slightly in most of the grid cells. Only in the very east, close to the Arabian Peninsula, there is a stronger increase in dust emission in areas C13, D13 and D14.

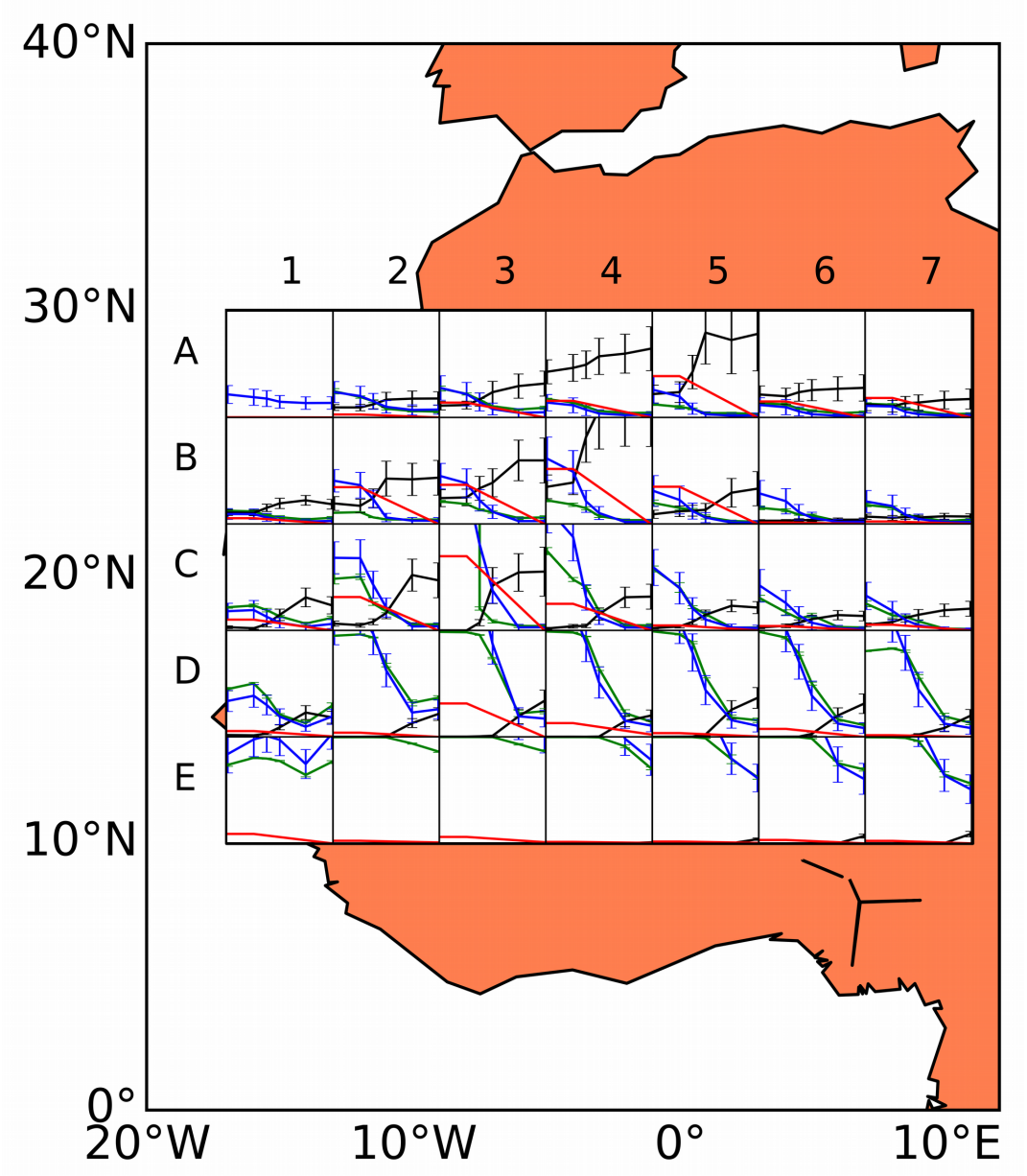

FIGURE 4.8: Dust emission, vegetation cover fraction, lake cover fraction and precipitation out of 4 grid cells in the western Sahara (17°W–11°E; 10°N–30°N).

In area D9 and D10, dust emission rises gradually from 5 ka BP onwards to extremely high values. This area contains the Bodélé Depression, the worlds largest dust source today (Prospero et al., 2002). However, from there, dust is transported in direction of the West African Sahel and supply to the marine cores north of 19°N is minor (Cockerton et al., 2014; Skonieczny et al., 2015). The high water levels during the mid-Holocene in areas D9, D10, E8 an E9 point to the location of former lake Megachad (Armitage et al., 2015).

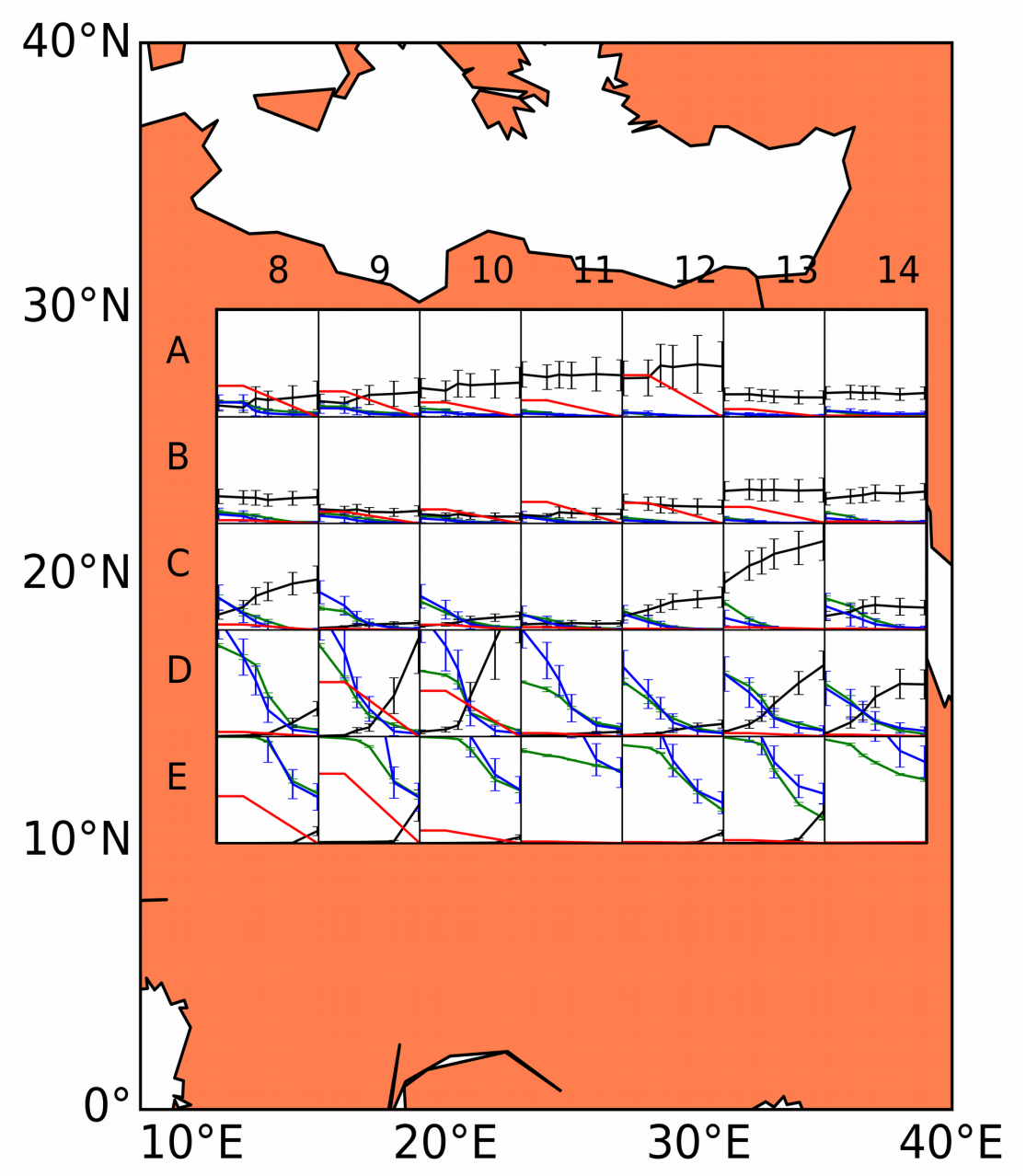

FIGURE 4.9: Dust emission, vegetation cover fraction, lake cover fraction and precipitation out of 4 grid cells in the eastern Sahara (11°E–39°E; 10°N–30°N).

Latitudinal differences in Holocene Saharan dust emission and landscape evolution

We find a southward shift of simulated dust emission, the vegetation cover and precipitation from 8 to 0 ka BP (Fig. 4.10) in agreement with a compilation of precipitation reconstructions in North Africa (Shanahan et al., 2015). Simulated dust emission increases strongly from 6 to 4 ka BP between 20°N and 30°N in the western Sahara and between 16°N and 30°N in the eastern Sahara (Fig. 4.11). The further south, the later the maximum rise in dust emission occurs. From 4 to 2 ka BP, maximum changes in simulated dust emission occur between 14°N and 20°N, from 2 to 0 ka BP, the maximum changes are simulated between 12°N and 16°N (Fig. 4.10) The slope of the rise is maximal at grid cells which contain former paleolakes in the NW and at the position of former lake Megachad (Fig. 4.11, right; compare to Fig. 3.1).

There are vegetation cover changes up to 30°N between 6 and 4 ka BP, up to 26°N between 4 and 2 ka BP and up to 18°N between 2 and 0 ka BP (Fig. 4.10). The strongest changes in vegetation cover occur, however, south of 20°N, between 14°N and 20°N from 6 to 4 ka BP and between 12°N and 16°N from 4 to 2 ka BP. This is because even during the mid-Holocene, our simulated vegetation cover extent north of 20°N is low (Fig. 4.11). North of 16°N, vegetation cover declines mainly between 6 and 4 ka BP, whereas further to the south, the main decrease occurs between 4 and 2 ka BP.

The southward shift of vegetation is linked to a retreat of the West African monsoon: Especially up to 20°N, precipitation declines rapidly from 6 to 2 ka BP. The similar patterns of the latitudinal and temporal transition of vegetation and precipitation point to strong vegetation-precipitation feedbacks. North of 18°N, the reduction in precipitation is maximal between 6 and 5 ka BP in the western Sahara and between 8 and 6 ka BP in the eastern Sahara (Fig. 4.11). South of that, the reduction is strongest between 5 and 4 ka BP and between 4 and 2 ka BP in some areas in the western Sahel. The strong reduction of precipitation between 10°N and 18°N marks the retreat of the West African monsoon. Additionally, the precipitation reduction is maximal at the position of former paleolakes because the more the lakes dry out, the less water can be recycled above the lake surface. The prescribed lake fraction remains at its maximum level between 8 and 6 ka BP and declines linearly from 6 to 0 ka BP (Fig. 4.10). In reality, one might expect that the retreat of lakes is more in accordance with vegetation and precipitation changes due to feedbacks between precipitation and surface waters (Coe and Bonan, 1997; Krinner et al., 2012). However, precipitation and vegetation do most likely not extend sufficiently far north. Also, sub-terrain aquifers may sustain lakes even in dry areas with almost no precipitation and increase the resilience of water bodies at

the end of the AHP (Lézine et al., 2011), which may justify the existence of lakes further north.

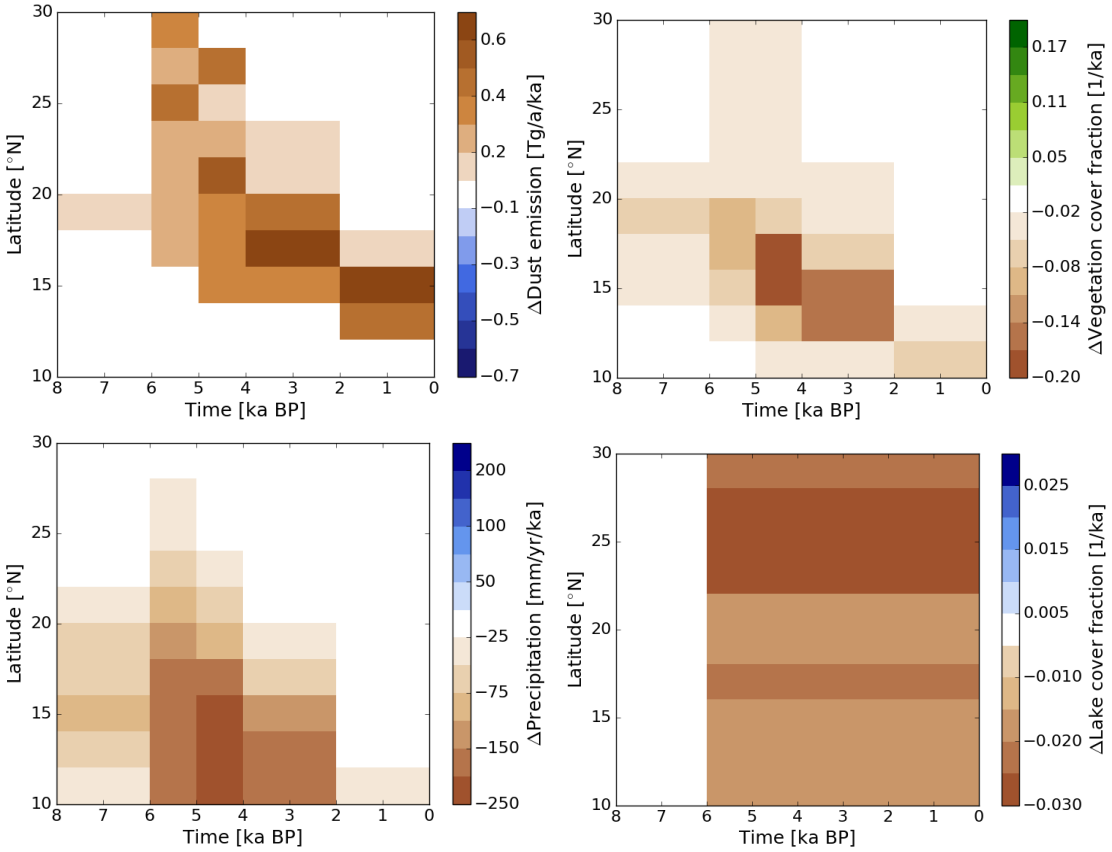

FIGURE 4.10: Zonally averaged (17°W–40°E) differences between two consecutive time slices for dust emission, vegetation cover fraction, precipitation and prescribed lake cover fraction.

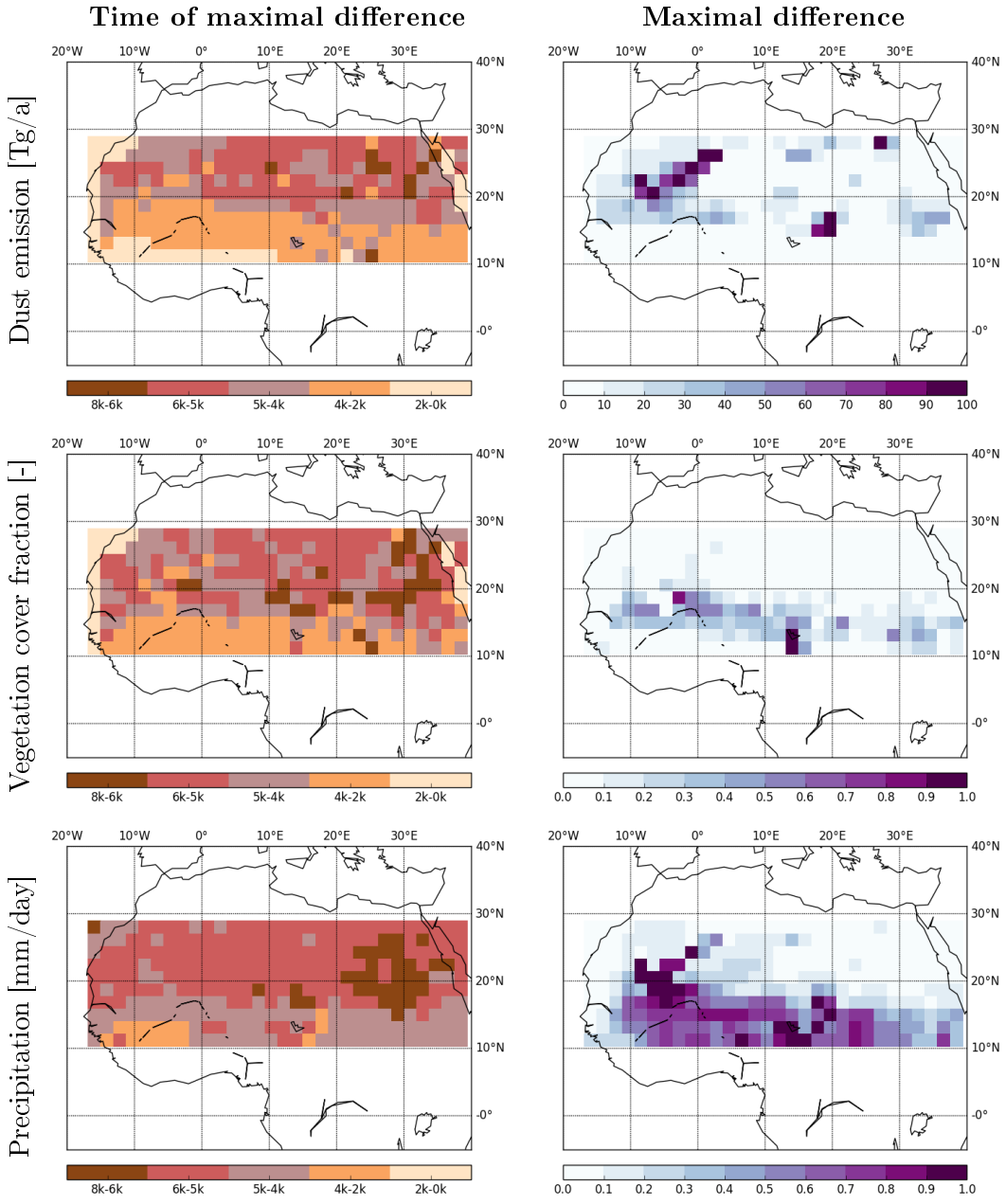

FIGURE 4.11: Time of maximal differences (left) and absolute maximal differences (right) in dust emission, vegetation cover fraction and precipitation. Units apply only to the maximal differences.

4.3.3 Changes in atmospheric circulation and annual cycle of dust emission

During the pre-industrial winter months (DJF), northeasterly surface trade winds between 12°N and 30°N transport dust from the western Sahara in lower altitudes to the North Atlantic (Fig. 4.12). Accordingly, pre-industrial dust emission is strongest in winter and early spring (Fig. 4.13). During the summer (JJA), the ITCZ is shifted northwards. Southwesterly winds transport moist air from the Equatorial Atlantic to the continent in accordance with a northward propagation of the WAM. Dust is transported within the Saharan Air Layer (SAL), which is connected to the African Easterly Jet (AEJ), in higher altitudes up to 500 hPa (Fig. 4.14) westward to the ocean. Consistently, we find a second smaller peak in North African dust emission in June and July (Fig. 4.13). A more detailed description of dust sources and transport in North Africa is given in Section 1.2.

Whereas in the 70s, Sarnthein (1978) argued that the position of the dust belt and the wind systems remained stable throughout the Holocene, later studies (Irizarry-Ortiz et al., 2003; Patricola and Cook, 2007) found a northward shift of the ITCZ during mid-Holocene summer by several degrees. Accordingly, the dust belt, the AEJ and associated wind systems were shifted north and Patricola and Cook (2007) even found a breakdown of the AEJ in their simulations. In our simulations, we confirm the northward shift of the center of the dust belt and the AEJ by approximately 4° from 13°N to 17°N. In the 6k simulation, the dust belt is narrowed by several degrees and much weaker, both, at the surface and at higher altitudes (Fig. 4.14). Its extent at the surface is shifted from between 15°N and 27°N at 0k to between 20°N and 29°N at 6k. The center of the AEJ is located between 10°N to 15°N during 0k and between 15°N to 20°N during 6k. The simulations indicate a clear relation between the shift of the dust belt and the jet system. In accordance with the strongest reduction in atmospheric dust (Fig. 4.14, bottom), near surface winds were weaker between 12°N and 18°N during mid-Holocene summer (Fig. 4.12). However, the changes in wind speed are weak, only reaching up to 2 m/s. During mid-Holocene winter, northeasterly near surface winds are reduced in northwestern Africa by less than 1 m/s. Consistently, dust emission is much weaker in winter and early spring during the mid-Holocene. Peak emissions are shifted by one month from between February and April at 0k to between March and May at 0k (Fig. 4.13). It is remarkable, that early spring dust emissions are reduced much more than dust emissions during the summer in the mid-Holocene simulation.

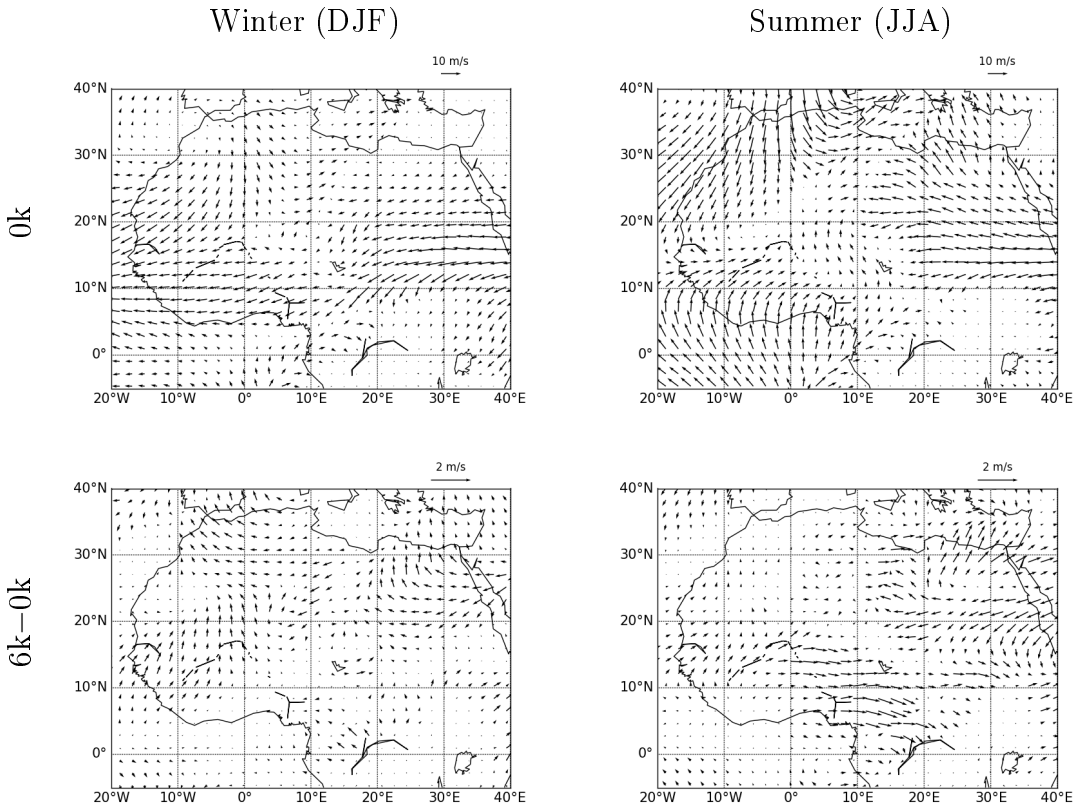

FIGURE 4.12: Simulated 10m wind speed and directions for winter (DJF, left) and summer (JJA, right) for 0k and for the difference between 6k and 0k.

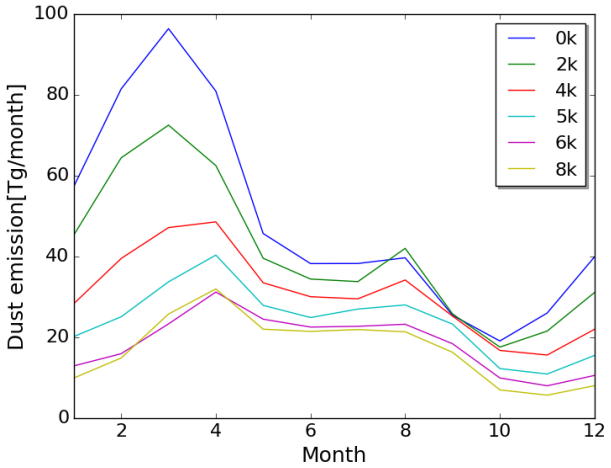

FIGURE 4.13: Mean annual cycle of simulated dust emission in North Africa (17°W–40°E; 10°N–30°N) for all time slices.

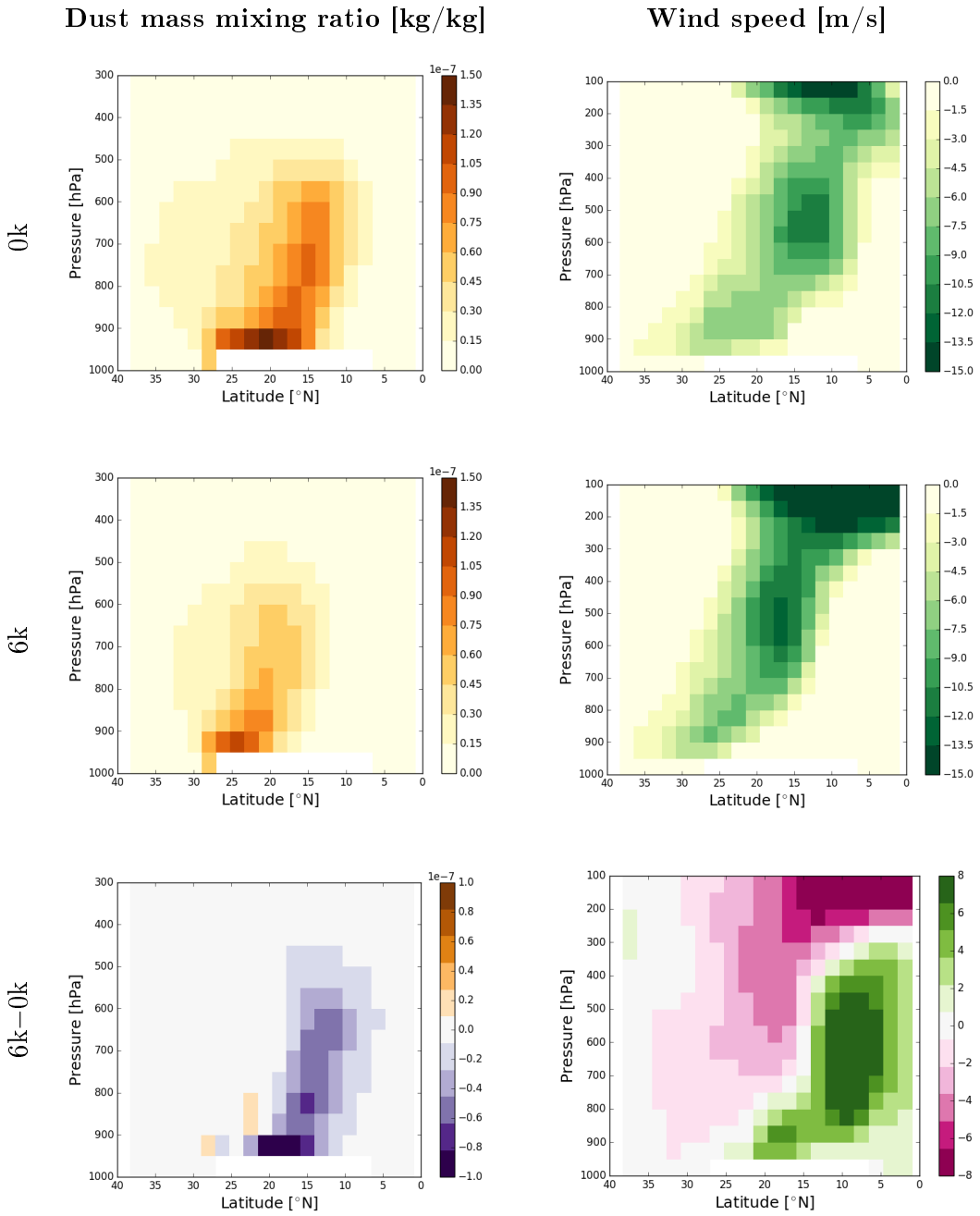

FIGURE 4.14: Zonally averaged dust mass mixing ratio (left) and wind speed (right) between 10°W and 25°E during summer (JJA) for 0k, 6k and 6k-0k. The SAL extends from 22°N to 12°N at 600−800hPa altitude for 0k and from 23°N to 16°N at 650−800hPa altitude for 6k. The core position of the AEJ is at 13°N and 540hPa for 0k and at 17°N and 510hPa for 6k.

4.4 Discussion

As seen in North Atlantic sediment records, we have found a rapid increase in simulated dust deposition at the location of the marine cores along the northwest African margin, which is synchronous over several latitudes from 19°N to 27°N. The sharpest rise in simulated dust deposition occurs between 5 and 4 ka BP, fairly consistent with the sediment records that determine the abrupt change at about 5.5 ka BP (deMenocal et al., 2000) and 4.9 ka BP (McGee et al., 2013a). The simulated dust deposition agrees quantitatively well with the data for GC68 and ODP658 at around 20°N (Adkins et al., 2006; McGee et al., 2013a), but is much higher in our simulations at the more northern cores GC37 and GC49 throughout the Holocene. At the remote cores VM20-234 in the tropical North Atlantic and CCG103 close to the Bahamas (Williams et al., 2016), simulated dust deposition fluxes agree for the mid-Holocene with the sediment records but are higher in the pre-industrial simulation.

The discrepancy between simulated dust deposition and data at the more northern cores may result from an overestimation of dust emission in our simulations. During the pre-industrial era, northwest Saharan dust sources are prescribed as preferential dust sources in the model, which is implemented such that the threshold wind velocity to enable dust emission is reduced. In contrast, these areas are not identified as major dust sources by satellite observations (Schepanski et al., 2012). During the mid-Holocene, the simulated vegetation does not propagate sufficiently far north compared to pollen records (Fig. 4.2) and too much dust is emitted from the uncovered soil. Consistently, ECHAM6-HAM2 is not capable to properly simulate the northward extent of the West African monsoon as indicated by paleo data (Bartlein, 2011). Nevertheless, compared to most other CMIP5 models, the mid-Holocene precipitation bias between our simulations and the observations was reduced (Fig. 4.3). Still, the meridional distribution of precipitation changes is not consistent with observations and requires further attention. The overestimation of long-range transported dust in the pre-industrial simulation compared to the remote records in the North Atlantic (Williams et al., 2016) could result on the one hand from too little simulated vegetation in the northern Sahara compared to satellite data (Fig. 4.2). On the other hand, fine grained particles that are more favorable for long-range transport are dominant in the model. Despite particles as large as 200μm are found in sediment traps in the North Atlantic (van der Does et al., 2016), the particle size in our model rarely exceeds 60μm (Fig. 2.5).

Consistent with the sudden increase in simulated dust deposition in the North Atlantic, simulated dust emission in the northwest Sahara rises rapidly between 6 and 4 ka BP. The areas of the strongest and fastest change in dust emissions are those of former paleolakes. In these areas, lakes disabled dust emission during the mid-Holocene. As soon as

the lakes desiccated, fine grained material was favored to be deflated by surface winds, which makes them a highly productive dust source today. In our simulations, lakes are prescribed to decline gradually. However, in Chapter 3 we found that a gradual decline of lakes and vegetation results in a rather gradual increase of North Atlantic dust deposition. Thus, the gradual desiccation of lakes is not the trigger of the abrupt dust deposition shift that we see in the current simulations. Instead, vegetation-climate feedbacks are key to explain the abrupt shift in North Atlantic dust deposition because in contrast to prescribed vegetation in Chapter 3 we have considered dynamic vegetation in this chapter. We find a fast decline of vegetation cover in the western Sahara from 22°N to 18°N collocated with a strong reduction of precipitation, which points to local vegetation-precipitation feedbacks. Further, the composition of vegetation changes: Grasses are rapidly replaced by shrubs in the areas of strong dust emission rise. This suggests that dust emission is determined by the composition of vegetation types in addition to the vegetation cover fraction. As mentioned before, the simulated vegetation does not propagate sufficiently far north during the mid-Holocene compared to pollen records (Fig. 4.2). If the simulated vegetation would shift as far north as indicated by pollen records, we suspect that vegetation-precipitation feedbacks would have a more prominent role also north of 22°N and less dust would be emitted from there. Consequently, the absolute difference in Saharan dust emission and associated North Atlantic dust deposition would be higher between the mid-Holocene and the pre-industrial era, and the change in northwest Saharan vegetation, precipitation and dust emission would be as abrupt, if not even sharper than in our current simulations.

We find only small changes in wind speed in our simulations. The AEJ, the SAL and the major dust belt at the surface are relocated by approximately 5° to the north during the mid-Holocene in our simulation. As a consequence, the north-south gradient of dust deposition along the northwest African margin is reduced compared to the pre-industrial gradient, similarly to Chapter 2. Obviously, changes in wind speed play a minor role for the fast change in North Atlantic dust deposition.

In the northeast Sahara, there is only a slight increase in simulated dust emission north of 18°N between 6 and 5 ka BP. The rapid increase in simulated dust deposition in the North Atlantic is hence rather determined by a sudden rise in dust deflation from northwest Saharan dust sources than by an increase of northeast Saharan dust emission. South of 18°N, there is a strong but gradual decrease of vegetation cover and precipitation roughly between 5 and 2 ka BP. In this area, where trees, grasses and shrubs coexist in our simulations, the higher plant diversity could stabilize the system which results in a more gradual vegetation decline as shown by modeling studies (Claussen et al., 2013; Groner et al., 2015; Groner, 2017). However, the vegetation there is still too dense

to enable dust emission until 4 ka BP. Thereafter, dust emission rises only sightly and gradually until present.

While a previous study associated the abrupt shift in North Atlantic dust deposition indicated by sediment records to a large-scale change in North African landscape (deMenocal et al., 2000), we argue that records from a local site are not sufficient to draw conclusions on large-scale changes in landscape and climate conditions and a spatial distinction of source areas is necessary. For instance, at specific sites, we see a gradual shift in vegetation cover in our simulations as indicated by pollen data (Kröpelin et al., 2008) and a gradual change in dust emission as seen in reconstructions of aeolian dust accumulation (Cockerton et al., 2014) in contrast to the rapid changes in simulated vegetation cover and simulated dust emission in the much larger area of the northwest Sahara and the abrupt change in North Atlantic dust deposition. An abrupt signal in one area is not in contradiction with gradual changes in another area. Local sites rather give insights into past climate and surface conditions for a specific region. The identification of this region depends on meteorological and geographical conditions, such as wind strength and direction, the updraft of dust and the formation of convective systems, soil composition, surface moisture, surface cover and topography. An increase of the number of core sites would thus increase the robustness of the results and would help to clarify spatial differences in the end of the AHP.

An important result of our study is that vegetation-climate feedbacks are key to simulate an abrupt shift in North Atlantic dust deposition. In addition to vegetation-climate feedbacks, surface water-climate feedbacks (Krinner et al., 2012), SST-climate feedbacks (Zhao et al., 2005) as well as SST-dust feedbacks (Williams et al., 2016) were proposed as candidates to explain an abrupt end of the AHP. Due to the prescription of lakes and SST in our simulations, we could not assess the contribution of these feedbacks to an abrupt change in North Atlantic dust deposition. Just recently, the technical basis was provided to run ECHAM6-HAM2 with an interactive ocean under a moderate increase of computation time by about 20%, which paves the way to explore the role of ocean feedbacks in the context of Holocene dust transport. Feedbacks between surface waters and climate are neglected in our study due to the lack of an interactive lake module. Lakes are thus not in equilibrium with climate. Our prescribed lake surface distribution rather represents the maximal extent of lake surface area when precipitation is unlimited (Tegen et al., 2002). In reality, lakes respond individually to the climate forcing, depending on their size, depth and how they are fed: Some are rather supported directly by precipitation, whereas others are fed by sub-terrain aquifers or by rivers (Florence Sylvestre, personal conversation). Thus, the dynamics of lake surface and the effect of surface waters on climate remain difficult to assess in a global circulation model. Still, the implementation of a dynamical lake surface scheme in ECHAM6-HAM2 could

help to include the role of surface waters to Holocene climate change more realistically compared to a prescribed lake surface map.

Based on previous studies (Kutzbach and Liu, 1997; Coe and Bonan, 1997; Krinner et al., 2012; Williams et al., 2016), we expect that the inclusion of these missing feedbacks would further strengthen the West African monsoon and shift vegetation further northwards during the mid-Holocene. This would help to minimize the gap to pollen records, which predict more extensive precipitation and vegetation north of 20°N compared to our simulations. Also, we expect that the transition from the 'green' Sahara to the present-day desert would be accelerated when taking all feedbacks into account. Therefore, the abruptness of the change in North Atlantic dust deposition found in this chapter is still a lower estimate.

4.5 Conclusions

1. We find a rapid shift in North Atlantic dust deposition along the West African margin in our simulations about 5 to 4 ka BP in agreement with marine sediment records.

2. The rapid shift in simulated North Atlantic dust deposition during the Holocene is linked to a fast decline of vegetation cover in the western Sahara from 22°N to 18°N. Additionally, the strong reduction of lake surface area between 18°N and 26°N contributes to the rapid shift in dust deposition. Changes in Saharan landscape and dust emission south of 18°N and in the eastern Sahara as well as changes in atmospheric circulation play a minor role in driving the dynamics of North Atlantic dust deposition.

3. The fast decline of vegetation cover in the western Sahara from 22°N to 18°N is collocated with a strong reduction of precipitation, which points to strong local vegetation-precipitation feedbacks.

4. Our study emphasizes spatial and temporal differences in the transition of North African landscape. Implications from local data records on large-scale climate have thus to be treated with caution.

Chapter 5

Summary and perspectives

5.1 Summary of results

Marine sediment records show an abrupt increase in North Atlantic dust deposition about 5 ka BP (deMenocal et al., 2000; Adkins et al., 2006; McGee et al., 2013a; Albani et al., 2015), which was interpreted in previous studies as an indicator for an abrupt end of the AHP. However, the timing and abruptness of vegetation decline towards the end of the AHP is still highly debated. To investigate how changes in North Atlantic dust deposition are linked to changes in North African landscape during the Holocene, we have simulated the Holocene dust cycle using the coupled aerosol-climate model ECHAM6-HAM2. We thereby contribute to understanding the drivers, nature and transition of the Holocene dust cycle and its link to atmosphere and land surface conditions in North Africa.

In Chapter 2, we have studied the relative importance of atmosphere and land surface conditions on reduced North African dust emission and associated North Atlantic dust deposition during the mid-Holocene addressing the first question:

What is the cause of the large difference between mid-Holocene and pre-industrial dust deposition in the North Atlantic?

We have identified the expansion of North African land surface cover, including vegetation and lakes, as the main cause of the strong reduction in North Atlantic dust deposition during the mid-Holocene. Extended vegetation and lakes (1) cover dust source areas and thereby disable dust emission and (2) change the atmospheric circulation through enhanced evapotranspiration and a lower surface albedo. Changes in vegetation and lakes contribute thereby equally to the reduced dust cycle during the mid-Holocene. On the contrary, changes in atmosphere and ocean conditions alone are not sufficient to explain the large reduction in dust deposition. However, they have an impact on the annual

cycle of dust emission and add to the suppression of dust in combination with extensive land surface cover.

In Chapter 3, we have focused on the dynamics of the Holocene dust cycle. We have tested the hypothesis that a gradual decline of vegetation and lake cover results in an abrupt rise in North Atlantic dust deposition either because of the nonlinearity in dust activation or due to the heterogeneous distribution of major dust sources. Therewith, we have addressed the second question:

Could gradual changes in Holocene Saharan landscape have caused the observed abrupt shift in North Atlantic dust deposition?

In contrast to our hypothesis, the simulated dust deposition follows the prescribed changes in vegetation and lake cover almost linearly. Consistently, the simulated precipitation in North Africa declines gradually. This, in turn, suggests that any abrupt change in dust deposition into the North Atlantic could be associated with a fast change of Saharan land cover. Vegetation-climate feedbacks, that are not considered in this chapter due to the prescribed vegetation, could provoke such a fast landscape transition.

In Chapter 4, we have included vegetation-climate feedbacks by calculating the vegetation dynamically in the model to answer the third question:

How is the abrupt change in North Atlantic dust deposition spatially and temporally linked to Holocene Saharan landscape evolution?

We find a rapid increase in simulated dust deposition in the North Atlantic between 6 and 4 ka BP as indicated by the sediment records. Accordingly, simulated vegetation cover and precipitation shift rapidly southward from 22°N to 18°N in the western Sahara. Lakes are replaced by highly active dust sources resulting in a fast increase in simulated dust emission in the northwest Sahara. Changes in dust sources, vegetation and lakes in the eastern Sahara and south of 18°N as well as changes in atmospheric circulation have a minor contribution to the rapid change in North Atlantic dust deposition. In conclusion, vegetation-climate feedbacks in the area of significant dust sources in the northwest Sahara are crucial to explain the abrupt shift in dust deposition, because in Chapter 3, a gradual decrease of vegetation and lakes resulted in a gradual increase of North Atlantic dust deposition.

5.2 Future key challenges

In the following, we address the main shortcomings of our study and point to future key challenges that arise from these limitations.

Dust model

The implementation of dust emission, transport and deposition entails high uncertainties in the simulation results. Within the framework of the Global Aerosol Model Intercomparison (AeroCom) initiative, the dust budgets in 15 global models were compared. It was found that simulated present-day dust emission in North Africa varies by an order of magnitude between the models (Huneeus et al., 2011). These uncertainties are attributed to differences in (1) dust emission parametrization (Zender et al., 2004), (2) soil properties and soil moisture, and (3) the representation of peak winds (Knippertz and Todd, 2012). Dust emission is very sensitive to changes in peak winds. Small deviations in surface winds can result in significant different dust fluxes.

The coupled aerosol-climate model ECHAM6-HAM2 is designed to perform global simulations on a relatively low spatial resolution of e.g. roughly 200 x 200km. The model can resolve large-scale weather systems but is not capable to resolve smaller scale processes such as haboobs or microscale dust devils despite the fact that haboobs were associated with about 40% of the dust emission in North Africa (Heinold et al., 2013). How these processes might influence the dynamics of dust deflation can not be evaluated with our model. In addition to regional climate models, the global ICOsahedral Non-hydrostatic (ICON) General Circulation Model (Zängl et al., 2015) is a promising tool to resolve smaller scale processes regionally under moderate computation costs and thereby to help increase our process understanding in the future.

Model uncertainties contribute to the mismatch between models and observations. For example, particles as large as 200μm are found in sediment traps in the North Atlantic (van der Does et al., 2016), whereas the particle size in models rarely exceeds 60μm (Fig. 2.5). By neglecting large particles in the model, we may underestimate the contribution of long-wave radiation to the total radiative forcing in regions with a relatively high dust load (Stanelle et al., 2014). Minimizing the discrepancy between models and observations can only be achieved by a common effort of advanced and more detailed observational programs and an improvement of model parametrization concerning meteorological processes (Knippertz and Todd, 2012). Dust measurements over the ocean may improve the assessment of dust emission estimates in North Africa and the characterization of remote dust transport and deposition at modern times (Prospero and Mayol-Bracero, 2013).

Desiccated paleolakes are prescribed as preferential dust sources in the current dust emission scheme. As a result of this parametrization, emissions from paleolake basins in northwest Africa are likely overestimated in our pre-industrial simulation because those areas are not identified as major dust sources by e.g. the Meteosat satellite (Schepanski et al., 2012). Nevertheless, we argue that these are the areas of the maximal difference in dust emission between the mid-Holocene and the pre-industrial era because they were covered by lakes during the mid-Holocene. Thus, most likely, the patterns and dynamics of dust emission changes are captured fairly well in our study.

Pollen and sediment records

Pollen and sediment records serve as a valuable proxy to explore past climate change but also to identify local differences in past climates. Up to now, the spatial availability of paleo data in North Africa is very limited. Additional pollen and sediment records are required for model validation and to increase the robustness of model results, e.g. dust records from the remote North Atlantic similar to the ones of Williams et al. (2016) can help to constrain dust transport and deposition in the model. Especially in areas with high dust impact, sediment records offer a very detailed archive of past climates due to the high temporal resolution. However, inferences from local dust records on large scale climate have to be treated with caution as the cores rather represent the climate in a specific source region. This source region might be identified via the analysis of dust composition, back trajectory modeling (Stuut et al., 2005; van der Does et al., 2016), satellite observations (Schepanski et al., 2012) and simulations studies.

Dynamic vegetation

The dynamic vegetation scheme in JSBACH generates less vegetation in North Africa at present times than derived from satellite data (Eichhorn and Bader, 2016). During the mid-Holocene, the simulated vegetation does not extend sufficiently far north compared to pollen records (Jolly et al., 1998a). As a consequence, the strong dependence of potential dust source areas on vegetation results in an overestimation of dust emission. One reason for the underestimation of vegetation during the mid-Holocene could be the missing PFT plasticity due to fixed bioclimatic limits in the model, such as a minimum temperature for plant establishment. Thus, tropical trees are prevented from growing in the northern Sahara where pollen records indicate their existence during the AHP (Hély et al., 2014). The choice of such bioclimatic limits is reasonable and based on empirical relationships (Prentice et al., 1992; Muller, 2012). However, plants respond very individually to climate conditions and can adapt to their environment. A more flexible implementation of these limits that is adaptable to specific plant types and external conditions could help to increase consistency with data. Additionally, JSBACH lacks a realistic representation of specific plant types in North Africa, such as high perennial

grasses and dry forest trees including gallery forest trees (Groner, 2017). In Chapter 4, we found that dust emission is not only very sensitive to the vegetation distribution, but also to the composition of vegetation. The implementation of new functional types in JSBACH might improve the representation of plant diversity resulting in more realistic dust emission patterns.

Soil albedo

The scheme to simulate changes in soil albedo used in Chapter 4 is very simplified. It parametrizes soil processes by NPP, i.e. it only implicitly considers the darkening of the soil in vegetated areas due to e.g. plant litter. During the mid-Holocene, the reduced albedo due to extended vegetation led to a strengthening of the West African monsoon. The implementation of realistic albedo dynamics is thus important to reproduce mid-Holocene climate. Also, dust emission fluxes are found to be very sensitive to the albedo in our simulations (not shown). A more sophisticated soil albedo scheme was designed by Vamborg et al. (2011), which takes both fast and slow vegetation processes into account. However, a long spin-up time of several hundred years is necessary to bring the carbon cycle in equilibrium and apply the scheme, which is inefficient for time slice simulations as in our study but more favorable for transient studies on the dust cycle. We assumed that for our purpose it is sufficient to rely on the simplified scheme because it generates the much lower soil albedo during the mid-Holocene reasonably well.

Dust feedbacks

In our study, we have restricted ourselves to regard dust as a proxy for Holocene climate and landscape change. Moreover, dust was highlighted as an active player in the climate system in previous studies. Dust has the potential to alter the surface radiation budget (Yoshioka et al., 2007; Spyrou et al., 2013), to impact precipitation patterns (Rosenfeld et al., 2001; Hui et al., 2008; Lau et al., 2009), to effect the strength of the AEJ (Tompkins et al., 2005), to alter the cloud structure (Lohmann, 2002), and it serves as a fertilizer for marine and terrestrial ecosystems (Mahowald et al., 2005). A change in atmospheric circulation or precipitation patterns due to dust could interfere with dust emission, transport and deposition processes, establishing a feedback loop between dust and climate. However, according to the Fifth Assessment Report of the Intergovernmental Panel on Climate Change (IPCC), uncertainties with regard to the sign and strength of dust feedbacks are high. To evaluate the impact of dust feedbacks on Holocene climate change, results from GCM studies may be combined with an extended version of a conceptual model on vegetation-precipitation interactions (Brovkin et al., 1998) that additionally considers dust as a component in the dynamic system. Thereby, the pace of Holocene climate and landscape change might be either slowed down or accelerated, depending on the dust feedback.

5.3 Conclusion and implications

The novelty of our study is the direct coupling of dust emission and land surface cover, including vegetation and lakes, in a global aerosol-climate model with application to Holocene climate change. For the first time, we are able to link the large increase in dust deposition, that was seen in marine dust records, directly to a strong reduction of North African land surface cover during the Holocene. Furthermore, we emphasize that local vegetation-climate feedbacks in specific dust source regions in northwest Africa are key to explain a rapid increase in simulated dust deposition in the North Atlantic. We highlight that a spatial distinction in the discussion about the timing and abruptness of Holocene climate change is essential. The interpretation of local dust records as indicator for large-scale landscape changes has thus to be treated with caution.

At present, the third phase of the Paleoclimate Modelling Intercompoarison Project (PMIP3) (Braconnot et al., 2011, 2012) demands pre-industrial dust distribution to be prescribed for mid-Holocene simulations. Dust has, however, a number of impacts on climate as described in 'Dust feedbacks' in Section 5.2. The importance of dust as an active player in the climate system was emphasized by the PMIP community as they discuss the inclusion of a more sophisticated mid-Holocene dust distribution scheme in the next PMIP phase (https://pmip3.lsce.ipsl.fr/). Our simulations offer a new perspective to prescribe a more realistic atmospheric dust load for mid-Holocene simulations. Alternatively, the potential to run ECHAM6-HAM2 with an interactive ocean under a moderate increase of computation time paves the way to perform fully coupled simulations instead of prescribing the dust load. In both cases, the discrepancy between the simulated northward extent of the West African monsoon and vegetation and paleo data could be most likely reduced. In that way, including dust in mid-Holocene climate simulations adds to our understanding of Holocene climate change.

Appendix A

Overview of model configurations

We present an overview of model configurations in the different chapters. The progressive development and installation of new hardware and software at the Max Planck Institute for Meteorology demanded the use of different model versions in different chapters throughout the years.

	Chapter 2	**Chapter 3**	**Chapter 4**
Model version	echam6.1-ham2.1	echam6.1-ham2.2	echam6.3-ham2.3
Model resolution	T63L31	T63L31	T63L31
Soil scheme	bucket scheme	bucket scheme	5-layer soil scheme
Soil albedo	prescribed (Dallmeyer, 2008)		dynamic (Zink, 2014)
SST, SIC	prescribed (Fischer and Jungclaus, 2011)		prescribed (Bader et al., in prep.)
Lakes			
-pre-industrial	prescribed based on satellite data (Loveland et al., 2000)		
-mid-Holocene	prescribed (Tegen et al., 2002)		
Vegetation			
-pre-industrial	prescribed based on satellite data (Loveland et al., 2000; Hagemann, 2002)	prescribed (Larrasoaña et al., 2013)	dynamic (Reick et al., 2013)
-mid-Holocene	prescribed (Hoelzmann et al., 1998)		

Table A.1: Model configurations in the different chapters.

Bibliography

Adkins, J., deMenocal, P., and Eshel, G. (2006). The "African Humid Period" and the Record of Marine Upwelling from Excess 230Th in ODP Hole 658C. *Paleoceanography*, 21.

Albani, S., Mahowald, N. M., Winckler, G., Anderson, R. F., Bradtmiller, L. I., Delmonte, B., François, R., Goman, M., Heavens, N. G., Hesse, P. P., Hovan, S. A., Kang, S. G., Kohfeld, K. E., Lu, H., Maggi, V., Mason, J. A., Mayewski, P. A., McGee, D., Miao, X., Otto-Bliesner, B. L., Perry, A. T., Pourmand, A., Roberts, H. M., Rosenbloom, N., Stevens, T., and Sun, J. (2015). Twelve thousand years of dust: the Holocene global dust cycle constrained by natural archives. *Climate of the Past*, 11(6):869–903.

Amaral, P. G. C., Vincens, A., Guiot, J., Buchet, G., Deschamps, P., Doumnang, J.-C., and Sylvestre, F. (2013). Palynological evidence for gradual vegetation and climate changes during the African Humid Period termination at 13°N from a Mega-Lake Chad sedimentary sequence. *Climate of the Past*, 9(1):223–241.

Armitage, S. J., Bristow, C. S., and Drake, N. A. (2015). West African monsoon dynamics inferred from abrupt fluctuations of Lake Mega-Chad. *Proceedings of the National Academy of Sciences*.

Bagnold, R. (1941). The physics of blown sand and desert dunes. page 266 S.

Bartlein, P. (2011). Pollen-based continental climate reconstructions at 6 and 21 ka: a global synthesis. *Climate Dynamics*, 37(3-4):775–802.

Berger, A. (1978). Long-term variations of daily insolation and quaternary climatic changes. *J. Atmos. Sci.*, 35:2362–2367.

Bory, A. J.-M. and Newton, P. P. (2000). Transport of airborne lithogenic material down through the water column in two contrasting regions of the eastern subtropical North Atlantic Ocean. *Global Biogeochemical Cycles*, 14(1):297–315.

Braconnot, P., Harrison, S., Kageyama, M., Bartlein, P. J., Masson-Delmotte, V., Abe-Ouchi, A., Otto-Bliesner, B., and Zhao, Y. (2012). Evaluation of climate models using palaeoclimatic data. *Nature Clim. Change*, 2(2):417–424.

Braconnot, P., Harrison, S., Otto-Bliesner, B., and Peterchmitt, J.-Y. (2011). The Paleoclimate Modeling Intercomparison Project contribution to CMIP5. *CLIVAR Exchanges*, 16(56):15–19.

Braconnot, P., Otto-Bliesner, B., Harrison, S., Joussaume, S., Peterchmitt, J.-Y., Abe-Ouchi, A., Crucifix, M., Driesschaert, E., Fichefet, T., Hewitt, C. D., Kageyama, M., Kitoh, A., Laîné, A., Loutre, M.-F., Marti, O., Merkel, U., Ramstein, G., Valdes, P., Weber, S. L., Yu, Y., and Zhao, Y. (2007). Results of PMIP2 coupled simulations of the Mid-Holocene and Last Glacial Maximum; Part 1: experiments and large-scale features. *Climate of the Past*, 3(2):261–277.

Bradtmiller, L. I., McGee, D., Awalt, M., Evers, J., Yerxa, H., Kinsley, C. W., and deMenocal, P. B. (2016). Changes in biological productivity along the northwest African margin over the past 20,000 years. *Paleoceanography*, 31(1):185–202. 2015PA002862.

Brovkin, V., Claussen, M., Petoukhov, V., and Ganopolski, A. (1998). On the stability of the atmosphere-vegetation system in the Sahara/Sahel region. *Journal of Geophysical Research: Atmospheres*, 103(D24):31613–31624.

Capps, S. B. and Zender, C. S. (2008). Observed and CAM3 GCM Sea Surface Wind Speed Distributions: Characterization, Comparison, and Bias Reduction. *Journal of Climate*, 21(24):6569–6585.

Carlson, T. and Prospero, J. (1972). The large-scale movement of Saharan Air outbreaks over the Northern Equatorial Atlantic. *J. Appl. Meteor.*, 11:283–297.

Charney, J. G. (1975). Dynamics of deserts and drought in the Sahel. *Quarterly Journal of the Royal Meteorological Society*, 101(428):193–202.

Claussen, Bathiany S., Brovkin V., and Kleinen T. (2013). Simulated climate-vegetation interaction in semi-arid regions affected by plant diversity. *Nature Geosci*, 6(11):954–958.

Claussen, M. (1998). On multiple solutions of the atmosphere–vegetation system in present-day climate. *Global Change Biology*, 4(5):549–559.

Claussen, M. and Gayler, V. (1997). The Greening of the Sahara during the Mid-Holocene: Results of an Interactive Atmosphere-Biome Model. *Global Ecology and Biogeography Letters*, 6(5):369–377.

Claussen, M., Kubatzki, C., Brovkin, V., Ganopolski, A., Hoelzmann, P., and Pachur, H.-J. (1999). Simulation of an abrupt change in Saharan vegetation in the Mid-Holocene. *Geophysical Research Letters*, 26(14):2037–2040.

Cockerton, H. E., Holmes, J. A., Street-Perrott, F. A., and Ficken, K. J. (2014). Holocene dust records from the West African Sahel and their implications for changes in climate and land surface conditions. *Journal of Geophysical Research: Atmospheres*, 119(14):8684–8694.

Coe, M. T. (1998). A linked global model of terrestrial hydrologic processes: Simulation of modern rivers, lakes, and wetlands. *Journal of Geophysical Research: Atmospheres*, 103(D8):8885–8899.

Coe, M. T. and Bonan, G. B. (1997). Feedbacks between climate and surface water in northern Africa during the middle Holocene. *Journal of Geophysical Research: Atmospheres*, 102(D10):11087–11101.

Cook, K. H. (1999). Generation of the African Easterly Jet and Its Role in Determining West African Precipitation. *Journal of Climate*, 12(5):1165–1184.

Crouvi, O., Schepanski, K., Amit, R., Gillespie, A. R., and Enzel, Y. (2012). Multiple dust sources in the Sahara Desert: The importance of sand dunes. *Geophysical Research Letters*, 39(13). L13401.

Dallmeyer, A. (2008). Simulation des Nordafrikanischen Sommermonsuns in ECHAM5-Analyse der Modellempfindlichkeit. Master's thesis, Universität Hamburg.

deMenocal, P., Ortiz, J., Guilderson, T., Adkins, J., Sarnthein, M., Baker, L., and Yarusinsky, M. (2000). Abrupt onset and termination of the African Humid Period:: rapid climate responses to gradual insolation forcing. *Quaternary Science Reviews*, 19(1–5):347–361.

Doherty, R., Kutzbach, J., Foley, J., and Pollard, D. (2000). Fully coupled climate/-dynamical vegetation model simulations over Northern Africa during the mid-Holocene. *Climate Dynamics*, 16(8):561–573.

Drake, N. A., Blench, R. M., Armitage, S. J., Bristow, C. S., and White, K. H. (2011). Ancient watercourses and biogeography of the Sahara explain the peopling of the desert. *Proceedings of the National Academy of Sciences*, 108(2):458–462.

Egerer, S., Claussen, M., Reick, C., and Stanelle, T. (2016). The link between marine sediment records and changes in Holocene Saharan landscape: simulating the dust cycle. *Climate of the Past*, 12(4):1009–1027.

Egerer, S., Claussen, M., Reick, C., and Stanelle, T. (2017). Could gradual changes in Holocene Saharan landscape have caused the observed abrupt shift in North Atlantic dust deposition? *Earth and Planetary Science Letters*, 473:104–112.

Eichhorn, A. and Bader, J. (2016). Impact of tropical Atlantic sea-surface temperature biases on the simulated atmospheric circulation and precipitation over the Atlantic region: An ECHAM6 model study. *Climate Dynamics*, pages 1–15.

Engelstaedter, S., Tegen, I., and Washington, R. (2006). North African dust emissions and transport. *Earth-Science Reviews*, 79(1–2):73–100.

Engelstaedter, S. and Washington, R. (2007). Atmospheric controls on the annual cycle of North African dust. *Journal of Geophysical Research: Atmospheres*, 112(D3).

Fiedler, S., Kaplan, M. L., and Knippertz, P. (2015). The importance of Harmattan surges for the emission of North African dust aerosol. *Geophysical Research Letters*, 42(21):9495–9504.

Fiedler, S., Schepanski, K., Heinold, B., Knippertz, P., and Tegen, I. (2013). Climatology of nocturnal low-level jets over North Africa and implications for modeling mineral dust emission. *Journal of Geophysical Research: Atmospheres*, 118(12):6100–6121.

Fiedler, S., Schepanski, K., Knippertz, P., Heinold, B., and Tegen, I. (2014). How important are atmospheric depressions and mobile cyclones for emitting mineral dust aerosol in North Africa? *Atmospheric Chemistry and Physics*, 14(17):8983–9000.

Fink, A. H. (2006). Das Westafrikanische Monsunsystem. *Promet*, Jahrg. 32(Heft 3/4):114–122.

Fischer, G., Donner, B., Ratmeyer, V., Davenport, R., and Wefer, G. (1996). Distinct year-to-year flux variations off Cape Blanc during 1988-1991: relation to 18O-deduced sea-surface temperatures and trade winds. *Journal of Marine Research*, 54:73–98.

Fischer, N. and Jungclaus, J. H. (2011). Evolution of the seasonal temperature cycle in a transient Holocene simulation: orbital forcing and sea-ice. *Climate of the Past*, 7(4):1139–1148.

Gasse, F. (2000). Hydrological changes in the African tropics since the Last Glacial Maximum. *Quaternary Science Reviews*, 19(1–5):189–211.

Giorgetta, M. A., Jungclaus, J., Reick, C. H., Legutke, S., Bader, J., Böttinger, M., Brovkin, V., Crueger, T., Esch, M., Fieg, K., Glushak, K., Gayler, V., Haak, H.,

Hollweg, H.-D., Ilyina, T., Kinne, S., Kornblueh, L., Matei, D., Mauritsen, T., Mikolajewicz, U., Mueller, W., Notz, D., Pithan, F., Raddatz, T., Rast, S., Redler, R., Roeckner, E., Schmidt, H., Schnur, R., Segschneider, J., Six, K. D., Stockhause, M., Timmreck, C., Wegner, J., Widmann, H., Wieners, K.-H., Claussen, M., Marotzke, J., and Stevens, B. (2013). Climate and carbon cycle changes from 1850 to 2100 in MPI-ESM simulations for the Coupled Model Intercomparison Project phase 5. *Journal of Advances in Modeling Earth Systems*, 5(3):572–597.

Goudie, A. and Middleton, N. (2001). Saharan dust storms: nature and consequences. *Earth-Science Reviews*, 56(1–4):179–204.

Groner, V. P. (2017). *Effects of plant diversity on simulated climate-vegetation interaction towards the end of the African Humid Period*. PhD thesis, Universität Hamburg.

Groner, V. P., Claussen, M., and Reick, C. (2015). Palaeo plant diversity in subtropical Africa – ecological assessment of a conceptual model of climate–vegetation interaction. *Climate of the Past*, 11(10):1361–1374.

Hagemann, S. (2002). An improved land surface parameter dataset for global and regional climate models. *MPI Report No. 289, Max Planck Institute for Meteorology, Hamburg*.

Hales, K., Neelin, J. D., and Zeng, N. (2004). Sensitivity of Tropical Land Climate to Leaf Area Index: Role of Surface Conductance versus Albedo. *Journal of Climate*, 17(7):1459–1473.

Hargreaves, J. C., Annan, J. D., Ohgaito, R., Paul, A., and Abe-Ouchi, A. (2013). Skill and reliability of climate model ensembles at the Last Glacial Maximum and mid-Holocene. *Climate of the Past*, 9(2):811–823.

Harrison, S. P., Bartlein, P., Izumi, K., Li, G., Annan, J., Hargreaves, J., Braconnot, P., and Kageyama, M. (2015). Evaluation of CMIP5 palaeo-simulations to improve climate projections. *Nature Climate Change*, 5(8):735.

Harrison, S. P., Kohfeld, K. E., Roelandt, C., and Claquin, T. (2001). The role of dust in climate changes today, at the last glacial maximum and in the future. *Earth-Science Reviews*, 54(1–3):43–80.

Heinold, B., Knippertz, P., Marsham, J. H., Fiedler, S., Dixon, N. S., Schepanski, K., Laurent, B., and Tegen, I. (2013). The role of deep convection and nocturnal low-level jets for dust emission in summertime West Africa: Estimates from convection-permitting simulations. *Journal of Geophysical Research: Atmospheres*, 118(10):4385–4400.

Hély, C., Lézine, A.-M., and contributors, A. (2014). Holocene changes in African vegetation: tradeoff between climate and water availability. *Climate of the Past*, 10(2):681–686.

Herman, J. R., Bhartia, P. K., Torres, O., Hsu, C., Seftor, C., and Celarier, E. (1997). Global distribution of UV-absorbing aerosols from Nimbus 7/TOMS data. *Journal of Geophysical Research: Atmospheres*, 102(D14):16911–16922.

Hoelzmann, P., Jolly, D., Harrison, S. P., Laarif, F., Bonnefille, R., and Pachur, H.-J. (1998). Mid-Holocene land-surface conditions in northern Africa and the Arabian Peninsula: A data set for the analysis of biogeophysical feedbacks in the climate system. *Global Biogeochemical Cycles*, 12(1):35–51.

Hui, W. J., Cook, B. I., Ravi, S., Fuentes, J. D., and D'Odorico, P. (2008). Dust-rainfall feedbacks in the West African Sahel. *Water Resources Research*, 44(5).

Huneeus, N., Schulz, M., Balkanski, Y., Griesfeller, J., Prospero, J., Kinne, S., Bauer, S., Boucher, O., Chin, M., Dentener, F., Diehl, T., Easter, R., Fillmore, D., Ghan, S., Ginoux, P., Grini, A., Horowitz, L., Koch, D., Krol, M. C., Landing, W., Liu, X., Mahowald, N., Miller, R., Morcrette, J.-J., Myhre, G., Penner, J., Perlwitz, J., Stier, P., Takemura, T., and Zender, C. S. (2011). Global dust model intercomparison in AeroCom phase I. *Atmospheric Chemistry and Physics*, 11(15):7781–7816.

Irizarry-Ortiz, M. M., Wang, G., and Eltahir, E. A. B. (2003). Role of the biosphere in the mid-Holocene climate of West Africa. *Journal of Geophysical Research: Atmospheres*, 108(D2):ACL 5–1–ACL 5–15. 4042.

Iversen, J. D. and White, B. R. (1982). Saltation threshold on Earth, Mars and Venus. *Sedimentology*, 29(1):111–119.

Janiga, M. A. and Thorncroft, C. D. (2016). The Influence of African Easterly Waves on Convection over Tropical Africa and the East Atlantic. *Monthly Weather Review*, 144(1):171–192.

Janssen, R. H. H., Meinders, M. B. J., Van Nes, E. H., and Scheffer, M. (2008). Microscale vegetation-soil feedback boosts hysteresis in a regional vegetation–climate system. *Global Change Biology*, 14(5):1104–1112.

Jemmett-Smith, B. C., Marsham, J. H., Knippertz, P., and Gilkeson, C. A. (2015). Quantifying global dust devil occurrence from meteorological analyses. *Geophysical Research Letters*, 42(4):1275–1282.

Jickells, T., Newton, P., King, P., Lampitt, R., and Boutle, C. (1996). A comparison of sediment trap records of particle fluxes from 19 to 48ÂřN in the northeast Atlantic and their relation to surface water productivity. *Deep Sea Research Part I: Oceanographic Research Papers*, 43(7):971–986.

Jolly, D., Harrison, S. P., Damnati, B., and Bonnefille, R. (1998a). Simulated climate and biomes of Africa during the Late Quaternary: comparison with pollen and lake status data. *Quaternary Science Reviews*, 17(6-7):629–657.

Jolly, D., Prentice, I. C., Bonnefille, R., Ballouche, A., Bengo, M., Brenac, P., Buchet, G., Burney, D., Cazet, J.-P., Cheddadi, R., Edorh, T., Elenga, H., Elmoutaki, S., Guiot, J., Laarif, F., Lamb, H., Lezine, A.-M., Maley, J., Mbenza, M., Peyron, O., Reille, M., Reynaud-Farrera, I., Riollet, G., Ritchie, J. C., Roche, E., Scott, L., Ssemmanda, I., Straka, H., Umer, M., Van Campo, E., Vilimumbalo, S., Vincens, A., and Waller, M. (1998b). Biome reconstruction from pollen and plant macrofossil data for Africa and the Arabian peninsula at 0 and 6000 years. *Journal of Biogeography*, 25(6):1007–1027.

Jones, C., Mahowald, N., and Luo, C. (2003). The Role of Easterly Waves on African Desert Dust Transport. *Journal of Climate*, 16(22):3617–3628.

Joussaume, S., Taylor, K. E., Braconnot, P., Mitchell, J. F. B., Kutzbach, J. E., Harrison, S. P., Prentice, I. C., Broccoli, A. J., Abe-Ouchi, A., Bartlein, P. J., Bonfils, C., Dong, B., Guiot, J., Herterich, K., Hewitt, C. D., Jolly, D., Kim, J. W., Kislov, A., Kitoh, A., Loutre, M. F., Masson, V., McAvaney, B., McFarlane, N., de Noblet, N., Peltier, W. R., Peterschmitt, J. Y., Pollard, D., Rind, D., Royer, J. F., Schlesinger, M. E., Syktus, J., Thompson, S., Valdes, P., Vettoretti, G., Webb, R. S., and Wyputta, U. (1999). Monsoon changes for 6000 years ago: Results of 18 simulations from the Paleoclimate Modeling Intercomparison Project (PMIP). *Geophysical Research Letters*, 26(7):859–862.

Jungclaus, J. H., Keenlyside, N., Botzet, M., Haak, H., Luo, J.-J., Latif, M., Marotzke, J., Mikolajewicz, U., and Roeckner, E. (2006). Ocean Circulation and Tropical Variability in the Coupled Model ECHAM5/MPI-OM. *Journal of Climate*, 19(16):3952–3972.

Kalnay, E., Kanamitsu, M., Kistler, R., Collins, W., Deaven, D., Gandin, L., Iredell, M., Saha, S., White, G., Woollen, J., Zhu, Y., Leetmaa, A., Reynolds, R., Chelliah, M., Ebisuzaki, W., Higgins, W., Janowiak, J., Mo, K. C., Ropelewski, C., Wang, J., Jenne, R., and Joseph, D. (1996). The NCEP/NCAR 40-Year Reanalysis Project. *Bulletin of the American Meteorological Society*, 77(3):437–471.

Karyampudi, V. M. and Carlson, T. N. (1988). Analysis and Numerical Simulations of the Saharan Air Layer and Its Effect on Easterly Wave Disturbances. *Journal of the Atmospheric Sciences*, 45(21):3102–3136.

Knippertz, P. and Todd, M. C. (2012). Mineral dust aerosols over the Sahara: Meteorological controls on emission and transport and implications for modeling. *Reviews of Geophysics*, 50(1).

Koch, J. and Renno, N. O. (2005). The role of convective plumes and vortices on the global aerosol budget. *Geophysical Research Letters*, 32(18).

Korte, L. F., Brummer, G.-J. A., van der Does, M., Guerreiro, C. V., Hennekam, R., van Hateren, J. A., Jong, D., Munday, C. I., Schouten, S., and Stuut, J.-B. W. (2017). Downward particle fluxes of biogenic matter and Saharan dust across the equatorial North Atlantic. *Atmospheric Chemistry and Physics*, 17(9):6023–6040.

Kremling, K. and Streu, P. (1993). Saharan dust influenced trace element fluxes in deep North Atlantic subtropical waters. *Deep Sea Research Part I: Oceanographic Research Papers*, 40(6):1155–1168.

Krinner, G., Lézine, A.-M., Braconnot, P., Sepulchre, P., Ramstein, G., Grenier, C., and Gouttevin, I. (2012). A reassessment of lake and wetland feedbacks on the North African Holocene climate. *Geophysical Research Letters*, 39(L07701).

Kröpelin, S., Verschuren, D., Lézine, A.-M., Eggermont, H., Cocquyt, C., Francus, P., Cazet, J.-P., Fagot, M., Rumes, B., Russell, J. M., Darius, F., Conley, D. J., Schuster, M., von Suchodoletz, H., and Engstrom, D. R. (2008). Climate-Driven Ecosystem Succession in the Sahara: The Past 6000 Years. *Science*, 320(5877):765–768.

Kuper, R. and Kröpelin, S. (2006). Climate-controlled Holocene occupation in the Sahara: motor of Africa's evolution. *Science (New York, N.Y.)*, 313(5788):803–807.

Kutzbach, J., Bonan, G., Foley, J., and Harrison, S. P. (1996). Vegetation and soil feedbacks on the response of the African monsoon to orbital forcing in the early to middle Holocene. *Nature*, 384(6610):623–626.

Kutzbach, J. E. (1981). Monsoon Climate of the Early Holocene: Climate Experiment with the Earth's Orbital Parameters for 9000 Years Ago. *Science*, 214(4516):59–61.

Kutzbach, J. E. and Liu, Z. (1997). Response of the African Monsoon to Orbital Forcing and Ocean Feedbacks in the Middle Holocene. *Science*, 278(5337):440–443.

Kutzbach, J. E. and Otto-Bliesner, B. L. (1982). The sensitivity of the african-asian monsoonal climate to orbital parameter changes for 9000 years b.p. in a low-resolution general circulation model. *J. Atmos. Sci.*, 39:1177–1188.

Kutzbach, J. E. and Street-Perrott, F. A. (1985). Milankovitch forcing of fluctuations in the level of tropical lakes from 18 to 0 kyr BP. *Nature*, 317(6033):130–134.

Lafore, J.-P., Flamant, C., Guichard, F., Parker, D. J., Bouniol, D., Fink, A. H., Giraud, V., Gosset, M., Hall, N., Höller, H., Jones, S. C., Protat, A., Roca, R., Roux, F., Said, F., and Thorncroft, C. (2011). Progress in understanding of weather systems in West Africa. *Atmospheric Science Letters*, 12(1):7–12.

Larrasoaña, J. C., P., R. A., and J., R. E. (2013). Dynamics of Green Sahara Periods and Their Role in Hominin Evolution. *PLOS ONE*, 8(10):1–12.

Lau, K. M., Kim, K. M., Sud, Y. C., and Walker, G. K. (2009). A GCM study of the response of the atmospheric water cycle of West Africa and the Atlantic to Saharan dust radiative forcing. *Annales Geophysicae*, 27(10):4023–4037.

Lawson, T. (1971). Haboob structure at Khartoum. *Weather*, 26(3):105–112.

Lézine, A.-M., Zheng, W., Braconnot, P., and Krinner, G. (2011). Late Holocene plant and climate evolution at Lake Yoa, northern Chad: pollen data and climate simulations. *Climate of the Past*, 7:1351–1362.

Lin, S.-J. and Rood, R. B. (1996). Multidimensional Flux-Form Semi-Lagrangian Transport Schemes. *Monthly Weather Review*, 124(9):2046–2070.

Liu, Z., Notaro, M., and Gallimore, R. (2010). Indirect vegetation–soil moisture feedback with application to Holocene North Africa climate1. *Global Change Biology*, 16(6):1733–1743.

Liu, Z., Notaro, M., Kutzbach, J., and Liu, N. (2006). Assessing Global Vegetation Climate Feedbacks from Observations*. *Journal of Climate*, 19:787.

Liu, Z., Wang, Y., Gallimore, R., Gasse, F., Johnson, T., Adkins, J., Notaro, M., Prentice, I., Kutzbach, J., Jacob, R., Behling, P., Wang, L., and Ong, E. (2007). Simulating the transient evolution and abrupt change of Northern Africa atmosphere–ocean–terrestrial ecosystem in the Holocene. *Quaternary Science Reviews*, 26(13–14):1818–1837.

Lohmann, U. (2002). Possible Aerosol Effects on Ice Clouds via Contact Nucleation. *Journal of the Atmospheric Sciences*, 59(3):647–656.

Loveland, T., Reed, B., Brown, J., Ohlen, D., Zhu, Z., Yang, L., and Merchant, J. (2000). Development of a global land cover characteristics database and IGBP DISCover from 1 km AVHRR data. *International Journal of Remote Sensing*, 21(6-7):1303–1330.

Mahowald, N., Albani, S., Kok, J. F., Engelstaeder, S., Scanza, R., Ward, D. S., and Flanner, M. G. (2014). The size distribution of desert dust aerosols and its impact on the Earth system. *Aeolian Research*, 15:53–71.

Mahowald, N., Kohfeld, K., Hansson, M., Balkanski, Y., Harrison, S. P., Prentice, I. C., Schulz, M., and Rodhe, H. (1999). Dust sources and deposition during the last glacial maximum and current climate: A comparison of model results with paleodata from ice cores and marine sediments. *Journal of Geophysical Research: Atmospheres*, 104(D13):15895–15916.

Mahowald, N. M., Baker, A. R., Bergametti, G., Brooks, N., Duce, R. A., Jickells, T. D., Kubilay, N., Prospero, J. M., and Tegen, I. (2005). Atmospheric global dust cycle and iron inputs to the ocean. *Global Biogeochemical Cycles*, 19(4):n/a–n/a. GB4025.

Marticorena, B. and Bergametti, G. (1995). Modeling the atmospheric dust cycle: 1. Design of a soil-derived dust emission scheme. *Journal of Geophysical Research: Atmospheres*, 100(D8):16415–16430.

McGee, D., deMenocal, P., Winckler, G., Stuut, J., and Bradtmiller, L. (2013a). The magnitude, timing and abruptness of changes in North African dust deposition over the last 20,000yr. *Earth and Planetary Science Letters*, 371–372(0):163–176.

McGee, D., deMenocal, P., Winckler, G., Stuut, J.-B. W., and Bradtmiller, L. I. (2013b). Reconstructions of eolian dust accumulation in northwest African margin sediments. *PANGAEA*.

Middleton, N. J. and Goudie, A. S. (2001). Saharan dust: sources and trajectories. *Transactions of the Institute of British Geographers*, 26(2):165–181.

Muller, M. J. (2012). *Selected climatic data for a global set of standard stations for vegetation science*, volume 5. Springer Science & Business Media.

Nicholson, S. E. (2009). A revised picture of the structure of the "monsoon" and land ITCZ over West Africa. *Climate Dynamics*, 32(7):1155–1171.

Nicholson, S. E. and Grist, J. P. (2003). The Seasonal Evolution of the Atmospheric Circulation over West Africa and Equatorial Africa. *Journal of Climate*, 16(7):1013–1030.

Niedermeyer, E. M., Schefuß, E., Sessions, A. L., Mulitza, S., Mollenhauer, G., Schulz, M., and Wefer, G. (2010). Orbital- and millennial-scale changes in the hydrologic cycle and vegetation in the western African Sahel: insights from individual plant wax Îŧ'D and Îŧ'13C. *Quaternary Science Reviews*, 29(23–24):2996–3005.

Patricola, C. M. and Cook, K. H. (2007). Dynamics of the West African Monsoon under Mid-Holocene Precessional Forcing: Regional Climate Model Simulations. *Journal of Climate*, 20(4):694–716.

Pausata, F. S. R., Messori, G., and Zhang, Q. (2016). Impacts of dust reduction on the northward expansion of the African monsoon during the Green Sahara period. *Earth and Planetary Science Letters*, 434:298–307.

Perez-Sanz, A., Li, G., González-Sampériz, P., and Harrison, S. P. (2014). Evaluation of modern and mid-Holocene seasonal precipitation of the Mediterranean and northern Africa in the CMIP5 simulations. *Climate of the Past*, 10(2):551–568.

Prentice, I. C., Cramer, W., Harrison, S. P., Leemans, R., Monserud, R. A., and Solomon, A. M. (1992). Special Paper: A Global Biome Model Based on Plant Physiology and Dominance, Soil Properties and Climate. *Journal of Biogeography*, 19(2):117–134.

Prentice, I. C., Jolly, D., and 6000 Participants, B. (2000). Mid-Holocene and Glacial-Maximum Vegetation Geography of the Northern Continents and Africa. *Journal of Biogeography*, 27(3):507–519.

Prospero, J. M., Ginoux, P., Torres, O., Nicholson, S. E., and Gill, T. E. (2002). Environmental characterization of global sources of atmospheric soil dust identified with the Nimbus 7 Total Ozone Mapping Spectrometer (TOMS) absorbing aerosol product. *Reviews of Geophysics*, 40(1):2–1–2–31. 1002.

Prospero, J. M., Glaccum, R. A., and Nees, R. T. (1981). Atmospheric transport of soil dust from Africa to South America. *Nature*, 289(5798):570–572.

Prospero, J. M. and Mayol-Bracero, O. L. (2013). Understanding the Transport and Impact of African Dust on the Caribbean Basin. *Bulletin of the American Meteorological Society*, 94(9):1329–1337.

Pye, K. (1987). *Aeolian Dust and Dust Deposits*. Academic Press.

Rachmayani, R., Prange, M., and Schulz, M. (2015). North African vegetation–precipitation feedback in early and mid-Holocene climate simulations with CCSM3-DGVM. *Climate of the Past*, 11(2):175–185.

Raddatz, T., Reick, C., Knorr, W., Kattge, J., Roeckner, E., Schnur, R., Schnitzler, K.-G., Wetzel, P., and Jungclaus, J. (2007). Will the tropical land biosphere dominate the climate-carbon cycle feedback during the twenty-first century? *Climatic Dynamics*, 29 (6):565 – 574. Publisher: Springer.

Ratmeyer, V., Fischer, G., and Wefer, G. (1999). Lithogenic particle fluxes and grain size distributions in the deep ocean off northwest Africa: Implications for seasonal changes of aeolian dust input and downward transport. *Deep Sea Research Part I: Oceanographic Research Papers*, 46(8):1289–1337.

Reick, C. H., Raddatz, T., Brovkin, V., and Gayler, V. (2013). Representation of natural and anthropogenic land cover change in MPI-ESM. *Journal of Advances in Modeling Earth Systems*, 5(3):459–482.

Renssen, H., Brovkin, V., Fichefet, T., and Goosse, H. (2003). Holocene climate instability during the termination of the African Humid Period. *Geophysical Research Letters*, 30(4). 1184.

Roeckner, E., Bäuml, G., Bonaventura, L., Brokopf, R., Esch, M., Giorgetta, M., et al. (2003). The atmospheric general circulation model ECHAM 5. PART I: Model description. *Report / MPI für Meteorologie*, 349.

Rosenfeld, D., Rudich, Y., and Lahav, R. (2001). Desert dust suppressing precipitation: A possible desertification feedback loop. *Proceedings of the National Academy of Sciences*, 98(11):5975–5980.

Sarnthein, M. (1978). Sand deserts during glacial maximum and climatic optimum. *Nature*, 272:23–46.

Sarnthein, M., Tetzlaff, G., Koopmann, B., Wolter, K., and Pflaumann, U. (1981). Glacial and interglacial wind regimes over the eastern subtropical Atlantic and North-West Africa. *Nature*, 293:193–196.

Schepanski, K., Tegen, I., and Macke, A. (2012). Comparison of satellite based observations of Saharan dust source areas. *Remote Sensing of Environment*, 123:90–97.

Schuster, M., Roquin, C., Duringer, P., Brunet, M., Caugy, M., Fontugne, M., Mackaye, H. T., Vignaud, P., and Ghienne, J.-F. (2005). Holocene Lake Mega-Chad palaeoshorelines from space. *Quaternary Science Reviews*, 24(16–17):1821–1827.

Shanahan, T. M., McKay, N. P., Hughen, K. A., Overpeck, J. T., Otto-Bliesner, B., Heil, C. W., King, J., Scholz, C. A., and Peck, J. (2015). The time-transgressive termination of the African Humid Period. *Nature Geosci*, 8(2):140–144.

Shao, Y., Raupach, M. R., and Findlater, P. A. (1993). Effect of saltation bombardment on the entrainment of dust by wind. *Journal of Geophysical Research: Atmospheres*, 98(D7):12719–12726.

Skonieczny, C., Paillou, P., Bory, A., Bayon, G., Biscara, L., Crosta, X., Eynaud, F., Malaizé, B., Revel, M., Aleman, N., Barusseau, J.-P., Vernet, R., Lopez, S., and Grousset, F. (2015). African humid periods triggered the reactivation of a large river system in Western Sahara. *Nature Communications*, 6:8751.

Spyrou, C., Kallos, G., Mitsakou, C., Athanasiadis, P., Kalogeri, C., and Iacono, M. (2013). Modeling the radiative effects of desert dust on weather and regional climate. *Atmospheric Chemistry and Physics*, 13(11):5489–5504.

Stanelle, T., Bey, I., Raddatz, T., Reick, C., and Tegen, I. (2014). Anthropogenically induced changes in twentieth century mineral dust burden and the associated impact on radiative forcing. *Journal of Geophysical Research: Atmospheres*, 119(23):13,526–13,546.

Stein, U. and Alpert, P. (1993). Factor separation in numerical simulations. *J. Atmos. Sci.*, 50:2107–2115.

Stevens, B., Giorgetta, M., Esch, M., Mauritsen, T., Crueger, T., Rast, S., Salzmann, M., Schmidt, H., Bader, J., Block, K., Brokopf, R., Fast, I., Kinne, S., Kornblueh, L., Lohmann, U., Pincus, R., Reichler, T., and Roeckner, E. (2013). Atmospheric component of the MPI-M Earth System Model: ECHAM6. *Journal of Advances in Modeling Earth Systems*, 5(2):146–172.

Stier, P., Feichter, J., Kinne, S., Kloster, S., Vignati, E., Wilson, J., Ganzeveld, L., Tegen, I., Werner, M., Balkanski, Y., Schulz, M., Boucher, O., Minikin, A., and Petzold, A. (2005). The aerosol-climate model ECHAM5-HAM. *Atmospheric Chemistry and Physics*, 5(4):1125–1156.

Street-Perrott, F., Marchand, D., Roberts, N., and Harrison, S. (1989). Global lake-level variations from 18,000 to 0 years ago: A palaeoclimate analysis. Technical report, U.S. Department of Energy Technical Report.

Stuut, J.-B., Zabel, M., Ratmeyer, V., Helmke, P., Schefuß, E., Lavik, G., and Schneider, R. (2005). Provenance of present-day eolian dust collected off NW Africa. *Journal of Geophysical Research: Atmospheres*, 110(D4). D04202.

Sudarchikova, N. (2012). *Modeling of mineral dust in the Southern Hemisphere with focus on Antarctica for interglacial and glacial climate conditions*. PhD thesis, Universität Hamburg.

Sudarchikova, N., Mikolajewicz, U., Timmreck, C., O'Donnell, D., Schurgers, G., Sein, D., and Zhang, K. (2015). Modelling of mineral dust for interglacial and glacial climate conditions with a focus on Antarctica. *Climate of the Past*, 11(5):765–779.

Sutton, L. J. (1925). Haboobs. *Quarterly Journal of the Royal Meteorological Society*, 51(213):25–30.

Taylor, K. E., Stouffer, R., and Meehl, G. (2011). An overview of CMIP5 and the experiment design. *Bull. Amer. Meteorol. Soc.*, 93:485–498.

Tegen, I., Harrison, S. P., Kohfeld, K., Prentice, I. C., Coe, M., and Heimann, M. (2002). Impact of vegetation and preferential source areas on global dust aerosol: Results from a model study. *Journal of Geophysical Research: Atmospheres*, 107(D21):AAC 14–1–AAC 14–27.

Tiedemann, R., Sarnthein, M., and Stein, R. (1989). Climatic changes in the western Sahara: Aeolo-marine sediment record of the last 8 million years (Sites 657-661). *Proceedings ODP, Scientific results*, 108:241–278.

Tjallingii, R., Claussen, M., Stuut, J.-B. W., Fohlmeister, J., Jahn, A., Bickert, T., Lamy, F., and Rohl, U. (2008). Coherent high- and low-latitude control of the northwest African hydrological balance. *Nature Geosci*, 1(10):670–675.

Tompkins, A. M., Cardinali, C., Morcrette, J.-J., and Rodwell, M. (2005). Influence of aerosol climatology on forecasts of the African Easterly Jet. *Geophysical Research Letters*, 32(10).

Vamborg, F., Brovkin, V., and Claussen, M. (2011). The effect of dynamic background albedo scheme on Sahel/Sahara precipitation during the Mid-Holocene. *Climate of the Past*, 7:117–131.

van der Does, M., Korte, L. F., Munday, C. I., Brummer, G.-J. A., and Stuut, J.-B. W. (2016). Particle size traces modern Saharan dust transport and deposition across the equatorial North Atlantic. *Atmospheric Chemistry and Physics*, 16(21):13697–13710.

Wefer, G. and Fischer, G. (1993). Seasonal patterns of vertical particle flux in equatorial and coastal upwelling areas of the eastern Atlantic. *Deep Sea Research Part I: Oceanographic Research Papers*, 40(8):1613–1645.

Weldeab, S., Lea, D. W., Schneider, R. R., and Andersen, N. (2007). 155,000 Years of West African Monsoon and Ocean Thermal Evolution. *Science*, 316(5829):1303–1307.

Werner, M., Tegen, I., Harrison, S. P., Kohfeld, K. E., Prentice, I. C., Balkanski, Y., Rodhe, H., and Roelandt, C. (2002). Seasonal and interannual variability of the mineral dust cycle under present and glacial climate conditions. *Journal of Geophysical Research: Atmospheres*, 107(D24):AAC 2–1–AAC 2–19.

White, B. R. (1979). soil transport by winds on Mars. *Journal of Geophysical Research: Solid Earth*, 84(B9):4643–4651.

Williams, R. H., McGee, D., Kinsley, C. W., Ridley, D. A., Hu, S., Fedorov, A., Tal, I., Murray, R. W., and deMenocal, P. B. (2016). Glacial to Holocene changes in trans-Atlantic Saharan dust transport and dust-climate feedbacks. *Science Advances*, 2(11).

Yoshioka, M., Mahowald, N. M., Conley, A. J., Collins, W. D., Fillmore, D. W., Zender, C. S., and Coleman, D. B. (2007). Impact of Desert Dust Radiative Forcing on Sahel Precipitation: Relative Importance of Dust Compared to Sea Surface Temperature Variations, Vegetation Changes, and Greenhouse Gas Warming. *Journal of Climate*, 20(8):1445–1467.

Zängl, G., Reinert, D., Rípodas, P., and Baldauf, M. (2015). The ICON (ICOsahedral Non-hydrostatic) modelling framework of DWD and MPI-M: Description of the non-hydrostatic dynamical core. *Quarterly Journal of the Royal Meteorological Society*, 141(687):563–579.

Zender, C. S., Miller, R. L. L., and Tegen, I. (2004). Quantifying mineral dust mass budgets:Terminology, constraints, and current estimates. *Eos, Transactions American Geophysical Union*, 85(48):509–512.

Zhang, K., O'Donnell, D., Kazil, J., Stier, P., Kinne, S., Lohmann, U., Ferrachat, S., Croft, B., Quaas, J., Wan, H., Rast, S., and Feichter, J. (2012). The global aerosol-climate model ECHAM-HAM, version 2: sensitivity to improvements in process representations. *Atmospheric Chemistry and Physics*, 12(19):8911–8949.

Zhao, Y., Braconnot, P., Marti, O., Harrison, S., Hewitt, C., Kitoh, A., Liu, Z., Mikolajewicz, U., Otto-Bliesner, B., and Weber, S. (2005). A multi-model analysis of the role of the ocean on the African and Indian monsoon during the mid-Holocene. *Climate Dynamics*, 25(7):777–800.

Zink, K. (2014). Einfluss der Konvektionsparametrisierung auf die Dynamik der Wechselwirkung Atmosphäre-Vegetation in Nordafrika. Master's thesis, Universität Hamburg.

Acknowledgements

First of all, I would like to gratefully acknowledge the providence, engagement and positive spirit of my principal supervisor, Martin Claußen, and I gratefully thank my second supervisor Christian Reick for the long discussions, his patience and inspiration.

I would further like to thank my unofficial supervisor, double co-author and remote supply Tanja Stanelle and with her the technical supply of the ECHAM-HAM team, especially Sylvaine Ferrachat for all her patience.

Many thanks to Thomas Raddatz for all the help with model and programming questions and for the endless stream of information.

Thousand thanks to Antje, Connie and Wiebke for making (organization) life so much easier and for teaching me that many things are possible if you just try hard enough.

I would like to heartily thank Vivi, Thomas, Johannes, Dirk, Raphaela, Sebastian, Alex, Tanja and Stephanie for proofreading.

Special thanks to Sebastian Bathiany for letting me take over his office, supervisor, flat and friends (basically his life).

Thanks to my lovely flatmates Markus, Jörn, Malte and quasi-flatmate Peter for all the cosy, tasty and inspiring hours on the sofa and on the balcony.

I am grateful to Jaci, Niklas, Johannes, Anne, Philipp, Kathleen, Lisa and Sina for always being there in mind, on the phone and as much as possible in person.

Thanks to the 'Wandahuren', Kevin, Anna, Sandra, Frank and special thanks to Steffi for sharing all the great experiences, especially in the happy hours with Wanda.

I am deeply grateful for having my office mates Vivi and Alex, who always provide such a positive, energetic and relaxed atmosphere and I thank Jessica and Rainer for a lot of laughter. Many thanks go to Johannes, Dirk and Leo for all the seasonal 'Späße'.

Thanks to the Volleyballgirls of GWE and to my beachvolleyball mates for getting me out of the office on the court and in the sand.
-Without all of you life would have been pretty boring.

I heartily thank my parents for all their love and absolute supply, the many hours on the phone and for always letting me come home. Thanks Ulrike for being so different and so equal to me and to little sunshine Oskar. Finally, I thank my grandparents for always trusting much more in me than I could ever do.

Eidesstattliche Versicherung-
Declaration of oath

Hiermit erkläre ich an Eides statt, dass ich die vorliegende Dissertationsschrift selbst verfasst und keine anderen als die angegebenen Quellen und Hilfsmittel benutzt habe.

I hereby declare, on oath, that I have written the present dissertation by myself and have not used other than the acknowledged resources and aids.

Signed: _____

Date: _____